Millimeter-Wave Integrated-Circuit Horn-Antenna Imaging Arrays

Thesis by

Yong Guo

In Partial Fulfillment of the Requirements

for the Degree of

Doctor of Philosophy

California Institute of Technology

Pasadena, California

1992

(Submitted August 5, 1991)

To My Wife and Parents

Acknowledgements

I would like to express my deep gratitude to my advisor, Professor David Rutledge, for letting me have such a wonderful opportunity to study and do research in the MMIC group at Caltech. His guidance, encouragement and support made this work possible. His scientific intuition, kindness and understanding left a deep impression on me. His industriousness and enthusiasm made my stay at Caltech an exciting and rewarding experience.

I also wish to thank Professor Gabriel Rebeiz and Dr. Wayne Lam for showing me fabrication techniques when I was getting started in the group. Many thanks go to Dr. Phil Stimson, Karen Lee and Kent Potter for their technical support in so many areas. I am grateful for the friendship and help of my fellow students in the group, Bobby Weikle, Dr. Scott Wedge, Jon Hacker, Moonil Kim, Victor Lubecke, Olga Boric, Lars Foged, Jung-Chih Chiao, David Haub and Mike DeLisio. Thanks also go to Professor Zoya Popovic, Dr. Dayalan Kasilingam, Dr. Wyman Williams, Professor Rick Compton and Dr. Wade Regehr for sharing their friendship and technical help. I would like to thank Dale Yee for informative conversations about daily life. I also thank all my other friends for the good times we spent together and for making my life at Caltech more pleasant and enjoyable.

Finally, I would like to thank my parents and my brothers and sisters for their love, encouragement and for always being there whenever I needed them. With my deepest appreciation, I thank my wife Yijin Wang for her love, understanding and support.

Millimeter-Wave Integrated-Circuit Horn-Antenna Imaging Arrays

Abstract

A new millimeter-wave, integrated-circuit, back-to-back, horn-antenna-mixer array is presented. The configuration of the array is one called "displaced back-to-back horn-antenna array," which consists of a set of forward- and backward-looking horns made with a set of silicon wafers. The front side is used to receive the incoming signal, and the back side is used to feed the local oscillator. IF is led out from the side of the array. Pyramidal-shaped horns in silicon bounded by (111) crystal planes were formed by anisotropic etching of the silicon wafers. The power received by the horns is picked up by antenna probes suspended on thin silicon-oxynitride membranes inside the horns. The array is fully two-dimensional, and the horns are made simultaneously by integrated-circuit processing techniques. Aperture efficiency of the horn-antenna array has been improved up to 72 %, and system coupling efficiency is 36 %. In the efficiency measurements, a new thin-film, power-density meter is developed for measuring the absolute power densities. The main applications of the array include imaging, remote sensing and plasma diagnostics.

Contents

Chapter 1

Introduction

Millimeterwaves, as the name implies, are the waves whose wavelengths range in millimeters. Traditionally, they are the electromagnetic waves of the wavelengths from 1 mm to 10 mm, corresponding to frequencies from 300 GHz to 30 GHz [1]. For comparison, microwaves are from 1 GHz to 30 GHz. The history of millimeterwaves and microwaves are embodied in the evolution of electromagnetic waves. James Clerk Maxwell (1831–1879), regarded as the founder of electromagnetics theory in its present form, unified, in four equations, all previous known results, experimental and theoretical, on electromagnetics. He also predicted the existence of electromagnetic waves. Heinrich Rudolf Hertz (1857–1894) experimentally confirmed Maxwell's prediction in 1888 [2]. In his experiment, Hertz produced the radiation with a spark-gap generator and recorded wavelengths in the centimeter range. Soon after, the first reported activity in millimeter-wave technology began in the 1890's [3]. In those experiments, methods similar to Hertz's were used and wavelengths detected were estimated to be 6 and 4 mm. Much later, researchers developed various components, devices and sources, including the klystron and the cavity magnetron. Early applications of these sources in radars occurred at microwave frequencies rather than at millimeter-wave frequencies, and progress in millimeterwaves was very slow. In the 1940s, high-accuracy radar requirements raised radar researchers' inter-

est in millimeterwaves. As a result, millimeter-wave advances were mainly from extensions of microwave technology, largely based on the availability of coherent oscillators. The current interest in millimeterwaves arises from the realization that there are limitations to what can be accomplished with infrared and optical systems, in particular their disadvantages in fog, smoke and dust. Furthermore, in communications, the widespread use of microwaves has forced microwave engineers to look for even higher frequencies, i.e. millimeterwaves.

Recent research interests in millimeterwaves are more focused on new technologies of power sources, sensitive detectors and systems. Significant advances have been made continuously in the area of millimeter-wave, integrated circuits. In addition, the design and fabrication of monolithic integrated circuits on semiconductors substrates, e.g., silicon, gallium arsenide and indium phosphide, are well advanced [4–7]. These include amplifiers [8–10], frequency multipliers [11–13], oscillators [14–16], power combiners [17–19] and antennas [20–23]. Computers also play an important role in the circuit design and modeling, as well as in the development of new theories and techniques. Using a computer-controlled network analyzer working at the frequencies up to 110 GHz, measurements can be carried out automatically with great precision. In astronomy, millimeter-wave, superconducter-insulator-superconducter (SIS) junction detectors have been widely used [24–26]. Application of high-temperature superconductors in millimeterwaves was attempted as soon as the new material was invented [27]. The hybrid techniques, on the other hand, have been refined to the point where they compete with monolithic circuits in terms of performance.

Millimeter-wave systems have shorter wavelengths and larger bandwidths than microwave systems. Millimeterwaves also have interaction with atmospheric constituents. These characteristics make millimeterwaves have both advantages and disadvantages, depending on the applications [28]. Compared to microwaves, the shorter wavelengths allow the reduction of component and sys-

tem size, which is attractive for satellites and aircraft. The antennas have narrower beamwidths, providing better resolution and precision in target tracking and discrimination. Wider bandwidths provide a high-information-rate capability in communications and high immunity to jamming and interference, because of the large number of frequencies that can be used. Wider bandwidths also have the benefit of greater Doppler frequencies, resulting in increasing detection and recognition capabilities of slow-moving objects. Atmospheric attenuation and losses of millimeterwaves are relatively low in the transmission windows compared to infrared and optical frequencies, which make millimeterwaves more attractive in unfavorable environment conditions, like fog, smoke and dust. On the other hand, smaller wavelengths and smaller component size increase the need for greater precision in manufacturing, which means higher costs, and narrow-beamwidth millimeter radars are not suitable for large-volume search.

The main applications of millimeterwaves are telecommunications, radar, radiometry and instrumentation. These include earth-to-satellite communications, satellite-to-satellite communications, remote sensing, target tracking, imaging, detection of atmospheric pollutants, plasma diagnostics, and military applications [29–31].

1.1 Imaging Arrays and Quasi-Optical Mixers

A two-dimensional, focal-plane imaging array with an optical lens can be taken as a camera working at the millimeter-wave frequencies (Fig. 1.1), compared to a 35 mm camera working at the frequencies of visible light. The scene either may be illuminated by a radar signal or may merely emit the blackbody radiation. The energy from the scene is focused through an objective lens onto the receiver array. The imaging array consists of many detectors located at the focal plane in the imaging system. Each single detector generates an output proportional to the energy emitted by its respective pixel. An appropriate pro-

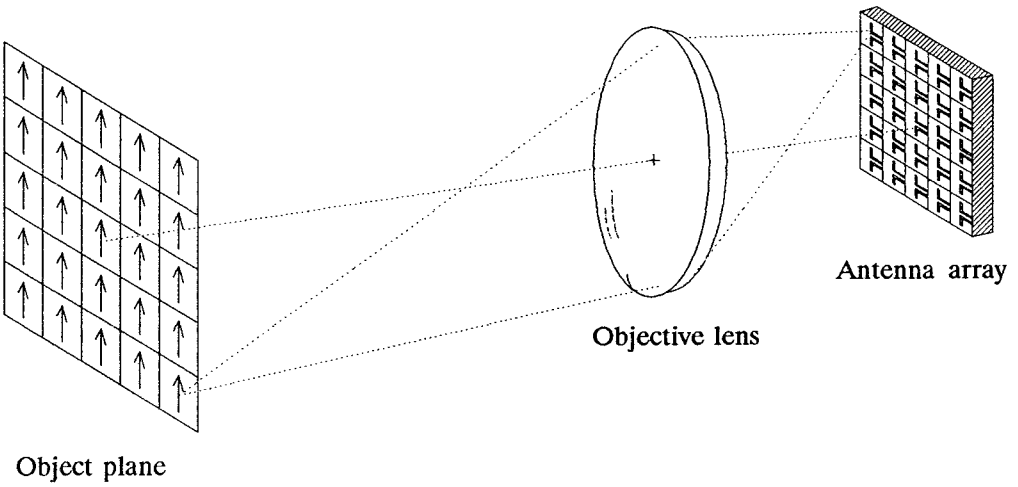

Figure 1.1 Basic configuration of a millimeter-wave imaging system.

cessing circuit can display a visual image of the millimeter-wave scene of the far field. Since many identically built detectors are required for this application, standard, integrated-circuit fabrication technologies can be used effectively.

A single-element, millimeter-wave scanning system, on the other hand, sees only one pixel at a time; therefore, it is not able to image on rapidly moving objects. Scanning systems can offer real-time imaging, at the cost of noisy performance because their integration time per pixel is very short. Two-dimensional imaging arrays offer much faster imaging of a scene than a single-element scanning system [32].

Mixer techniques are commonly used at millimeter-wave frequencies and the frequencies beyond. The biggest advantage of these techniques is that they avoid the difficulty of building high-frequency amplifiers for the receivers. Instead, they mix the incoming signal (RF) with a local oscillator (LO) signal to produce an intermediate frequency signal (IF) and IF can be easily amplified and processed. Traditionally, mixers are made of mixing elements and wave-guide circuits which are normally machined. At shorter wavelengths, the wave-guide circuits become

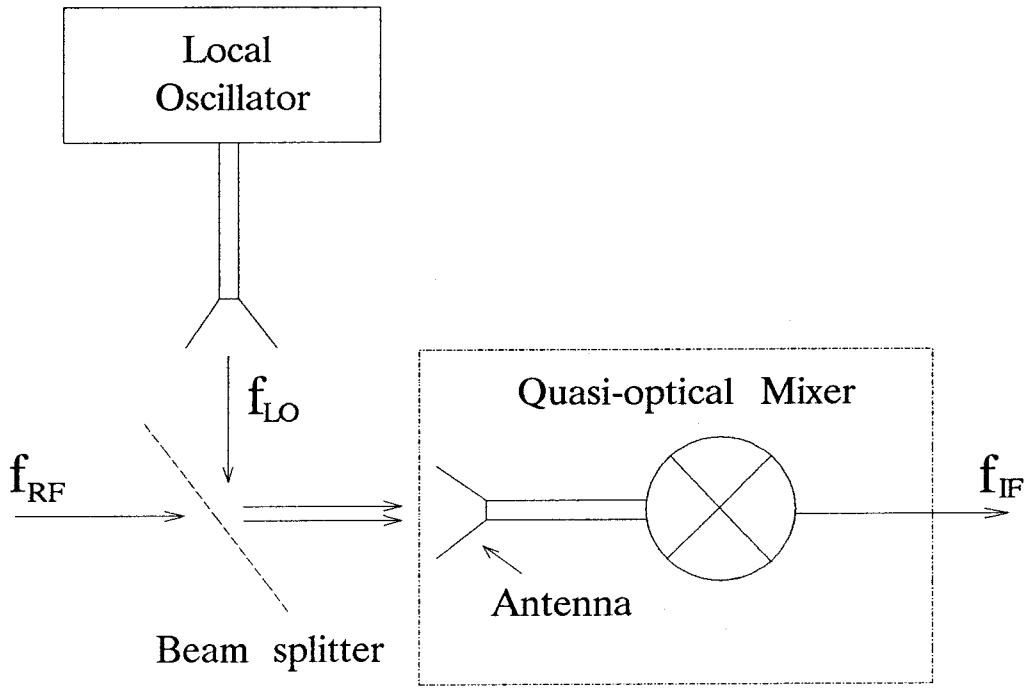

Figure 1.2 Basic structure of a quasi-optical mixer.

much smaller, making them very expensive to build. Quasi-optical components, however, provide a solution to this problem. They combine the function of an antenna and a mixer circuit into a single array. These types of circuits potentially can be mass-produced by standard, integrated-circuit technology. The applications of this technique include radars, satellite communication and imaging systems.

Fig. 1.2 shows a diagram of a quasi-optical mixer. The RF signal through the diplexer is captured by the antenna, which is integrated into the mixer circuit. The LO signal reflected by the diplexer can also be captured by the same antenna. Both RF and LO are fed into the mixer behind the antenna. For these kinds of mixers, the LO-to-RF isolation is more difficult than the conventional mixers; however, polarization duplexing can be used for improvement of this

characteristic. Since a quasi-optical mixer is a combination of an antenna and a mixer circuit, the mixers can be made compact and are potentially low cost. In addition, one local oscillator can be used for all mixers if they are illuminated by the LO signal in a quasi-optical manner. Quasi-optical mixers are an excellent candidate for imaging arrays.

1.2 Integrated-Circuit, Back-to-Back Antenna-Mixer Arrays

The integrated-circuit quasi-optical two-dimensional back-to-back horn-antenna-mixer array (Fig. 1.3) presented in this thesis combines antennas and mixer circuits monolithically. The array uses the focusing properties of the horn and is made based on anisotropic etching of silicon. The etch forms pyramidal cavities bounded by (111) crystal planes. The horn configuration is a so-called "displaced back-to-back horn array," which consists of a set of forward- and backward-looking horns sharing the same membrane wafer. The horns are made on a stack of silicon wafers pyramidally etched. Gold is evaporated on the side-walls of the horns to make them highly conducting. The front side is used to receive the signal RF, and the back side is used for the LO. Both RF and LO are picked up by dipole probes suspended on 1-μm silicon-oxynitride membranes inside the horns on one of the central wafers. The power is detected by the bismuth microbolometers between the dipole probes. Instead of being supported by a thick substrate, the probes and detectors are on the thin membrane, thinner than a thousandth of the wavelength; consequently, the dielectric losses of the antenna are negligible.

In order to make the array couple the incoming energy efficiently, the receiving area of each detector of the imaging array at the focal plane should be as big as the resolution cell, the maximum physical area corresponding to its respective pixel. In a diffraction-limited imaging system, in which the imaging array samples the imaging at such a rate that the resolution of the reconstructed image

is limited only by the optical system [33], it is shown [34] that the sampling distance of field-magnitude detection is $f\,\lambda$ in free space, where f is the f-number of the optical system and λ is the signal wavelength. Once the distance between the detectors is determined, the maximum physical area for each horn is also fixed. In this design, the horn spacing is $1\,\lambda$, assuming the antenna array to be used in an f-1 system. In the antenna array, each detector can use the maxi-

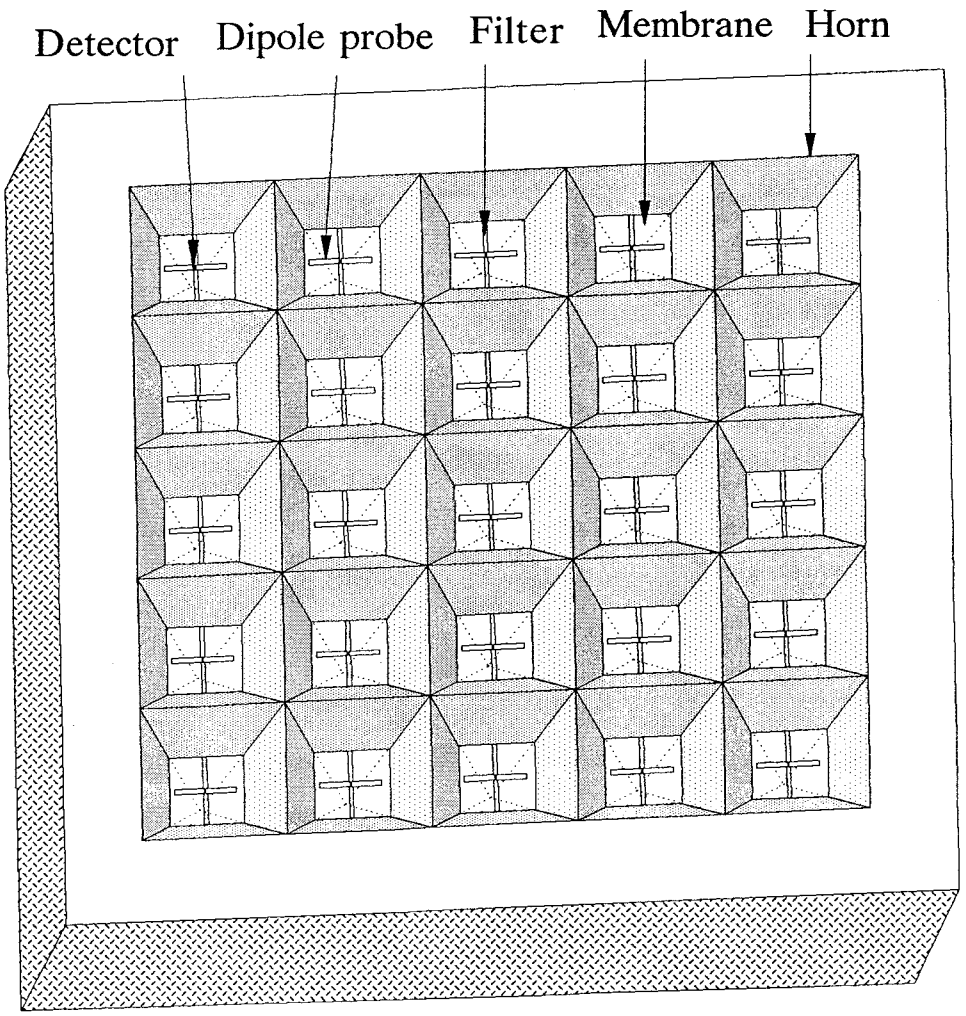

Figure 1.3 (a)

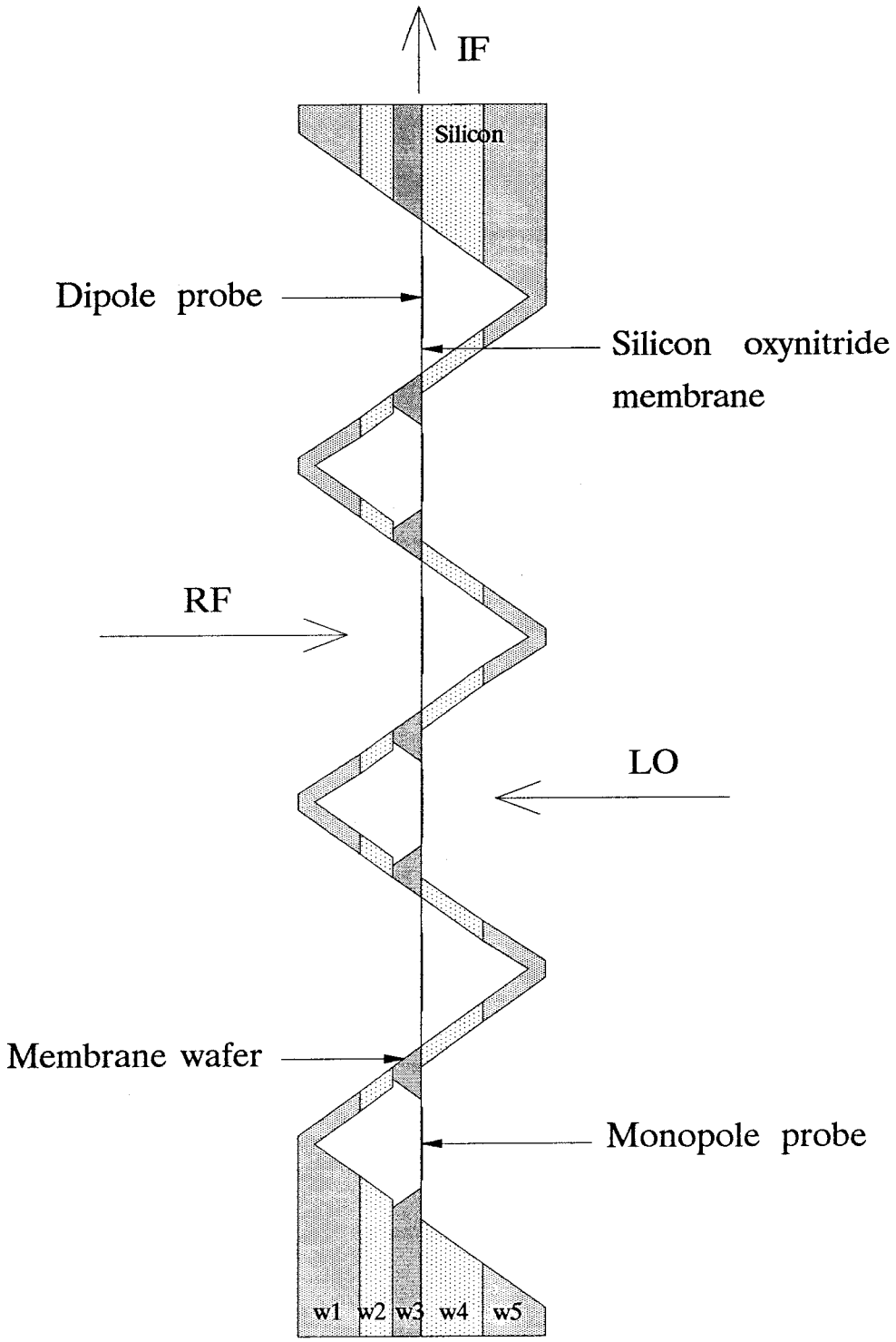

Figure 1.3 (b)

Figure 1.3 The back-to-back mixer array. Front view (a). Cross-sectional view (b).

mum available space to receive the incoming power, but can also leave plenty of room for electronic interconnections between the detectors. The array is fully two-dimensional, and the horns are made simultaneously by integrated-circuit processing techniques.

The aperture efficiency of a single horn in the array is defined as the power received by the detector in the horn divided by the total power incident on the horn aperture, when the array is illuminated by a plane wave. This definition includes the taper loss, the cross-polarization loss, and the coupling loss between neighboring horns. It also includes a mismatch loss between the dipole probe and the detector, and the resistive loss of the sidewalls in the horn. Because aperture efficiency of the imaging array is very important for its applications, it need be investigated in detail and optimized. The designs of the back-to-back antenna-mixer array are based on those horn arrays with optimized aperture efficiencies. Applications of the back-to-back horn-antenna-mixer array include imaging, remote sensing, atmospheric pollutant detecting, plasma diagnostics and so forth.

1.3 Overview of the Thesis

The goal of the project is to develop high-efficiency integrated-circuit horn-antenna imaging arrays for millimeter-wave applications. The effort has been mainly emphasized on optimizing the efficiencies of the horn imaging arrays, improving the fabrication procedures, and designs for the integrated-circuit back-to-back horn-antenna-mixer arrays.

In Chapter 2, the aperture efficiency of the horn-antenna array is studied. Impedance mismatch, resistive, cross-polarization and horn-to-horn coupling losses of the array are analyzed. Dipole impedance in a scaled model horn is measured. Designs of dipole probes, coplanar strips and microbolometers are presented and discussed. The theory and the design of a new quasi-optical

power-density meter to be used in efficiency measurements are also presented in this chapter.

Chapter 3 presents fabrication procedures of etching horns in the silicon wafers: growing low-stressed membranes on the surface of silicon wafers; making one-step, bismuth, thermal-microbolometers with four-wire connections; coating the entire sidewalls of the horns with gold, and building the power-density meters. Photographs of the completed imaging array as well as the etched silicon wafers before assembling are also illustrated in the chapter.

Chapter 4 describes the aperture-efficiency measurement setups and calibrations, and gives the results of the measured aperture efficiencies at different dipole probe lengths as well as the system-coupling efficiencies with variant f-numbers at 93 GHz. Measured aperture efficiencies in the W-band (75–110 GHz) are also presented. In Section 4.4, test results of beam-lead diodes in the horn array are given. These results include both environmental tests and pattern measurements.

Chapter 5 presents the designs of the horn structures and circuits of the integrated-circuit, back-to-back, horn-antenna-mixer arrays, in which both fundamentally and subharmonically pumped, antenna-mixer designs are described. Various antenna probes inside scaled model horns are tested in searching for proper probes for the best RF and LO receptions. The measured impedances are illustrated in the Smith charts.

Chapter 6 illustrates a unit-cell of the subharmonically pumped, antenna-mixer array. The unit-cell, which has been built on a microwave scaled-model, consists of one local oscillator horn and four RF horns. Measurements of impedances and reception properties of the unit cell for both the RF horns and the LO horn at frequencies from 2 to 12 GHz are presented and discussed. The RF-LO and LO-RF isolations, as well as the pattern measurements of the RF horns and

the LO horn in the unit cell, are also presented.

Chapter 7 presents some possible new research directions in the future based on current research results and analysis. Ideas include transmission lines made in silicon; back-to-back arrays to be scaled to terahertz range; introducing monolithic Schottky diodes in the arrays; integrating superconducting tunnel junction devices in the arrays; and mounting a monolithic millimeter-wave integrated circuit amplifier in the arrays.

References

[1] N. C. Currie, C. E. Brown, "Principles and Applications of Millimeter-Wave Radar," Artech House, Inc., Norwood, MA, 1987.

[2] J. H. Bryant, "Heinrich Hertz, the Beginning of Microwaves," IEEE, Inc., New York, 1988.

[3] J.C. Wiltse, "History of Millimeter and Submillimeter-Waves," *IEEE Transactions on Microwave Theory and Techniques*, Vol. MTT-32, pp. 1118–1127, September 1984.

[4] J.F. Luy, "Silicon-Based Millimeter-Wave Integrated-Circuits," *Thin solid Films*, vol. 184, pp. 185–197, January, 1990.

[5] S.K. Roy, and J.P. Banerjee, "Properties of Gallium-Arsenide and Indium-Phosphide Impatts at Microwave and Millimeter-Wave Frequencies," *Bulletin of Materials Science*, vol 13, pp. 113–119, 1990.

[6] J.W. Archer, R.A. Batchelor, "Low-Parasitic, Planar Schottky Diodes for Millimeter-Wave Integrated-Circuits," *IEEE Transactions on Microwave Theory and Techniques*, vol. 38, pp. 15–22, January, 1990.

[7] J.V. Bellantoni, D.C. Bartle, G. McDermott, S. Bandla, R. Tayrani, L. Raffaelli, "Monolithic GaAs P-I-N-Diode Switch Circuits for High-Power Millimeter-Wave Applications," *IEEE Transactions on Microwave Theory and Techniques*, vol. 37, pp. 2162–2165, 1989.

[8] Reza Majidi-Ahy C.K. Nishimoto et al., "5–100 GHz InP Coplanar Waveguide MMIC Distributed Amplifier," *IEEE Transactions on Microwave Theory and Techniques*, Vol. 38, pp. 1986–1993, December 1990.

[9] K.H.G. Duh et al., P.C. Chao, P. Ho, M.Y. Kao, P.M. Smith, J.M. Ballingall, A.A. Jabra, "High-Performance InP-Based HEMT Millimeter-Wave Low-

Noise Amplifiers," *IEEE MTT-S Int. Microwave Symp. Dig.*, pp. 805–808, 1989.

[10] J. Perdomo, M. Mierzwinski, H. Kondoh, C. Li, and T. Taylor, "A Monolithic 0.5 to 50 GHz MODFET Distributed Amplifier With 6 dB Gain," *GaAs IC Symp. Dig.*, pp. 91–94, 1989,

[11] Y. Kwon, D. Pavlidis, P. Marsh, M. Tutt, G.I. Ng, T. Brock, "90 to 180 GHz Heterostructure Monolithic Integrated Doubler," *Second International Symposium on Space Terahertz Technology*, JPL, Pasadena, CA, February 26–28, 1991.

[12] R.J. Hwu, L.P. Sadwick, and G.B. Stringfellow, "III-V Compound Semiconductor MIS Varactor Millimeter and Submillimeter-Wave Frequency Multipliers," *Second International Symposium on Space Terahertz Technology*, JPL, Pasadena, CA, February 26–28, 1991.

[13] E. Kollberg, A. Rydberg, "Quantum-Barrier-Varactor Diodes for High-Efficiency Millimeter-wave Multipliers," *Electronics Letters*, vol. 25, pp. 1696–1698, 1989.

[14] E.R. Brown, C.D. Parker, "Recent Advance in Resonant-Tunneling Diode Oscillators," *Second International Symposium on Space Terahertz Technology*, JPL, Pasadena, CA, February 26–28, 1991.

[15] H. Eisele, R.K. Mains, and G.I. Haddad, "GaAs IMPATT Diodes For Frequencies Above 100 GHz: Technology and Performance," *Second International Symposium on Space Terahertz Technology*, JPL, Pasadena, CA, February 26–28, 1991.

[16] A. Rydberg, "High-Efficiency and Output Power from 2nd-Harmonic and 3rd-Harmonic Millimeter-Wave INP-TED Oscillators at Frequencies above 170 GHz," *IEEE Electron Device Letters*, vol. 11, pp. 439–441, October,

1990.

[17] M. Nakayama, M. Hieda, T. Tanaka, H. Kondo, and K. Mizuno, "Millimeter And Submillimeter-Wave Quasi-Optical Oscillator with Multi-Elements," *Second International Symposium on Space Terahertz Technology*, JPL, Pasadena, CA, February 26–28, 1991.

[18] T. Itoh, "Network Analysis of Planar Spatial Power Combining," *Second International Symposium on Space Terahertz Technology*, JPL, Pasadena, CA, February 26–28, 1991.

[19] N. Camilleri, B. Bayraktaroglu, "Monolithic Millimeter-Wave IMPATT Oscillator and Active Antenna," *IEEE Transactions on Microwave Theory and Techniques,* Vol. 36, pp. 1670–1676, December, 1988.

[20] A.A. Oliner, "Recent Developments in Millimeter-Wave Antennas," *Alta Frequenza*, vol. 58, pp. 491–505, 1989.

[21] F. Schwering, A.A. Oliner, "Millimeter-Wave Antennas," Chap. 17 of *Antenna Handbook: Theory, Applications and Design*, (Eds, Y.T. Lo and S.W. Lee), Van Nostrand Reinhold Company, New York, 1988.

[22] D.B. Rutledge, D.P. Neikirk, D.P. Kasilingam, "Integrated-Circuit Antennas," *Infrared and Millimeter-Waves*, vol. 10, (ed. K.J. Button), Chapter 1, pp. 1–90, Academic Press, New York, 1983.

[23] K.S. Yngvesson, "Near-Millimeter Imaging with Integrated Planar Receptors: General Requirements and Constraints," *Infrared and Millimeter-Waves*, vol. 10 (ed. K.J. Button), Chapter 2, pp. 91–110, Academic Press, New York, 1983.

[24] R. Monaco, "Josephson Millimeter-Wave Oscillators," *International Journal of Infrared and Millimeter Waves*, vol. 11, pp. 533-564, April, 1990.

[25] A.N. Vystavkin, V.P. Kosheletz, and G.A. Ovsiannikov, "Millimeter-Wave Receivers on Superconductors," Radiotekhnika I Elektronika, vol. 34, pp. 2465-2483, December, 1989.

[26] T. G. Phillips and D. B. Rutledge, "Superconducting Tunnel Detectors in Radio Astronomy," *Scientific American* vol. 254, pp. 96–102, 1986.

[27] N.F. Pedersen, "Millimeter-Wave Detectors Based on Future Thin-Film High-Tc Josephson-Junctions," *Physica B*, vol. 165, pp. 107-108, August, 1990.

[28] P. Bhartia, I.J. Bahl, *Millimeter-Wave Engineering and Applications*, John Wiley & Sons, New York, 1984.

[29] R.J. Hwu, L. Sjogren, N.C. Luhmann, et al., "Millimeter And Submillimeter-Wave Technology Developments for the Next Generation of Fusion Devices," *Review of Scientific Instruments*, vol. 61, pp. 3253–3255, October, 1990.

[30] H. Suss, K. Gruner, and W.J. Wilson, "Passive Millimeter-Wave Imaging a Tool for Remote-Sensing," *Alta Frequenza*, vol. 58, pp. 457-465, 1989.

[31] K. Miyanchi, "Millimeter-Wave Communications," *Infrared and Millimeter Waves*, Chap. 1, pp. 1–94, (ed. K. J. Button), Academic Press, New York, 1983.

[32] W. J. Wilson, R. J. Howard, A. C. Ibbott, G. S. Parks and W. B. Ricketts, "Millimeter-Wave Imaging Sensor," *IEEE Trans. Microwave Theory Tech*, vol. 34, pp. 1026–1035, 1986.

[33] J. W. Goodman, "Introduction to Fourier Optics," pp. 4–21, McGraw Hill, New York, 1968.

[34] D.P. Neikirk et al., "Far-Infrared Imaging Antenna Arrays," *Applied Physics Letters*, vol. 40, pp. 203–205, 1982.

Chapter 2

Horn-Antenna Efficiency Analysis and Circuits Design

The aperture efficiency of the horn antennas has been studied on a single-side antenna array consisting of a set of 4 silicon wafers (Figure 2.1). These wafers were etched by an anisotropic etchant [1], and pyramidal cavities in the wafers were formed bounded by (111) crystal planes [2]. The aperture efficiency of a single horn in the array is defined as the power received by the detector in the horn divided by the total power incident on the horn aperture when the array is illuminated by a plane wave. The theoretical pattern of the horn array was calculated [3] by approximating the horn as a set of cascade rectangular waveguides. To do this, the boundary conditions were matched at each of the waveguide discontinuity and at the aperture of the horn. Then the pattern was found, using reciprocity, by calculating the received fields inside the horn for waves at different incident angles. The theory also predicted the normalized electric-field distribution along the horn axis for a normal-incident plane-wave. The normalized electric field in the horn along the horn axis is given in Figure 2.2 [3] for an antenna array with horn openings of $1.0\,\lambda$ square. The field distribution indicates that the best feed position for the antenna probes is 0.4–$0.6\,\lambda$ from the apex. In addition, the receiving patterns of the horn antennas were measured at 93 GHz and 242 GHz, and a measured horn aperture-efficiency of 44 % was obtained [3]. This value of the aperture efficiency is considered to be low for most

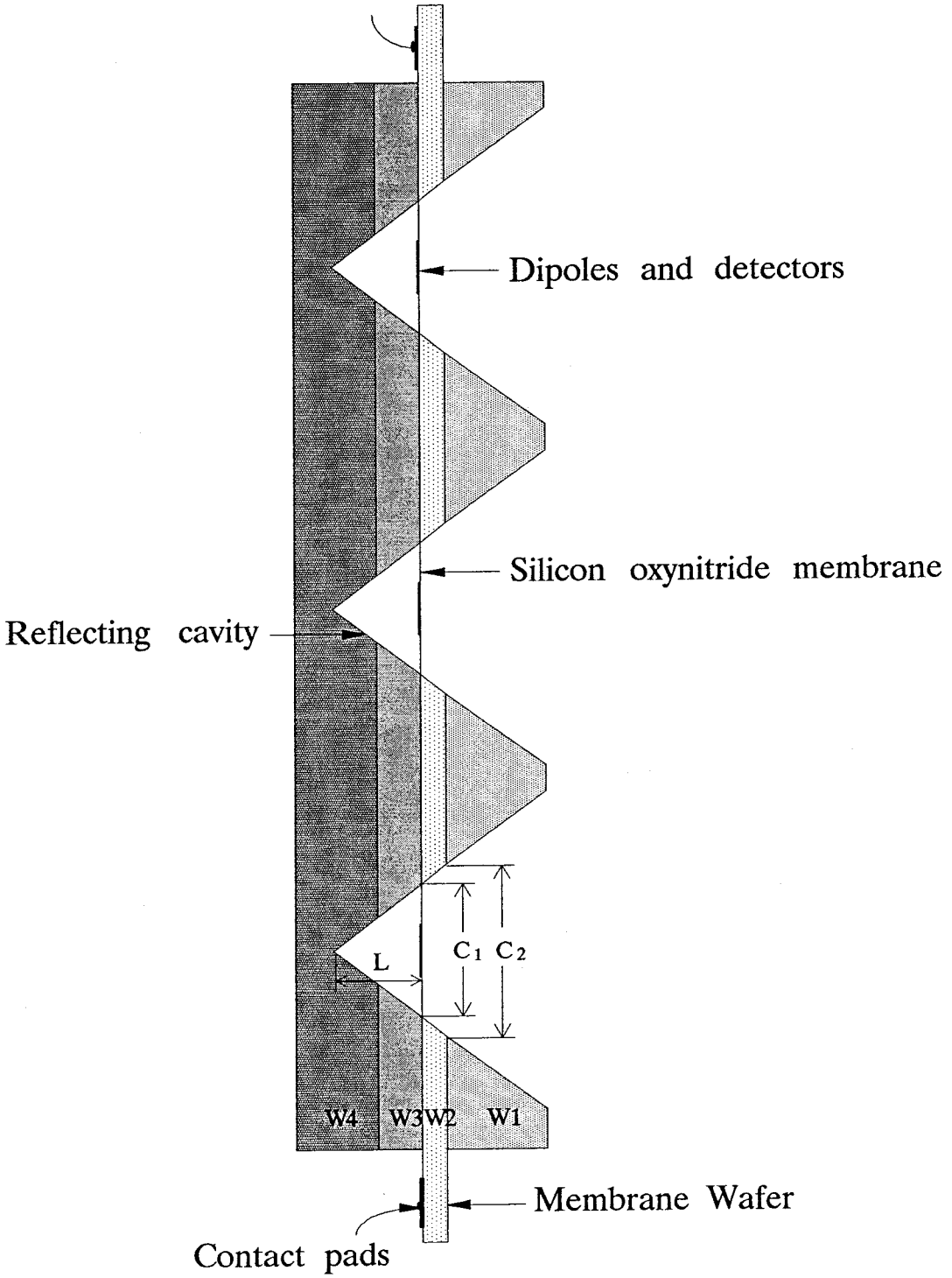

Figure 2.1 Cross-sectional view of a single-side horn antenna array.

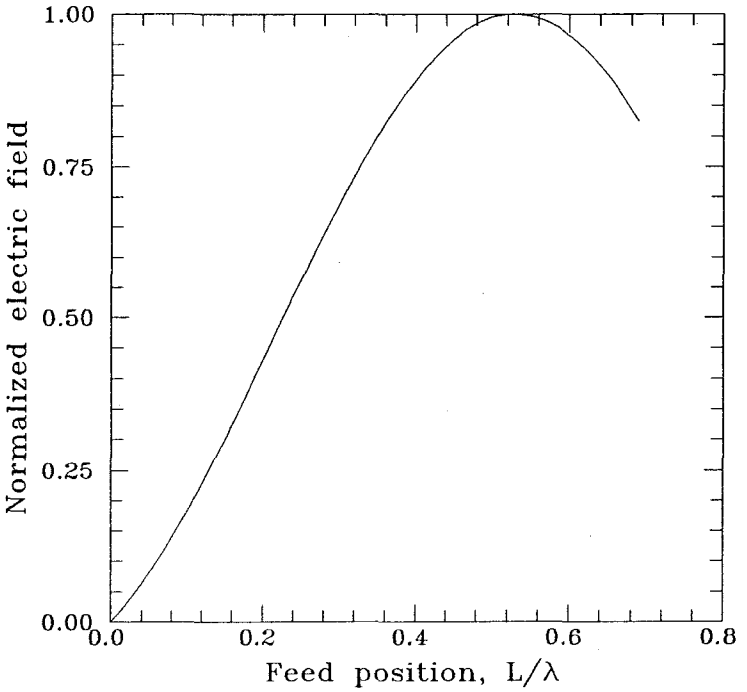

Figure 2.2 The normalized electric-field distribution along the horn axis for a normal-incident plane-wave onto a horn antenna array with 1.0 λ square openings.

applications; therefore, losses of the horn antenna array need to be analyzed and reduced.

2.1 Horn-Antenna Losses

Horn antenna array losses include the taper loss, the cross-polarization loss, and the coupling loss between neighboring horns. They also include a mismatch loss between the dipole probe and the detector, and the resistive loss of the sidewalls in the horn. It is the mismatch loss and sidewall-resistive loss that turn out to be the biggest losses that need to be reduced in order to improve the aperture efficiency.

The taper loss is due to the non-uniform field distribution at the horn front, which can be analyzed in terms of the aperture efficiency of the horn when the

horn has a matched-load and no other losses, or simply the matched-load aperture efficiency. The matched-load aperture efficiency will be 100 % if the horn antenna is uniformly illuminated without any phase error [4], which, in reality, is always smaller than 100 %. Normally, the matched-load aperture efficiency will decrease when the aperture size increases because a wider flare angle introduces more non-uniformity of the field distribution. The matched-load aperture efficiency can be obtained by A_{eff}/A, where A_{eff} is the effective area and A is the physical area of the horn aperture. The effective aperture area A_{eff} of the horn is given by

$$A_{\text{eff}} = \frac{\lambda^2}{4\pi} D \tag{2.1}$$

where D is the co-polarized maximum directivity of the horn antenna defined as

$$D = \frac{4\pi}{\int_0^{2\pi} \int_0^{\frac{\pi}{2}} P_c \, \sin\theta \, d\theta \, d\phi} \tag{2.2}$$

in the formula, while P_c is the normalized, co-polarized radiation pattern of the antenna [3]. From the co-polar, two-dimensional scan at 93 GHz, the calculated result is $A_{\text{eff}}/A = 90\,\%$, or the taper loss is 0.5 dB.

The cross-polarization loss is the loss that is due to the cross-polarized electric field component which is measured at 93 GHz, and a maximum component of -15 dB is found in the 45° plane. An upper limit of the cross-polarization losses can be found by assuming that the cross-polarized 45° plane pattern is rotationally symmetric and by calculating the received power from this pattern. The co-polar and cross-polar directivity of the antenna is then given by

$$D = \frac{4\pi}{\int_0^{2\pi} \int_0^{\frac{\pi}{2}} P_c \, \sin\theta \, d\theta \, d\phi \; + \; \int_0^{2\pi} \int_0^{\frac{\pi}{2}} P_x \, \sin\theta \, d\theta \, d\phi} \tag{2.3}$$

where P_c and P_x are the normalized measured co-polar and cross-polar patterns. The effect of the cross-polarized component decreases the matched-load aperture

efficiency from 90 % to 86 %. Thus, the maximum cross-polarization loss is about 0.2 dB.

The horn sidewall loss comes from the exposed silicon wafer (W2) in Fig. 2.1, or membrane wafer, as it is called. While other silicon wafers were coated with gold by evaporation to make them highly conducting, the membrane wafer was not. This was because the membranes would also have been covered over during the evaporation. These silicon wafers have a resistivity of 0.55 Ωcm, measured using a four-point probe. The sidewall losses are then estimated by assuming that only TE_{10} exists in the horn. The effect of the high-order modes is neglected, and the TE_{10} current distribution on the sidewalls can be calculated [5]. Then the resistive loss is obtained by

$$L_{\text{resis}} = \frac{\sqrt{2}R_s}{377} \int_{C_1}^{C_2} \frac{1 + 2(\frac{\lambda}{2C_z})^2}{C_z\sqrt{1 - (\frac{\lambda}{2C_z})^2}} dC_z \tag{2.4}$$

where C_z is the variable cross section of the pyramidal cavity. $C_2 = 0.7\,\lambda$ and $C_1 = 0.56\,\lambda$ are, respectively, the front and the back cross sections of the horns on the membrane wafer. R_s is the millimeter-wave surface resistance of the sidewalls, given by

$$R_s = \sqrt{\frac{\pi f \mu}{\sigma}} \tag{2.5}$$

where μ and σ are the permeability and conductivity of the horn sidewalls, and f is the operating frequency. For the membrane wafer, $R_s = 45\,\Omega$ at 93 GHz. Additionally, the integral in Equation 2.4 is not valid for cross sections smaller than $0.5\,\lambda$. The losses of the gold-coated sections are negligible because R_s is very small. The total sidewall losses are calculated to be about 0.7 dB.

2.2 Horn-Antenna Modeling

In order to understand the dipole probe behavior inside the horn, a 3×3 horn-array microwave scale model was built of aluminium at an operating frequency of 7.3 GHz. A dipole probe and a coplanar-strip transmission line made of copper foil were put inside the horn, $0.37\,\lambda$ away from the horn apex. This is the same position as the dipole probes inside the 93 GHz horn array. The coplanar-strip transmission line was shorted $\lambda/4$ away from the dipole (Figure 2.3), and the dipole was connected to the coaxial line leading to a network analyzer [6], which is calibrated to the end of the test set cable, using coax standards. The length of the coaxial line between the dipole probe and the test-set cable is measured electrically by shortening the end point of the coaxial line at the center of the dipole probe and measuring the electric delay. This extra length of the coaxial line is calibrated out when the measured impedances are plotted on the Smith chart by Puff, a microwave software CAD program [7].

The measurements were done on several different lengths of dipole probes, from $0.32\,\lambda$ to $0.5\,\lambda$. The measured results are shown in Figure 2.4. The effect of the cavity is that it increases the reactive impedance of the dipole. In other words, it makes the dipole probe effectively longer. For an $0.5\,\lambda$ dipole, as it was designed in the 44 % aperture-efficiency measurement, the impedance is $54 + \mathrm{j}95\,\Omega$, compared with the bolometer resistance, $138\,\Omega$. The impedance mismatch loss is then calculated by using

$$L_m = \frac{4R_dR_b}{(R_t^2 + X_d^2)} \tag{2.6}$$

where R_d is the dipole radiation-resistance; R_b is the bolometer resistance; R_t is the sum of the dipole radiation-resistance, the bolometer resistance and the series resistance in the circuit ($4\,\Omega$); and X_d is the dipole reactive impedance. The calculated mismatch loss is 2.2 dB.

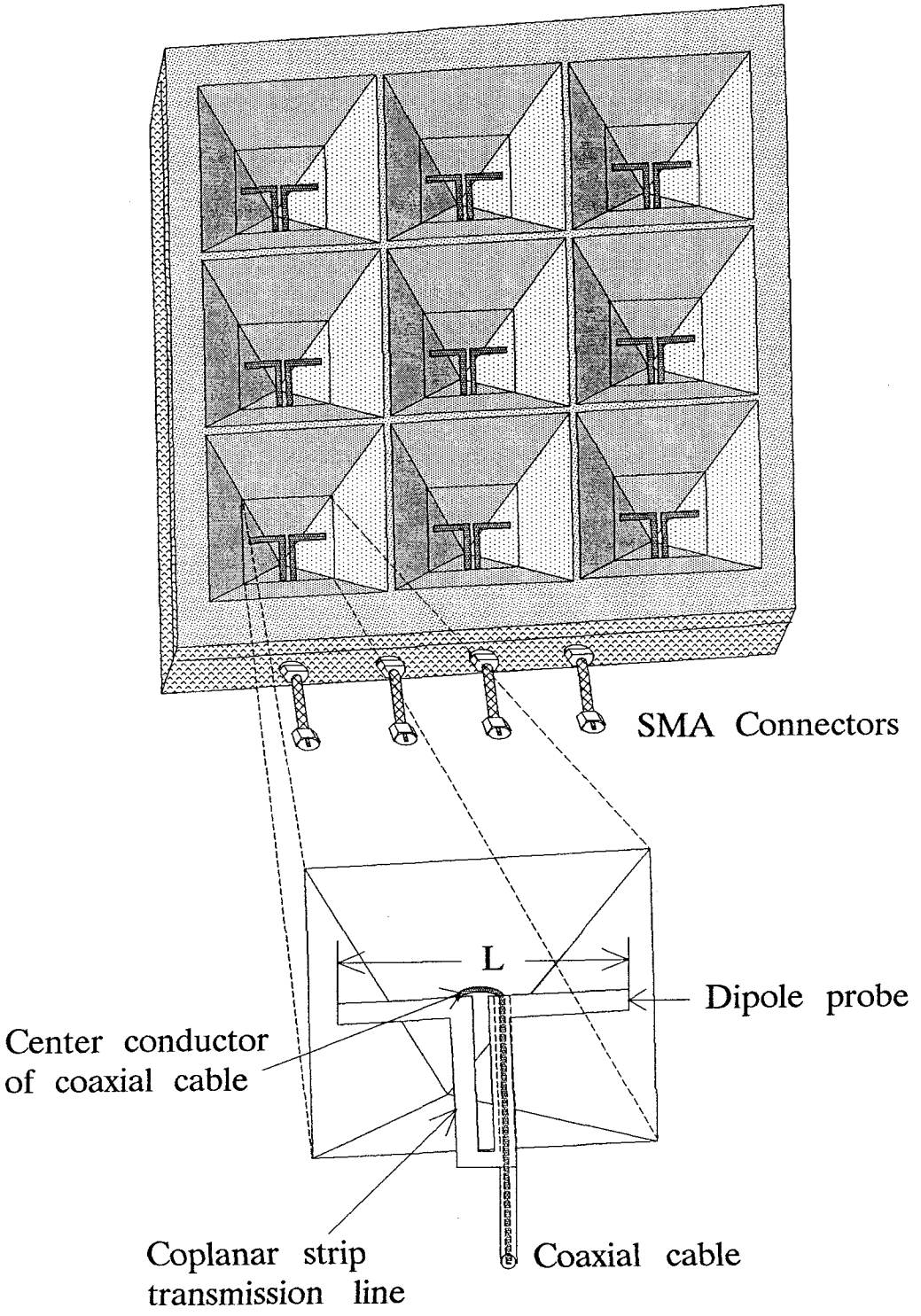

Figure 2.3 A 3 × 3 horn-array model at 7.3 GHz.

The horn-to-horn coupling loss between nearby horns was also measured on this model array by measuring the S_{12} parameters, and the loss is estimated to be 0.1 dB. In summary, the analyzed losses are listed in Figure 2.5. Among those losses, the two biggest losses are the impedance mismatch loss of 2.2 dB and the horn-sidewall resistive lose of 0.7 dB. The total calculated loss is 3.7 dB versus

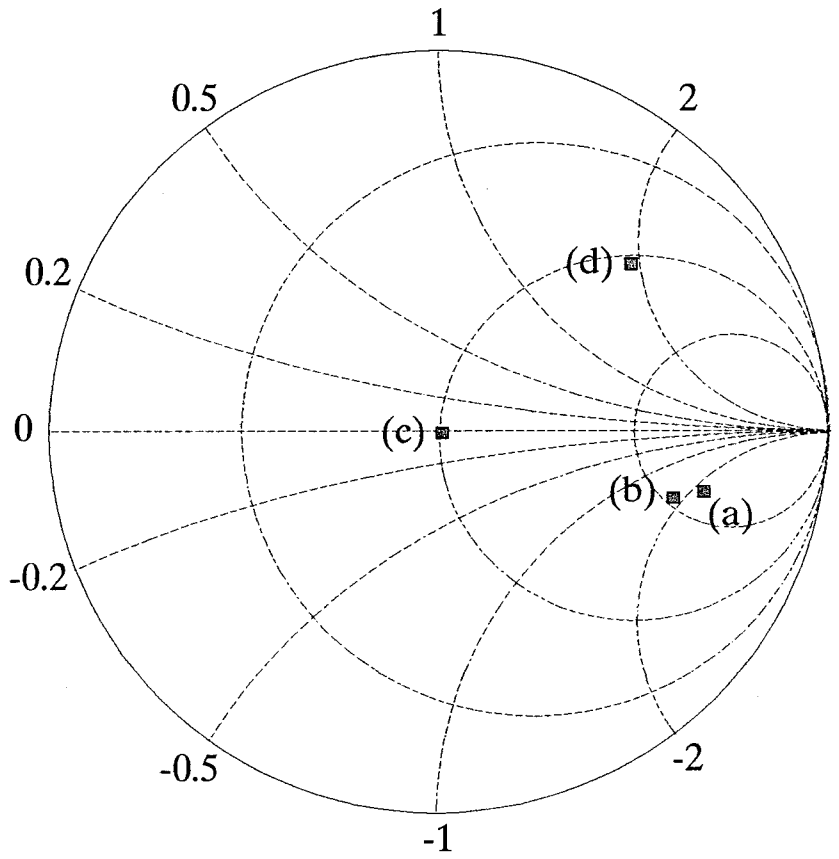

(a) L=0.20λ; Z=220 Ω - j116 Ω;
(b) L=0.30λ; Z=160 Ω - j79 Ω;
(c) L=0.40λ; Z=50Ω +j0.1 Ω;
(d) L=0.50λ; Z=54 Ω +j95 Ω;

Figure 2.4 Measured dipole-probe impedances on the Smith chart.

Loss component	loss, dB
Taper loss	0.5
Cross-polarization loss	0.2
Horn-sidewall loss	0.7
Mismatch loss	2.2
Horn-to-horn coupling loss	0.1
Total calculated loss	3.7
Measured loss	3.6

Figure 2.5 The summary of calculated and measured losses.

the measured result of 3.6 dB.

2.3 Dipole and Circuits Design

The impedance-mismatch loss and the horn-sidewall resistive loss are to be reduced or eliminated; however, the reduction of the taper loss is not included in this effort. The reason is that the taper loss comes from the non-uniformity of the field distribution and phase error, which will not change unless the flare angle of the horn, determined by the silicon (111) crystal planes, is reduced. Figure 2.6 illustrates the circuit design on the membrane. The dipole probe is put in the center of the membrane, which varies in length from $0.32\,\lambda$ to $0.5\,\lambda$ in a set of horns. A four-wire connection is used for the dipole probe to eliminate the effect of the series resistance and contact resistance. The four wires are actually two parallel, coplanar-strip transmission lines on each side of the dipole probe. The bismuth thermal bolometer, made by using a double-layer photoresist-bridge technique, is located in the center of the dipole probe. Both the dipole probe and the microbolometer can be evaporated in the same vacuum (detailed in Chapter 3), which gives the microbolometer much higher responsivity and lower noise.

The dipole probe and the coplanar strip are made of silver with a width of $80\,\mu$m; the spacing between the coplanar strip is $40\,\mu$m, and the characteristic impedance of the coplanar-strip transmission line is $200\,\Omega$ [8]. Near the edge

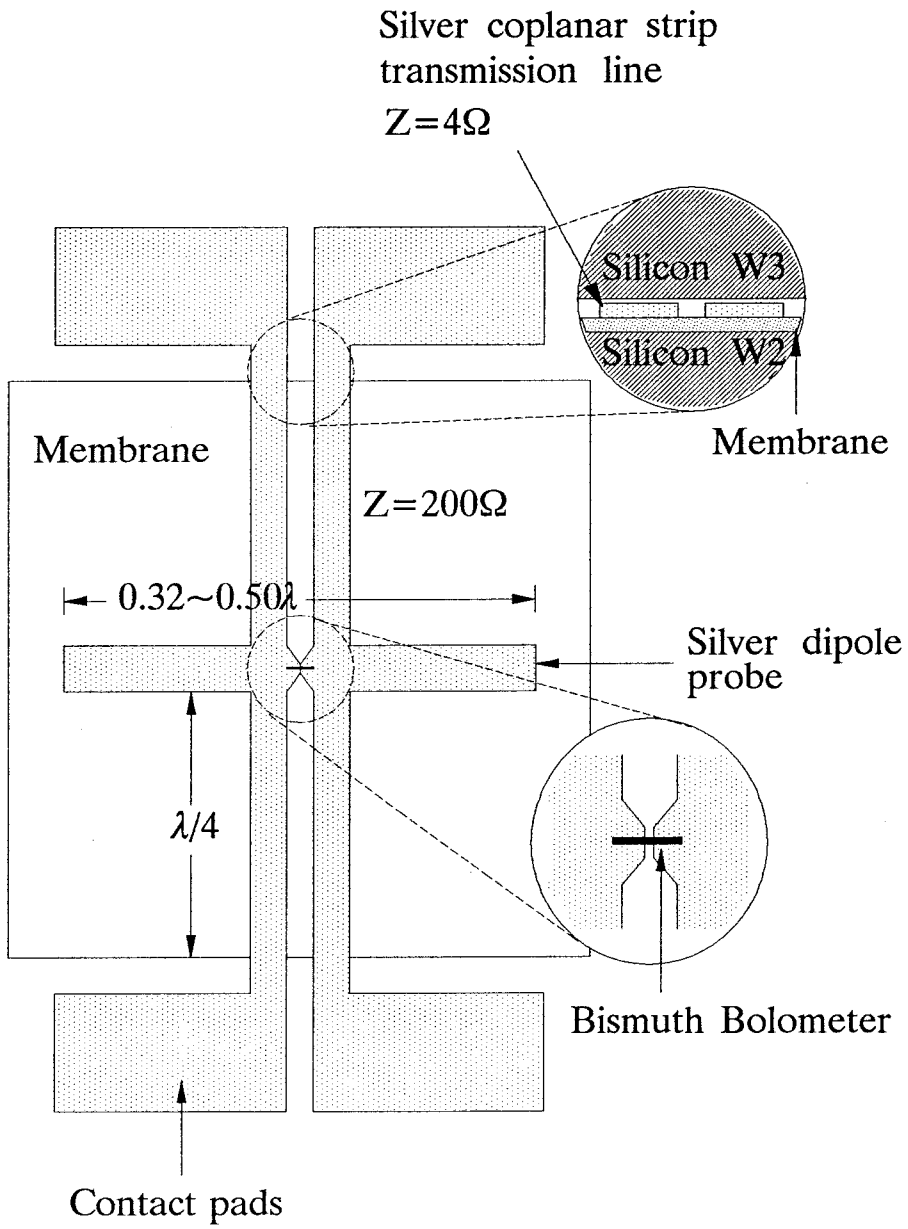

Figure 2.6 The dipole probe, micro-bolometer, and circuit on one of the membranes.

of the membrane, the coplanar strip sandwiched by two silicon wafers has a very low characteristic impedance, about $4\,\Omega$. However, a quarter-wavelength back at the bolometer, it acts as an open circuit. This provides RF isolation. Moreover, because it is a quarter-wavelength, a small impedance variation of the transmission line is not very critical in the design. The transmission lines leading the signal to outside circuits are aligned to the contact pads.

2.4 Power-Density Meter Design

In measuring the antenna aperture-efficiency, knowing the absolute power density at the receiving antenna is essential. Relative power-density measurements at millimeter wavelengths are commercially available. These consist of two principal types: quasi-optical power meters in which the radiation is incident on an absorbing element in free space [9], and wave-guide power meters in which the radiation is coupled by a horn to a fundamental-mode wave-guide and absorbed by an element in the guide. However, absolute power-density measurements are more difficult. With the quasi-optical power meters, the uncertainty comes about from not knowing accurately the absorption coefficient of the detector element. This problem also exists in the wave-guide power meters. Other problems with wave-guide power-meter measurements are the repeatability of connections, calibration of directional couplers, and the uncertainty in standard-gain horns.

Recently, millimeter-wave, power-density meters have been developed whose absorption coefficient is accurately known and whose response can be calibrated at low frequencies. In one approach, radiation is absorbed in a metallic thin film suspended in a gas cell, and a microphone detects the resulting pressure change [10], with a quoted accuracy of 10%. Another approach consists of a thin-film bolometer on a silicon-oxynitride membrane whose responsivity is calibrated with an amplitude-modulated ac current. The resistance change resulting from the incident chopped-millimeter-wave signal is measured with a lock-in am-

plifier [11].

The power-density meter presented in this thesis is a simple design consisting of an evaporated large-area bismuth film on a mylar membrane (Figure 2.7). No vacuum windows are needed; the device is easy to fabricate, and calibration is performed with DC measurements only. This means that no chopping factors or frequency roll-off corrections are required, the device is polarization independent, and the reception patterns are smooth [12].

The large-area bolometer in the power-density meter is a thermal detector whose resistance change is proportional to its thermal impedance. The resistance responsivity in Ω/W is given by

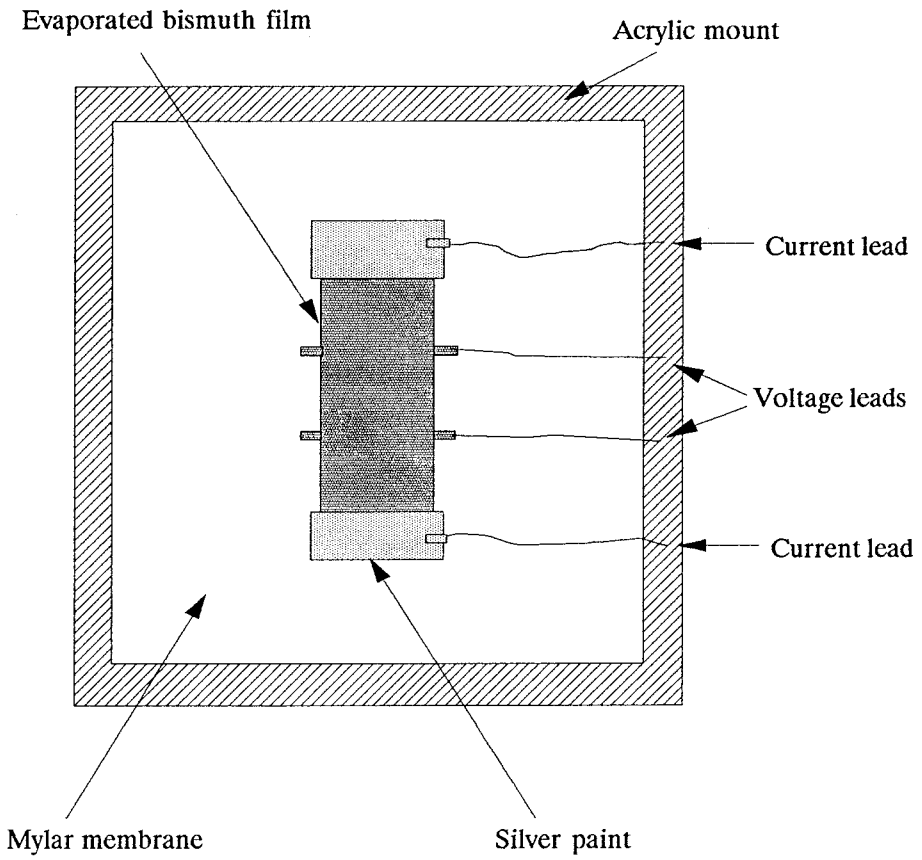

Figure 2.7 Large-area, thin-film, bismuth bolometer on a membrane.

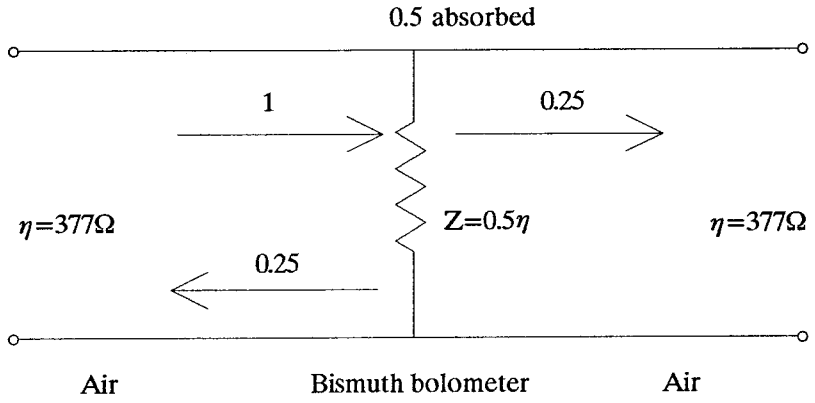

Figure 2.8 Transmission-line model of the thin-film, power-density meter.

$$\mathcal{R}_\Omega = a\alpha R_e R_t \tag{2.7}$$

where a is the millimeter-wave absorptance, α is the temperature coefficient of the bolometer material, R_e is the electrical resistance, and R_t is the thermal resistance. The bolometer is constructed on a 5-μm mylar membrane in order to increase the thermal resistance of the device. The device active-region is $2 \times 2\,\mathrm{cm}^2$. Since the bolometer is much thinner than a wavelength, it can be modeled as a lumped resistance in a transmission-line equivalent circuit (Figure 2.8). The bolometer has an absorption coefficient of 0.5 when it has a sheet resistance of $189\,\Omega$/square. At this sheet resistance, the power-density meter receives its maximum power; therefore, the accuracy of the power-density meter is insensitive to small changes in the resistance change or the angle of incidence.

References

[1] A. Reisman *et al.*, "The Controlled Etching of Silicon in Catalized Ethylene-Diamine-Pyrocatechol-Water Solutions," *J. Electrochemical Soc.*, vol. 126, pp. 1406–1425, 1979.

[2] K. E. Peterson, "Silicon as a Mechanical Material," *Proc. IEEE,* vol. 70, pp. 420–457, May 1982.

[3] G. Rebeiz, D. Kasilingam, Y. Guo, P. Stimson, D. Rutledge, "Monolithic Millimeter-Wave Two-Dimensional Horn Imaging Arrays," *IEEE Transactions on Antennas and Propagation*, Vol. 38, pp. 1473–1482, September, 1990.

[4] C. A. Balanis, *Antenna Theory and Design,* Chap. 11, Harper and Row, New York, 1984.

[5] R. F. Harrington, *Time-Harmonic Electromagnetic Fields,* McGraw-Hill, New York, 1961.

[6] W. L. Williams, R. C. Compton and D. B. Rutledge, "Elf: Computer Automation and Error Correction for a Microwave Network analyser," *IEEE Trans. Instrum. Measurements,* vol. 37(1), pp. 95–100, 1988.

[7] R.C. Compton, S.W. Wedge, D.B. Rutledge, "*Puff*: Computer-Aided Design for Microwave Integrated Circuits," published at Caltech, January, 1990.

[8] K.C. Gupta, R. Garg, I.J. Bahl, *Microstrip Lines and Slotlines,* Chap. 7, Artech House, Inc., Dedham, MA, 1979.

[9] F. B. Foote, D. T. Hodges, and H. B. Dyson, "Calibration of Power and Energy Meters for the Far Infrared/Near Millimeter Wave Spectral Region," *Int. J. Infrared Millimeter Waves,* Vol. 2, No. 4, pp. 773–782, 1981.

[10] Thomas Keating Ltd., Billingshurst, West Sussex, England.

[11] C. C. Ling, G. M. Rebeiz, "A Wideband Monolithic Submillimeter-Wave Quasi-Optical Power Meter," *IEEE MTT-S International Microwave Symposium*, May, 1990, Dallas, Texas.

[12] K. Lee, Y. Guo, P. Stimson, K. Potter, D. Rutledge, "Thin-Film Power-Density Meter for Millimeter Wavelengths," *IEEE Transactions on Antennas and Propagation*, Vol. 39, pp. 425–528, March, 1991.

Chapter 3

Integrated-Circuit Horn-Antenna Array Fabrications

Silicon is being increasingly used in a variety of new applications not because of its well-established electronic properties, but rather because of its excellent mechanical properties. Similarly, silicon is employed in the horn antenna array used more as a mechanical material rather than as an electronic material. Silicon has anisotropic properties and can be etched by an anisotropic etchant to form horn-shaped cavities. In addition, silicon is inexpensive and can be easily batch-fabricated by the standard photolithography techniques. The horn antenna array consists of a stack of silicon wafers with etched horns in them. Once the aperture size and the antenna-probe position inside the horn are determined, the thickness of the silicon wafers and the window size on the masks for each wafer can be designed accordingly so that pyramidal horns can be produced with smooth sidewalls when these wafers are assembled. Antenna probes and circuits are integrated on the silicon-oxynitride membranes, which are suspended inside the horns. Making low-residual-stressed membranes is a critical step in the horn-antenna-array fabrication process. Since the antenna probes are suspended on the membrane, they radiate effectively in the free space; therefore, they do not have any dielectric substrate loss. Furthermore, there is plenty of space between the horns for transmission lines.

3.1 Etching Horns in Silicon

The horn antenna array consists of a set of four anisotropic-etched, n-type-doped silicon wafers, including a membrane wafer (W2 in Figure 2.1, Chapter 2). The horns are made by coating both sides of silicon wafers with a protection layer, silicon-oxynitride for the membrane wafer, and silicon-dioxide for other wafers. The silicon-dioxide layer is made by thermal oxidation because this is a quick and easy way to grow protection layers. The thickness of the silicon-dioxide is usually about 1.5 μm. The photoresist pattern is defined on one side of the wafer and the other side is protected by a glass slide with a layer of photoresist between them. The protection layer on the front side is first etched off by buffered HF acid. Then the photoresist and the glass slide are removed. The wafer with open windows on the front side and protection layer on the back is ready for EDP etching. EDP, or Ethylene-Diamine Pyrocatechol solution, an anisotropic etchant developed about 20 years ago [1,2], etches silicon (100) crystal planes much faster than (111) planes, because the (111) planes in the silicon have the highest atom density of any other crystal planes. It is necessary to point out that EDP is highly dopant-dependent, exhibiting near-zero etch rates on highly boron-doped silicon, but etches well on phosphorus-doped silicon, namely, n-type silicons. The anisotropic etch-rate ratio of (100) over (111) is about 50:1 experimentally. The etching rate for (100) plane is usually about 50 μm/hour at 110 C°. This forms pyramidal cavities in the silicon bounded by (111) crystal planes. The angle between (100) and (111) planes in the silicon is 54.74°; the horn flare angle is 70.52° [3]. Although this angle is larger than desirable for horn antennas, it is possible to achieve smaller flare angles with ion-beam milling or reactive-ion etching, but it is expensive and needs special masks. EDP etching, however, is a very inexpensive chemical etching process. Additionally, it has good repeatability and can be easily masked by a variety of materials, such as silicon-dioxide, silicon-nitride, chromium or gold [4].

Silicon has a cubic crystal structure. Some simple crystal planes are illustrated in Figure 3.1 (a). When etching horns in silicon, it is necessary to align the edge of the mask windows to a (110) plane, as shown in Figure 3.1 (b). The horn opening is in the (100), but each edge of the square opening is in the (110) plane. The four neighboring (111) planes form the sidewalls of the horn. If a misalignment happens, it will increase the size of the etched pyramidal cavity or possibly will break the walls between the cavities [5,6]. This is because etching through silicon wafers with a thickness of a few hundred micrometers is a long-time etching, and undercut etching is unavoidable. Moreover, EDP has a fast convex undercut-etching rate. Figure 3.2 illustrates the general EDP anisotropic etch-undercutting rules when the silicon wafer is etched long enough [7]. The pattern on the left-hand side shows that an arbitrarily shaped, closed pattern masked by a silicon-dioxide layer will result in a rectangular cavity in the silicon, bounded by the (111) planes and oriented in the <110> direction. The pattern on the right-hand side shows a misaligned rectangular horn resulting in a larger rectangular horn. When it is etched through, it leaves a freestanding silicon-oxynitride membrane on the other side. The membrane dimension $W_2 = W_1 - 2t\tan(35.26°) \approx W_1 - \sqrt{2}t$.

Accurate alignment of the surface pattern to the crystal plane is necessary to achieve good dimensional control. The misalignment undercut error needs to be controlled under a certain degree, especially for the front wafer W1. The horn openings of W1 need to be as close as possible to get the maximum receiving area while leaving enough tolerance for the undercut error to avoid destroying the horns. If a rectangular-shaped mask is misaligned by an angle θ, indicated in Figure 3.2 (a), then the original $W \times d$ rectangle becomes $W_1 \times d_1$; $W_1 = d\sin\theta + W\cos\theta$ and $d_1 = W\sin\theta + d\cos\theta$. The maximum relative error introduced is $(d_1 - d)/d = 2\sin\theta + \cos\theta$, assuming that $W = 2d$. If $\theta \leq 1°$, then $(d_1 - d)/d \leq 3\%$. This $\theta \leq 1°$ can be achieved by cutting (100) silicon wafers right on

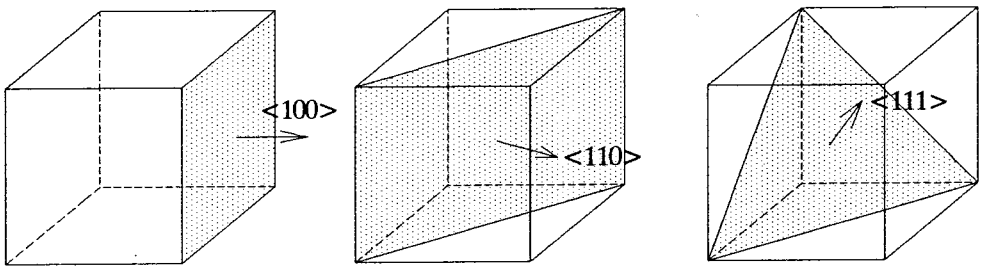

(100) Plane (110) Plane (111) Plane

(a)

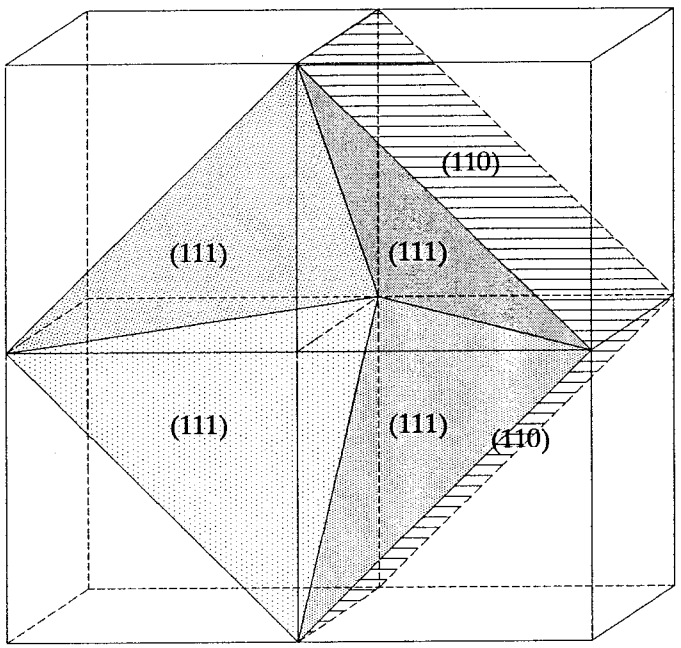

(b)

Figure 3.1 A few simple crystal planes in silicon and their corresponding crystal <directions> (a); a horn bounded by four (111) planes, and the edges are in (110) planes (b).

the (110) plane; then the edge of the pattern is aligned to that (110) plane. Alternatively, a long, narrow groove can be etched first roughly along the (110) plane until the two (111) planes converge to one line in the (110) plane, like the

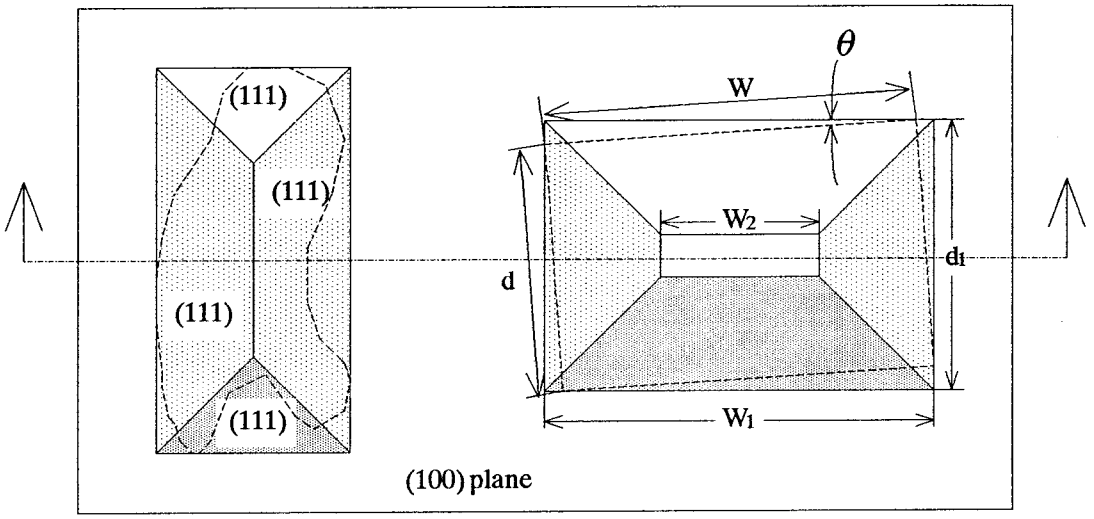

(a)

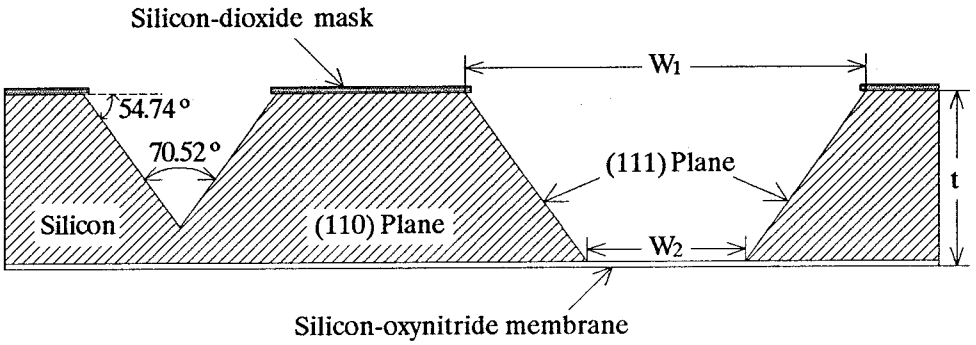

(b)

Figure 3.2 Illustration of pyramidal cavities etched into a (100) silicon wafer with a silicon-dioxide mask, using the anisotropic etch EDP (a); cross-sectional view of the silicon wafer (b).

pattern on the left-hand side in Figure 3.2. Later, this long line in the (110) plane can be used as an alignment mark. In the design, spacing between the horns on W1 is about 80 μm, and the opening of the horn is 1.0 λ. Other wafers in the back are of less concern because the horns are far apart.

The pictures in Figure 3.3 show etched silicon wafers W1, W3 and W4 with a 7×7 horn array on them. After etching, these wafers need to be thoroughly cleaned before being coated with gold to make them highly conducting. Notice that W3 is not completely coated with gold as the other two wafers are, but it

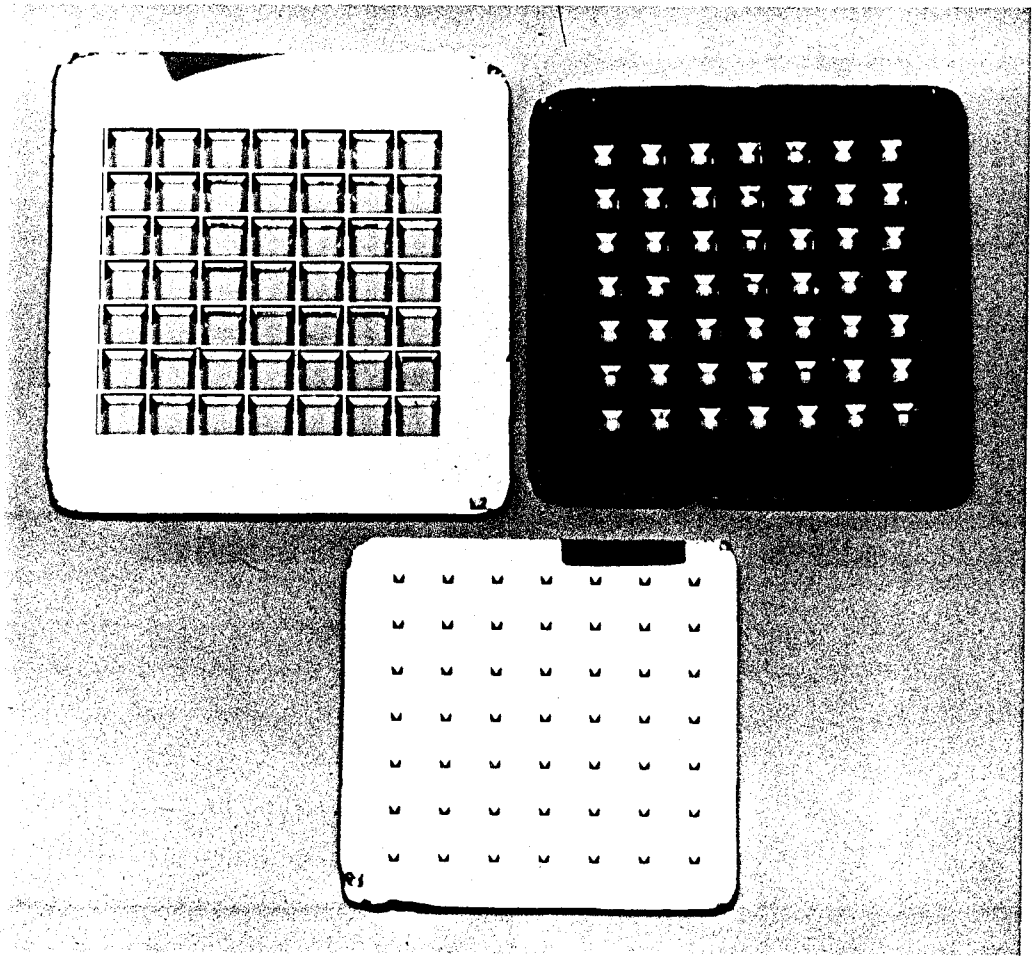

Figure 3.3 Photographs of 7×7 horn arrays etched in the (100) silicon wafers of W1, W3 and W4 by using anisotropic EDP.

has gold only on the sidewalls. This is because W3 is next to the membrane on which all the circuits are located; therefore, W3 needs to keep its silicon-dioxide as an insulating layer to isolate the low-frequency transmission lines.

3.2 Membrane Deposition and Stress Analysis

The membrane is made by coating a silicon wafer with a thin film of silicon-oxynitride, using a plasma-enhanced, chemical-vapor deposition (PE-CVD) [8]. Then the supporting silicon in the defined windows is etched off, resulting in free-standing membranes. To produce mechanically strong, free-standing membranes, the mechanism of the broken membrane needs to be studied. Normally, broken membranes are caused by residual stress σ_R in the membrane when a square portion of the supporting substrate is removed, or a stress σ_P produced by a pressure difference, or a combination of the two.

When a film with stress is deposited on a thin silicon substrate, the substrate will bend by a measurable degree. A tensile stress will bend the substrate to a concave, while a compressive stress will bend it to a convex. Figure 3.4 (a) shows a tensile-stressed membrane silicon wafer, which is bent concavely. Upon etching away a square substrate region, the membrane relaxes from position 1 to position 2, shown in Figure 3.4(b). This relaxation causes the residual stress to be less than the initial residual stress in the film. This will produce flat and rigid membranes under the condition that the residual stress σ_R is less than the tensile strength of the silicon-oxynitride, σ_B, which is estimated to be around $4 \times 10^4\,\mathrm{N/cm^2}$. On the other hand, on a compressive-stressed membrane wafer, the membrane breaks easily when a portion of the substrate is etched away. The strength of the membrane can be expressed in terms of hydrostatic strength Q, defined as the pressure differential across the membrane sufficient to cause it to rupture. For a square membrane, a break occurs first at the center, when the internal stress in the membrane is equal to the tensile strength σ_B of the film.

The hydrostatic strength is given by [9,10]

$$Q = \frac{2Ed}{L}\left(\frac{\sigma_B - \sigma_R}{K(\nu)E_f}\right)^{3/2} \tag{3.1}$$

where E, ν, L and d are Young's modulus, Poisson's ratio, the edge length and the thickness of the film, respectively. The function $K(\nu)$ is given by

$$K(\nu) = 0.323\ \frac{(1-\nu^2)^{2/3}}{1-\nu} \tag{3.2}$$

Poisson's ratio for the silicon-oxynitride is around 0.2. This gives $K(\nu)$ of 0.39. To increase the hydrostatic strength, the residual stress σ_R needs to be reduced. The residual stress of the silicon-oxynitride can be measured [11] and is given by

$$\sigma_R = \frac{E_s}{3(1-\nu_s)}\frac{d_s^2}{{r_s}^2}\frac{h}{d_f} \tag{3.3}$$

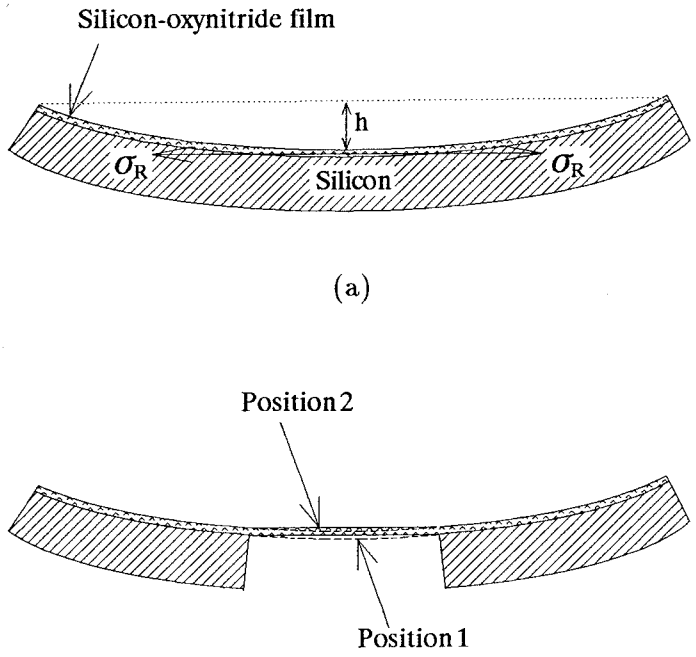

Figure 3.4 A film with tensile stress grown on a thin silicon substrate (a); when a portion of silicon is etched away (b).

where E_s, ν_s, d_s and r_s are Young's modulus, Poisson ratio, the thickness and the radius of a circular substrate, respectively. For a (100) silicon substrate, ν is between 0.2 and 0.25, and the value of $\frac{E_s}{(1-\nu)}$ is 1.8×10^7 N/(cm)^2. h is deflection of the substrate caused by residual stress shown in Figure 3.4 (a), and d_f is the film thickness. Both h and d_f can be measured by a surface-profile machine, DekTak. Figure 3.5 shows the typical measured results of deflection h and film thickness d_f as a function of distance. In the d_f measurement, the film is etched off, masked by equally spaced windows, resulting in a step function like surface profile. The thickness is taken as an average of these steps. For a 1.5 inch radius and 550 μm-thick silicon wafer, with measured $h = 3.1\,\mu$m and $d_f = 1.5\,\mu$m, the residual stress is calculated to be $9700\,N/(\text{cm})^2$.

The film is grown using gases of nitrous oxide (N_2O), ammonia (NH_3) and

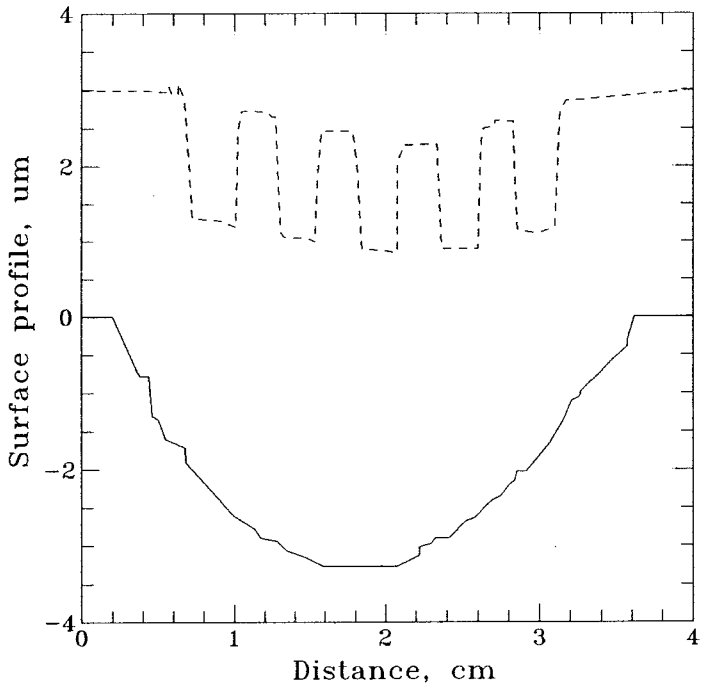

Figure 3.5 Measured profile on a stressed silicon substrate (dashed line); a substrate with evenly spaced film windows (solid line).

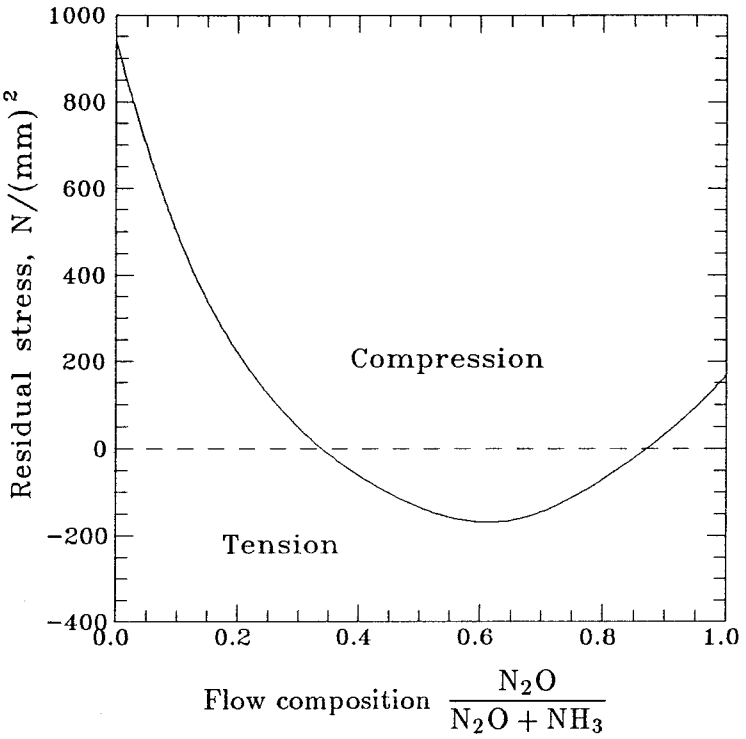

Figure 3.6 Residual stress as a function of relative gas-flow rates.

silane (SiH_4) [12]. The residual stress in the film can be controlled by regulating the relative gas-flow rates of nitrous oxide N_2O and ammonia NH_3. This is shown in Figure 3.6, which indicates that films with tensile, compressive or with no residual stress may be produced [13]. After many testings and readjustments, the optimal operating conditions listed in Figure 3.7 have been adopted.

The deposition temperature is 350°C and the pressure in the chamber is 2.0 Torr. An RF power density of 0.012 W/cm^2 is used, with an RF frequency

Gases	SiH_4	N_2O	NH_3	Unit
Flow rate	250	500	1500	SCCM
Flow control	2.5	0.84	2.5	Volt

Figure 3.7 Optimal gases flow rate for making low residual-stress film.

of 440 KHz. The 7×7 membrane array is built on this kind of low residual-stress film wafer, with a membrane size of 1.8×1.8 mm. These membranes have withstood all standard fabrication procedures, such as photoresist spinning, contact exposure, evaporation in the vacuum and photoresist liftoff. The lowest residual stress of $420\,\mathrm{N/(cm)^2}$ has been tested. With such a low residual-stress film, a large area membrane as big as 13×13 $(\mathrm{mm})^2$ has been made.

3.3 Dipole Probes and One-Step Thermal Bolometers

Dipole probes, thermal bolometers and low-frequency transmission lines are integrated monolithically on the membrane surface by the standard semiconductor-photolithography techniques. Silver is used for the dipole probes, bismuth for the thermal bolometers and gold for the transmission lines. The dipole probes and transmission lines are first defined. The bismuth-bolometer, photoresist pattern is then aligned to the dipole probes; bismuth is evaporated and finally the liftoff is performed. The contact between bismuth and silver, however, used to be a problem. This is illustrated in Figure 3.8 (a) and (b). After the liftoff of silver, a pair of sharp, thin edges of silver near the opening is left behind. When, bismuth is evaporated onto the silver, the bismuth will be cut into three segments like a broken circuit. One way to avoid this is to give the photoresist surface a special treatment, e.g., to sink the substrate in chlorobenzene for a few minutes before developing [14,15]. As a result, it gives an overhanging photoresist profile, as shown in Figure 3.8 (c). This will produce a smoother silver edge for a better contact between the silver and the bismuth.

There are two major disadvantages of evaporating silver and bismuth separately. First, for small dipole probes and small bolometers, the alignment between the two becomes very critical. Secondly, the noise is pretty high compared with the two metals evaporated without breaking the vacuum, or the one-step process [16]. The one-step process is a photoresist bridge technique, utilizing

double layers of the photoresist with a CF_4 plasma buffer layer in between [17]. But this process is not stable and does not have good repeatability, because of the uncertainty of the CF_4 buffer layer produced by a plasma etcher in our laboratory. The buffer layer used in the current process is a thin layer of aluminum. The illustration of this process is shown in Figure 3.9.

After the first-layer photoresist is spun on the substrate, it is flush-exposed. A thin layer of aluminum is then evaporated on top of it, followed by spinning the second layer of the photoresist. Then, this second layer of the photoresist is

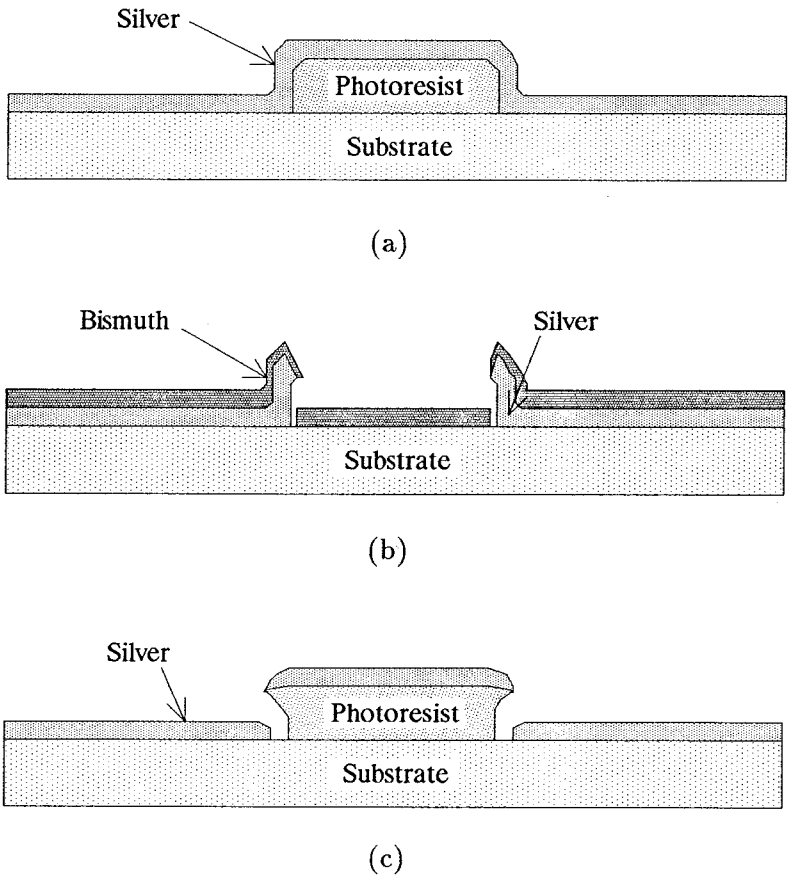

Figure 3.8 Silver deposited on photoresist-patterned substrate (a); bismuth evaporated on the substrate after silver liftoff (b); the overhanging photoresist profile produces smooth silver edges (c).

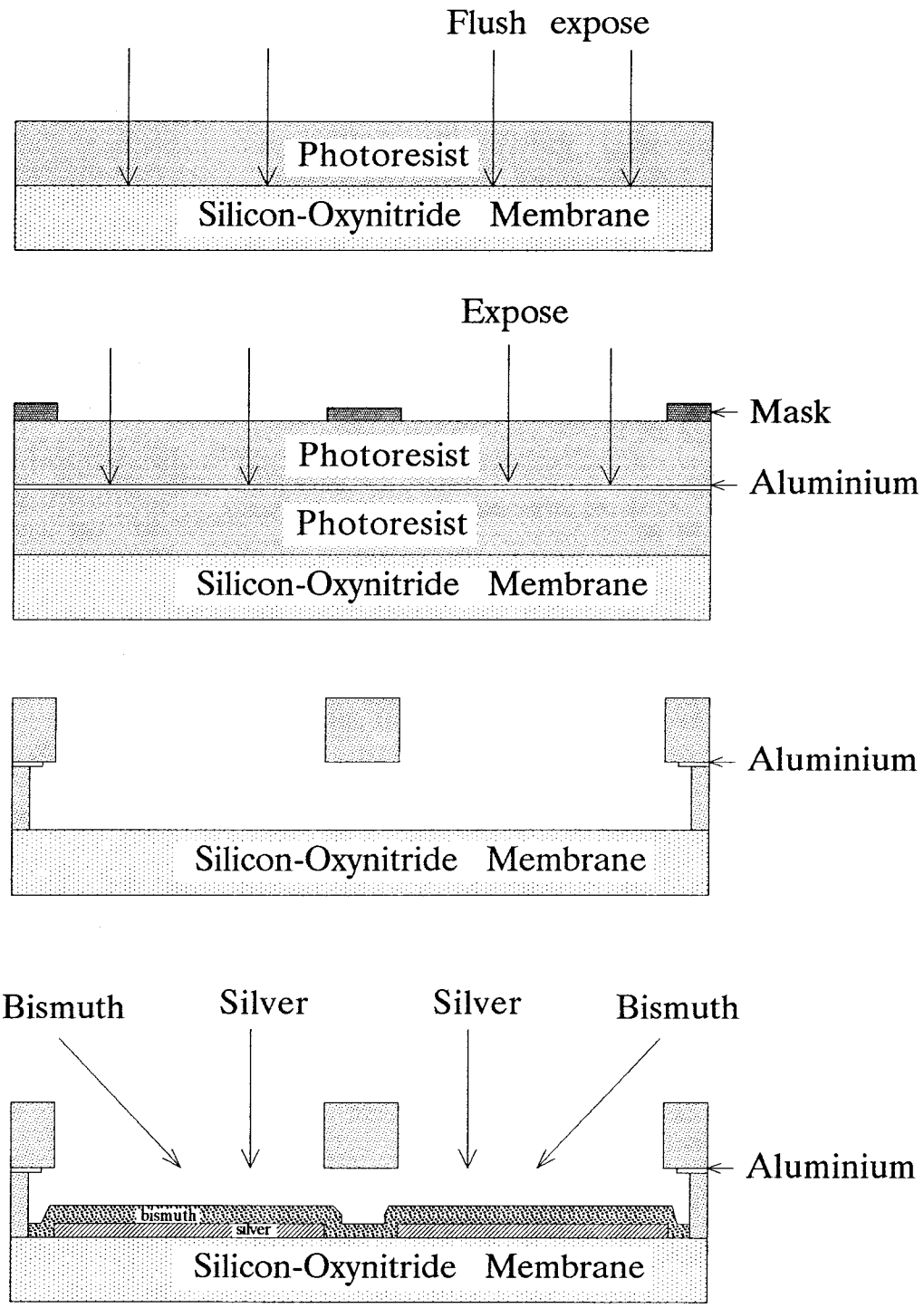

Figure 3.9 Photoresist bridge with a buffer layer of aluminum to produce one-step microbolometer.

mask-exposed. After the top layer photoresist is developed, the aluminum in the opened window is etched off. The bottom layer of the photoresist is then overdeveloped. Because the gap in the center is very narrow (4 μm), overdeveloping will get out the bottom layer exposed-photoresist but will leave a suspended photoresist bridge on the top. Afterwards, silver is evaporated normal to the substrate and bismuth is evaporated with an angle from both sides. In evaporating bismuth, a voltmeter is connected to a sample dipole probe, so that the resistance of the bismuth bolometer can be monitored and controlled. The thickness was about 1500 Å for a resistance of 90 Ω. A photograph of such a bridge is shown in Figure 3.10, taken by a scanning electron microscope (SEM). Figure 3.11 shows before and after the evaporation and liftoff on such a bridge, taken by a Polaroid

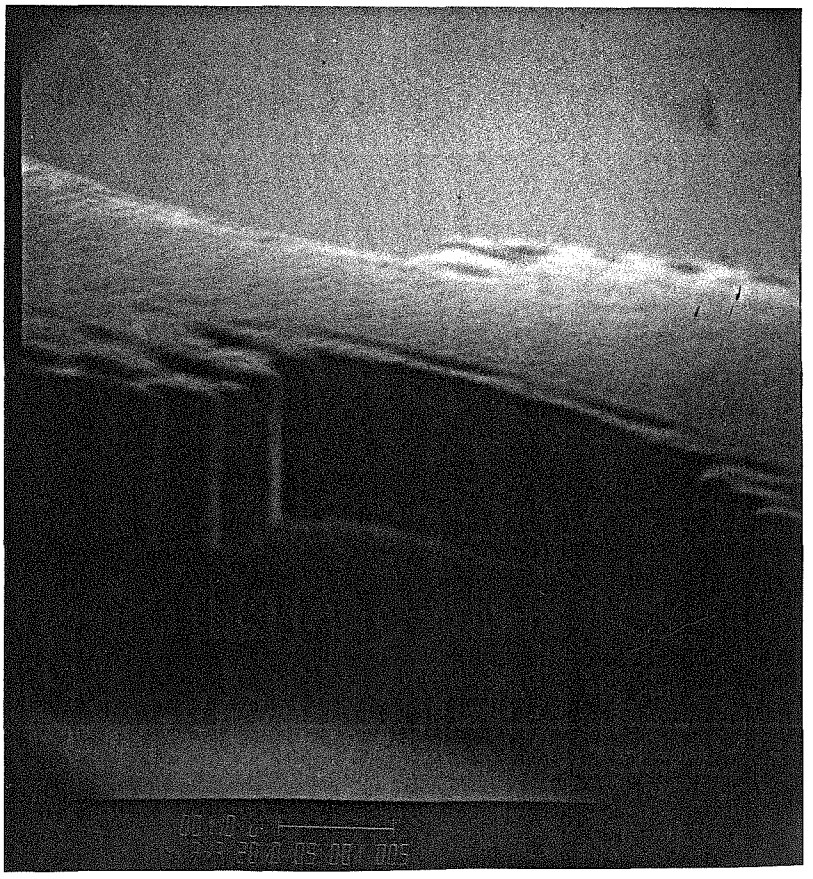

Figure 3.10 Photoresist bridge on the membrane taken by SEM.

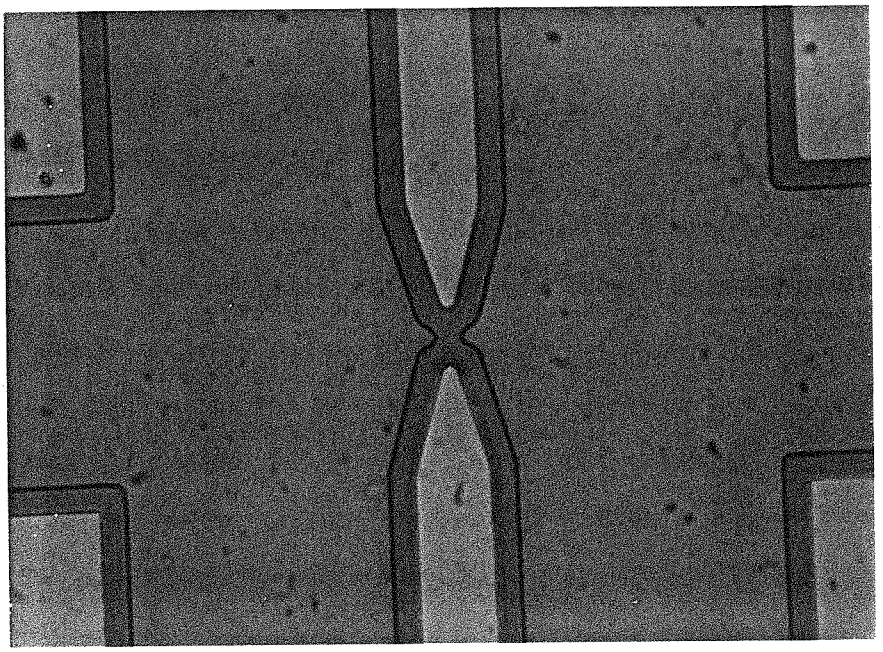

(a)

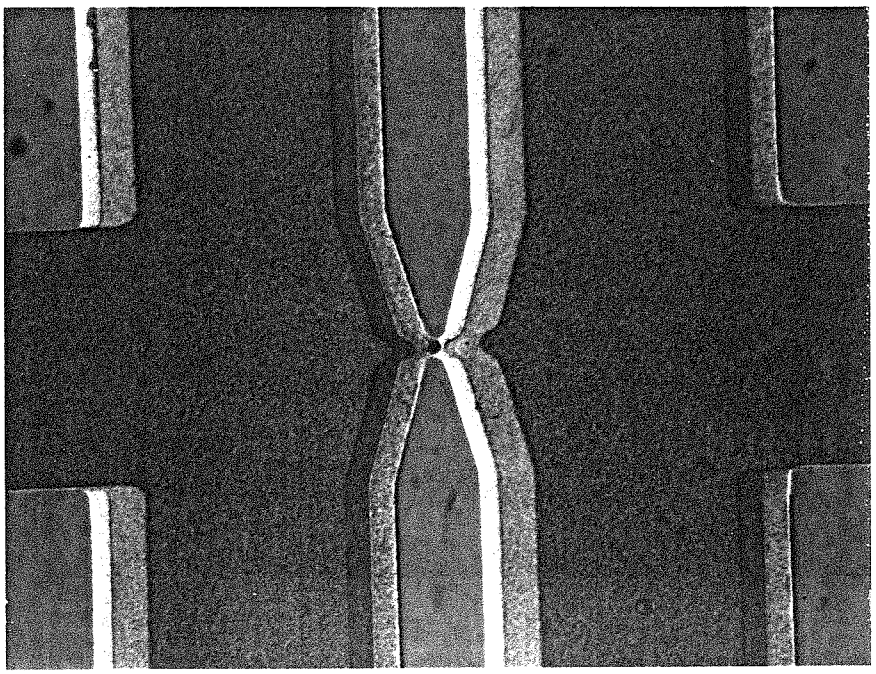

(b)

Figure 3.11 Photoresist bridge before (a) and after (b) the evaporation and liftoff.

camera through a high-magnification microscope. Because the dipole probes and bolometers are suspended on the membrane, they effectively radiate in the free space; therefore, they do not have any dielectric substrate loss.

3.4 Coating Horn Sidewalls with Gold

All the wafers need to be coated with gold on the sidewalls before assembling in order to eliminate resistive losses. The wafers were easily coated with gold except for the membrane wafer. This is because the membranes would also have been covered over during the evaporation. To solve this problem, quite a few methods have been attempted. One of them was to cover the membrane with the photoresist before evaporation, using either positive or negative photoresist.

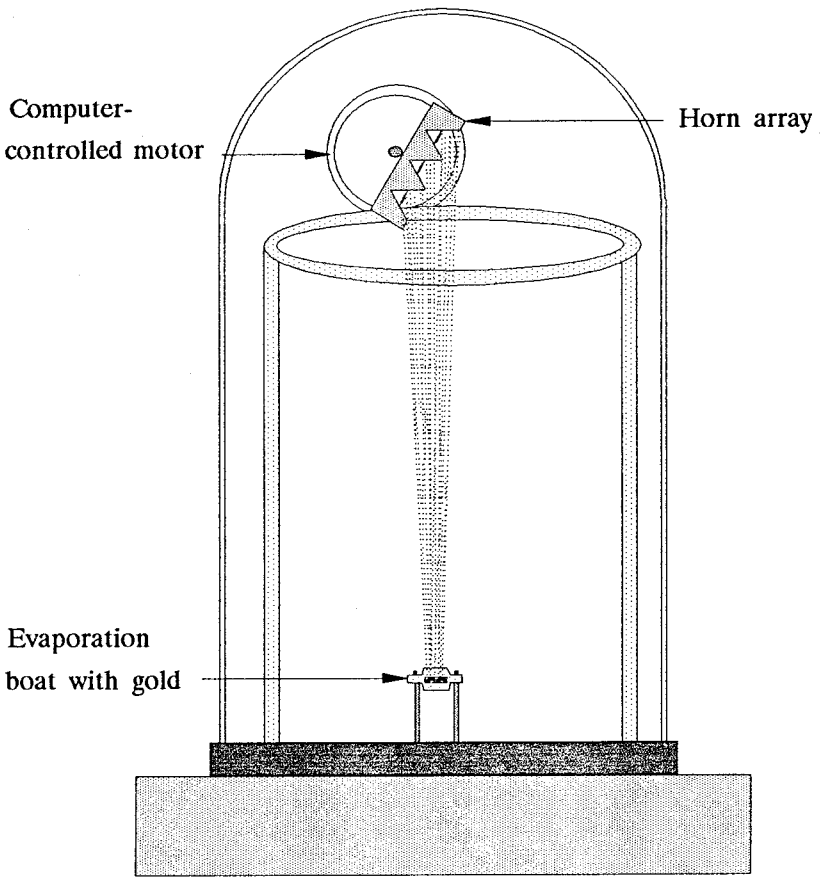

Figure 3.12 Gold coating the sidewalls with a tilted substrate.

This method was proved to be unsuccessful because the photoresist accumulated in the cavity was too thick to be exposed and developed properly. Another way is electric plating of gold on the sidewalls, since doped silicon conducts pretty well at room temperature. In doing so, unfortunately, the gold was not well confined on the horn sidewalls, but spread over onto the membranes. Furthermore, the gold accumulated on the sidewalls very loosely; consequently, annealing was necessary in the process. Most membranes could not withstand temperatures higher than 300 C° in the annealing process. In an attempt to look for alternatives, an easier way was found, namely, by evaporating gold with a tilted substrate, as shown in Figure 3.12. The opening of the horn automatically forms a shadow, which blocks the membrane from the gold vapor. A small computer-controlled motor is connected to the substrate chuck, so that the substrate can be rotated easily between the evaporations of the different sides. This coating process can be done either before or after the wafers' assembly. As a matter of fact, this is normally done not only after the wafers' assembly, but also after the first time of the efficiency measurement, so that the aperture efficiencies before and after the gold-coating sidewalls can be compared.

Photographs of the membrane wafer are shown in Figure 3.13, in which the antenna probes, bolometers, and circuits have already been laid out on the membrane surface. Notice that the membrane side is going to face the apex of the horn when the four silicon wafers are assembled. Figure 3.14 shows the picture of a full 7×7 antenna array operating at 93 GHz, with entire sidewalls having been coated with gold.

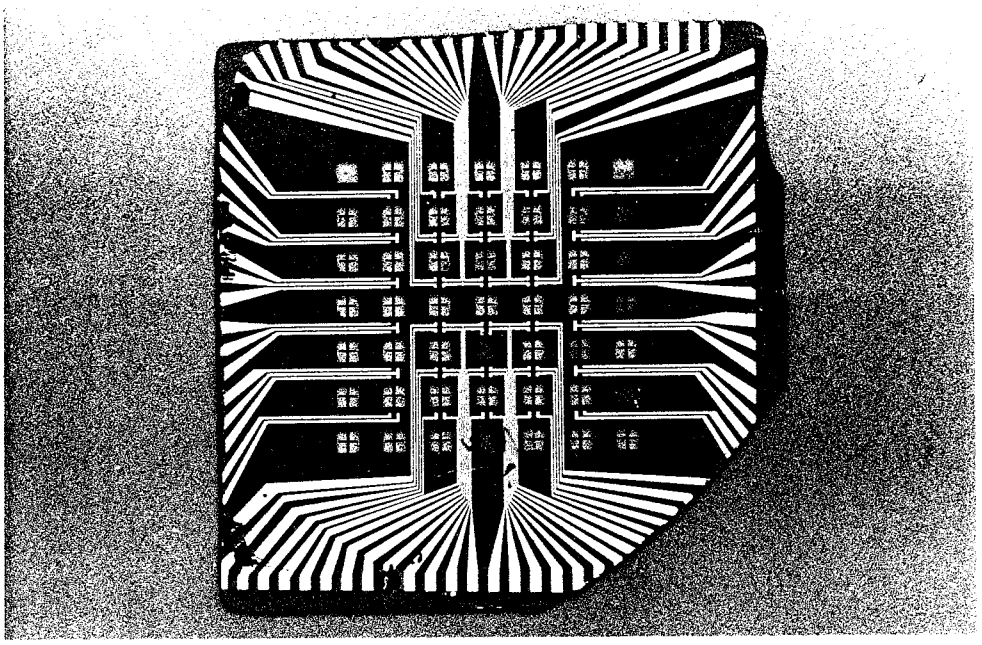

(a)

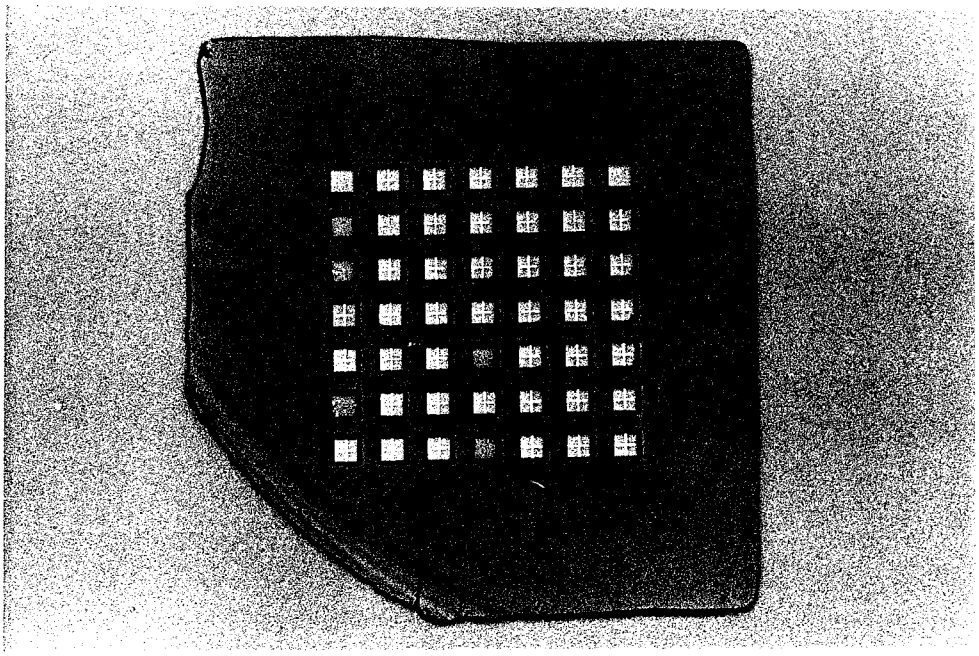

(b)

Figure 3.13 Photographs of the membrane wafer, looking from the membrane side (a); and looking from the opposite side (b).

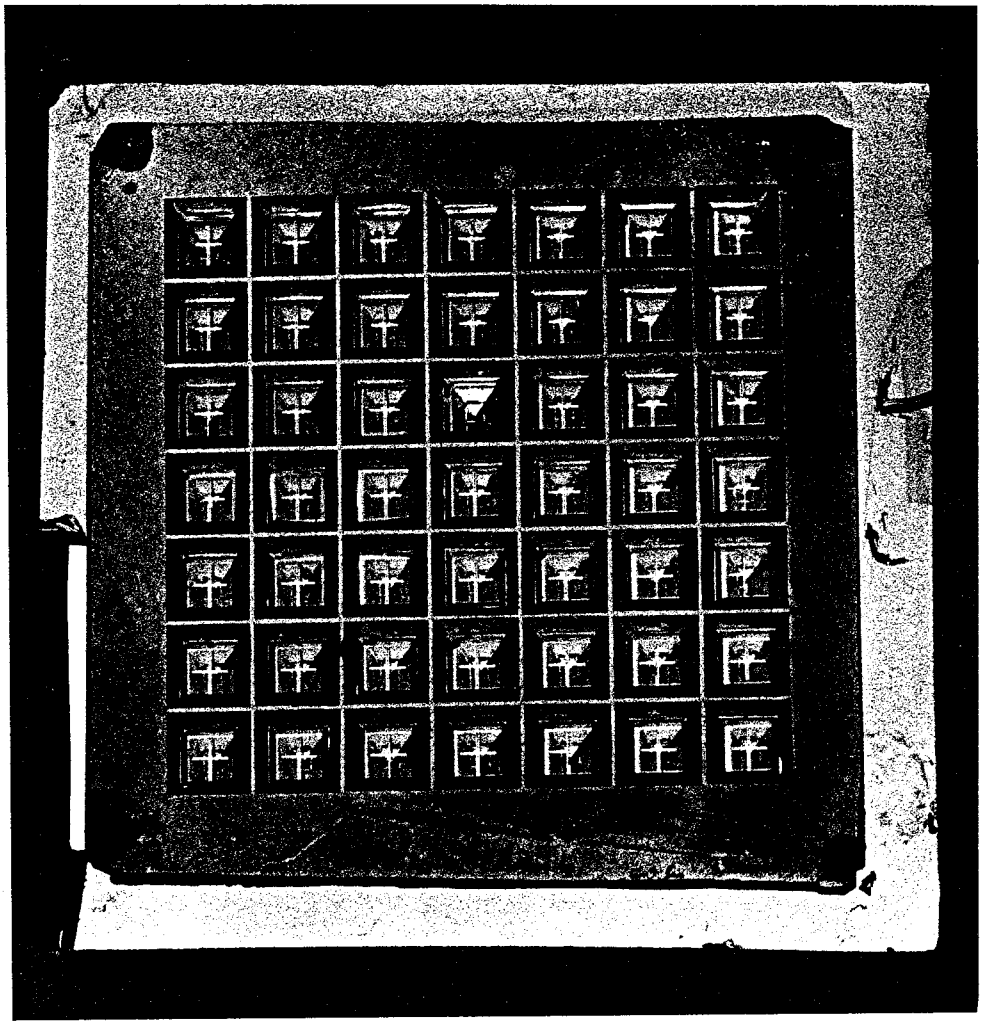

Figure 3.14 The full 7×7 horn antenna imaging array, with entire sidewalls coated with gold, working at 93 GHz. The opening of each horn is 1λ or 3.2 mm, and the whole device size is about $3.5 \times 3.5\,\mathrm{cm}^2$.

3.5 Fabrication of the Power-Density Meter

In the process of making the power-density meter, a 5-μm-thick mylar sheet is first glued on an acrylic frame (shown in Figure 2.7). This is done by stretching the mylar sheet flat using an embroidery loop, then epoxy-gluing the mylar onto the acrylic frame. The bismuth film is evaporated through a metal mask onto the mylar until the DC sheet resistance is 189 Ω. The thickness is about 500 Å. This sheet resistance gives the maximum absorptance of 0.5 by the thin film. Bismuth is chosen as the bolometer material because of its high temperature coefficient, measured to be $0.0026\,\mathrm{K}^{-1}$. The bolometer is surrounded by 5-cm styrofoam blocks to reduce convection heat loss to the air and to block infrared radiation. By placing the structure in an absorbing beam dump, reflections and other unwanted signals are minimized (Figure 3.15). The bolometer has a time constant of 1 minute, which appears to be determined by thermal diffusion through the styrofoam. The attenuation at 93 GHz in the styrofoam is measured to be less than 0.01 dB/cm, so that its effect on the measurements is negligible.

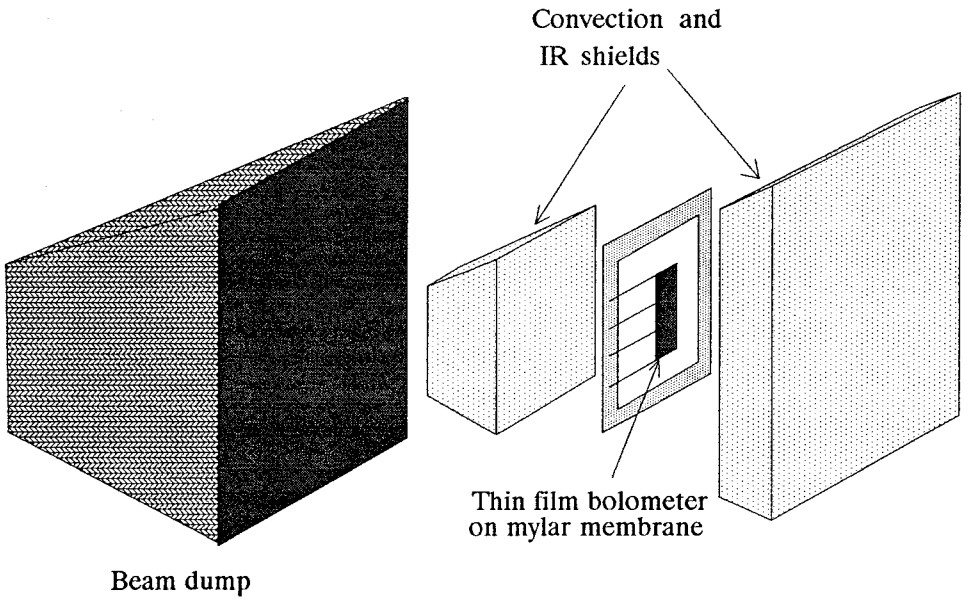

Figure 3.15 The power-density meter with the bolometer embedded in styrofoam.

In addition, the absorptance is independent of polarization and frequency. The geometry of the device allows for a four-point measurement, which eliminates the effect of resistance in the contacts because the biasing leads are separate from the voltage-sensing leads. The bolometer is a $2\times2\,\mathrm{cm}^2$ square and is much thinner than the skin depth in bismuth at millimeter wavelengths ($5\,\mu\mathrm{m}$ at $93\,\mathrm{GHz}$), so the RF sheet resistance is the same as the DC resistance, which can also be monitored and controlled during the bismuth evaporation.

References

[1] J.C. Greenwood, "Ethylene Diamine-Catechol-Water Mixture Shows Preferential Etching of P-N Junctions," *J. Electrochem. Soc.*, vol. 116, pp. 1325, 1969.

[2] A. Bohg, "Ethylene Diamine-Pyrocatechol-Water Mixture Shows Etching Anomaly in Boron-Doped Silicon," *J. Electrochem. Soc.*, vol. 118, pp. 401, 1971.

[3] N.W. Ashcroft, N.D. Mermin, *Solid State Physics,* Chapter 4, Holt, Rinehart and Winston, New York, 1976.

[4] A. Reisman *et al.*, "The Controlled Etching of Silicon in Catalized Ethylene-Diamine-Pyrocatechol-Water Solutions," *J. Electrochemical Soc.*, vol. 126, pp. 1406–1425, 1979.

[5] D.L. Kendall, "On Etching Very Narrow Grooves in Silicon," *Appl. Phys. Letter*, vol. 26, pp.195, 1975.

[6] E. Bassous, "Fabrication of Novel Three-Dimensional Micro-structures by the Anisotropic Etching of (100) and (110) Silicon," *IEEE Trans. Electron Devices*, vol. ED-25, pp. 1178, 1978.

[7] K. E. Peterson, "Silicon as a Mechanical Material," *Proc. IEEE,* vol. 70, pp. 420–457, May 1982.

[8] D. W. Hess, "Plasma-Enhanced CVD: Oxides, Nitrides, Transition Metals, and Transition Silicides," *J. Vac. Sci. Technol.* vol. 2, pp. 244–252, April–June, 1984.

[9] M. Sekimoto, H. Yoshihara, and T. Ohkubo, "Silicon Nitride Single-Layer X-Ray Mask," *J. Vac. Sci. Technol.*, vol. 21, pp. 1017–1021, Nov.-Dec., 1982.

[10] S. Timoshenko and S. Woinowsky-Krieger, *Theory of Plates and Shells*, McGraw Hill, New York, 1959.

[11] L. I. Maissel and R. Glang, *Handbook of Thin Film Technology*, pp. 12-21 to 12-30, McGraw-Hill, New York, 1970.

[12] Pacific Western Systems, Model GL–450G–L–450 Coyote Catalog.

[13] Courtesy of W.R. Snow, Pacific Western Systems.

[14] M. Hatzakis, B.J. Canavello, J.M. Show, "Single-Step Optical Liftoff Process," *IBM J. Res. Develop*, vol. 24, No. 4, pp. 453–460, July, 1980.

[15] G.G. Collins, C.W. Halsted, "Process Control of the Chlorobenzene Single-Step Liftoff Process with a Diazo-Type Resist," *IBM J. Res. Develop*, vol. 26, No. 5, pp. 596–604, September, 1982.

[16] D.P. Neikirk, Wayne W. Lam, D.B. Rutledge, "Far-Infrared Microbolometer Detectors," *International Journal of Infrared and Millimeter Waves*, Vol. 5, No. 3, 1984.

[17] D.M. Dobkin, B.D. Cantos, "Plasma Formation of Buffer Layers for Multilayer Resist Structures," *IEEE Electron Device Letters*, vol.EDL-2, No. 9, September 1981.

Chapter 4

Horn-Antenna Array Efficiency Measurements

The aperture efficiency of a single horn in the array is defined as the power received by the detector in the horn divided by the total power incident on the horn aperture, when the array is illuminated by a plane wave. Accurate calibration of the microbolometer and the power-density meter is crucial in the aperture-efficiency measurements of the horn antenna arrays. Responsivities of both microbolometers in the horns and the bolometer in the power-density meter can be obtained through measurements. Considerations and tests have been made for different sources of errors, such as resistance drift, source-power drift, edge effects, time constants and varying angles of incidence. In order to simplify the measurement and increase the accuracy, a complete DC method has been developed on millimeter-wave, absolute power-reception measurements, in contrast to a modulated RF power-reception measurement which was used before. In the measurements, a klystron was used to provide the 93-GHz RF power. Signal changes were measured by Hewlett-Packard multimeters and data were collected, calculated and plotted by PC computers. As an initial test for the antenna-mixer array development, beam-lead Schottky diodes were introduced into the array, on which both environmental and electrical tests have been made.

4.1 System Calibrations

The resistance of either the microbolometer or the bolometer in the power-density meter is a linear function of the power dissipated in it [1],

$$R = R_0 + \mathcal{R}P \tag{4.1}$$

where R and R_0 is the biased and non-biased resistance of the bolometer, $\mathcal{R}$ is the resistance responsivity (Ω/W) of the bolometer, and P is the power dissipated in the bolometer, being either DC power or RF power. Since Equation (4.1) can be expressed as

$$\frac{V}{I} = R_0 + \mathcal{R}(IV) \tag{4.2}$$

$\mathcal{R}$ can be found by measuring the DC I-V curve of the bolometer. These bolometers are all four-lead connected, with two leads for DC bias and two leads for the voltage measurement (shown in Figure 4.1), which essentially eliminates the effect of the series resistance; therefore, there is no need to take the series resistance into account in the calibration. Figure 4.2 shows a typical R-P plot for a one-step microbolometer on the membrane, along with linear fitting lines; the correlation coefficients for the fits are normally better than 0.999. The I-V curve for each bolometer is measured before and after the aperture-efficiency measurement to ensure the accuracy. The deviation of the resistance responsivity between the two measurements is usually smaller than 0.5 %. The resistance responsivity of the microbolometer is typically 2×10^4 Ω/W, while 150 Ω/W for the bolometer in the power-density meter.

Equation 4.1 can also be written as

$$R = R_0 + \mathcal{R}(P_{DC} + P_{RF}) \tag{4.3}$$

The resistance change ΔR_{RF} of the bolometer caused by an RF power is found when the changes of the voltage are measured with a constant DC current applied

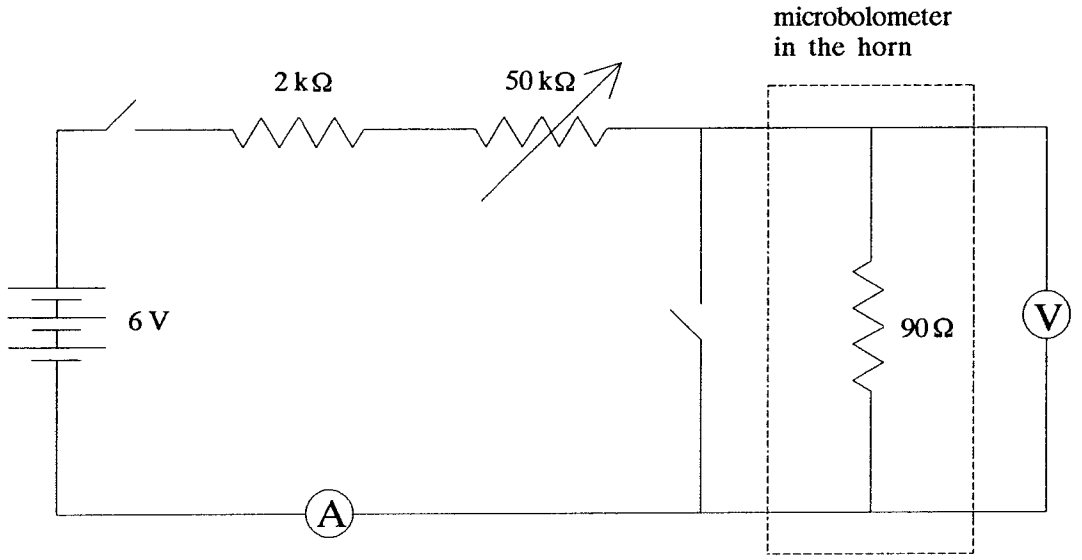

Figure 4.1 Circuit connections of the bolometer-responsivity measurements.

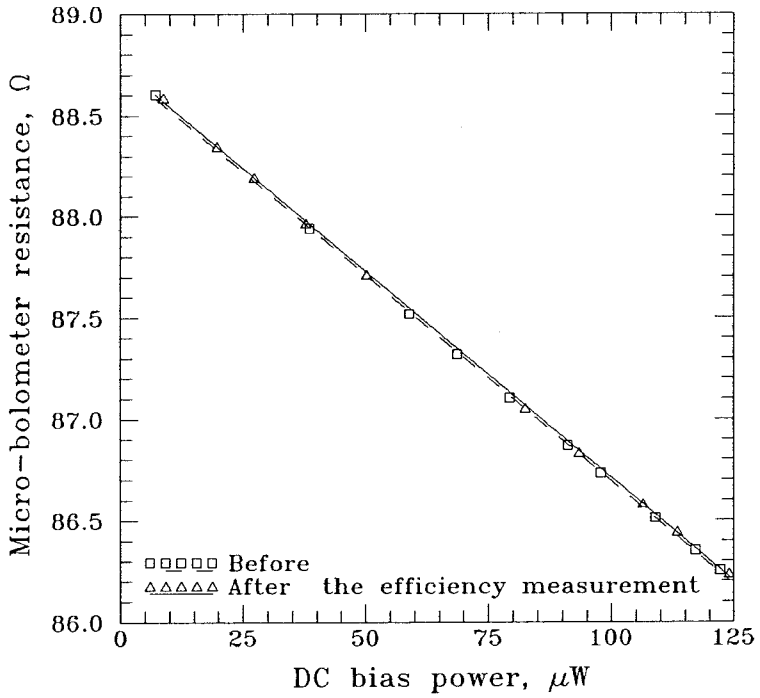

Figure 4.2 Measured resistance versus DC bias power for the microbolometer, before (dashed line) and after (solid line) the aperture-efficiency measurement.

to the bolometer,

$$\Delta R_{RF} = R - (R_0 + \mathcal{R} P_{DC}) \tag{4.4}$$

Then the P_{RF} is simply given by

$$P_{RF} = -\frac{\Delta R_{RF}}{\mathcal{R}} \tag{4.5}$$

All voltage and current measurements are made with Hewlett-Packard $6\frac{1}{2}$-digit multimeters. The time constant of the microbolometer is in the order of milliseconds; on the other hand, at least 5 minutes are needed before making a resistance measurement to allow for the long time constant of the large-area bolometer in the power-density meter. To obtain accurate, absolute power-density measurements from the power-density meter, edge effects and the effects of the biasing contacts and the voltage-sensing leads should be negligible. To check for these effects, several bolometers of different sizes were constructed. The measurements from the different bolometers agreed to within $\pm 2\%$. The results are shown in Figure 4.3 measured at 93 GHz.

The bolometer response of the power-density meter as a function of incident angle can be calculated by using the transmission-line model. When the sheet resistance is half the free-space impedance, the pattern is independent of the

Width, cm	Length, cm	Power density, $\mu W/cm^2$
2.0	2.0	575
2.0	1.5	565
2.0	1.0	564
1.5	2.0	582
1.0	2.0	569

Figure 4.3 Power densities measured with different bolometers at 93 GHz. The sample standard deviation is 1.2%.

polarization and is given by

$$P(\theta) = \frac{2\cos^2\theta}{(1+\cos\theta)^2} \tag{4.6}$$

where θ is the incident angle. The measurements agreed well with the theory, and there are no spikes near normal incidence [2]. Furthermore, since maximum absorptance of the power is obtained at normal incidence, the accuracy of the power-density meter is insensitive to small changes in the angle of incidence. At higher frequencies, the finite thickness of the mylar membrane will affect the absorptance of the bolometer film. The calculated correction factor indicates that the absorptance will decrease by 1.2 % from 0.5 at 1 THz when the bolometer film is in front of the mylar sheet. The reflective index is taken from [3]. This verifies that the effect of the mylar is negligible at 93 GHz. Alternatively, the thickness of the membrane could be reduced to avoid using the correction [4] for high frequencies. Considerations and tests have been done carefully for different sources of errors: resistance drift, edge effects, time constants, varying angles of incidence, and absorption in the styrofoam, and it is believed that the measurements are accurate to better than 5 % for incident power densities greater than $100\,\mu\mathrm{W/cm^2}$.

4.2 Aperture Efficiency Measurements

In the aperture efficiency measurements, the RF signal source is a 93-GHz klystron with an output power of 170 mW. The horn array is placed in the far field of the source (Figure 4.4), about 60 cm away, which is much farther than the far-field criterion of $2\mathrm{d}^2/\lambda$, where d is the larger cross section of the transmitting horn. In the neighborhood of the measurement setup are the millimeter-wave absorbers. Figure 4.5 shows the mounting and wire connections of the antenna array to the outside circuits. The microbolometer is biased by a DC current source at about 1 mA. By blocking and unblocking the incoming signal, the

changes in resistance of the microbolometer were measured. Then, the power-density meter is placed at the same location, and its changes in resistance are also measured. The aperture efficiency η of a horn can then be written as a simple formula,

$$\eta = \frac{A_m \mathcal{R}_m \Delta R_h}{A_h \mathcal{R}_h \Delta R_m} \tag{4.7}$$

where A_m is the area of the power-density meter, $\mathcal{R}_m$ is the corrected resistance responsivity of the meter, ΔR_h is the resistance change of the horn microbolometer, A_h is area of the horn, $\mathcal{R}_h$ is the responsivity of the horn microbolometer, and ΔR_m is the resistance change of the power-density meter. Alternatively, the power-density measurement can be related to the reading on the wave-guide power meter in Figure 4.4. This makes it unnecessary to calibrate the directional coupler, attenuator, and horn individually.

Figure 4.6 shows the measured efficiencies for different dipole probe lengths. Measurements were made first for membrane wafers without gold coating. After the membrane wafers were coated with gold, the efficiencies were measured again.

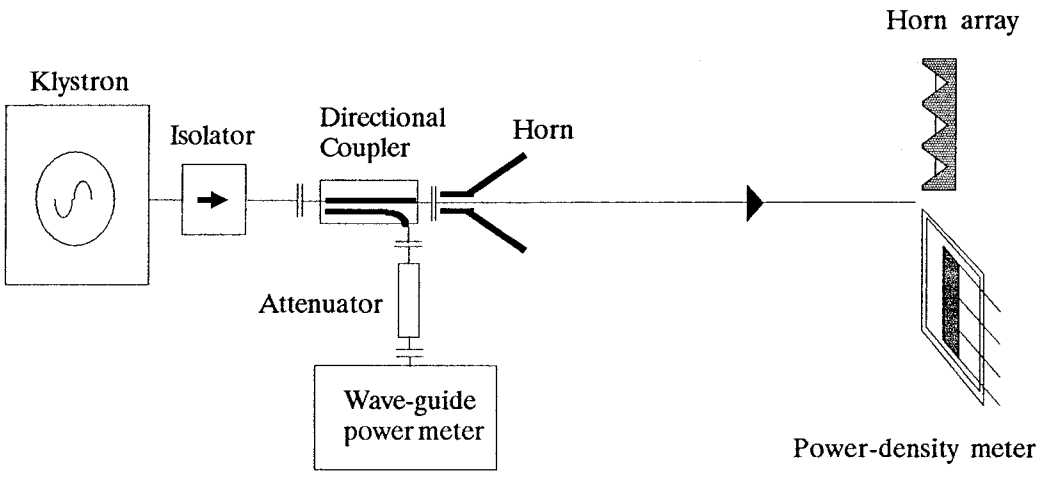

Figure 4.4 The setup of the aperture efficiency measurement.

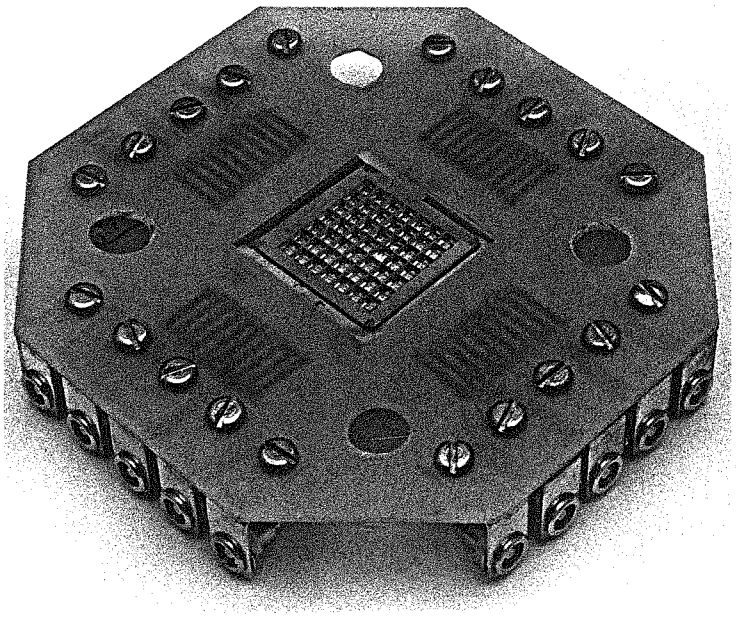

(a)

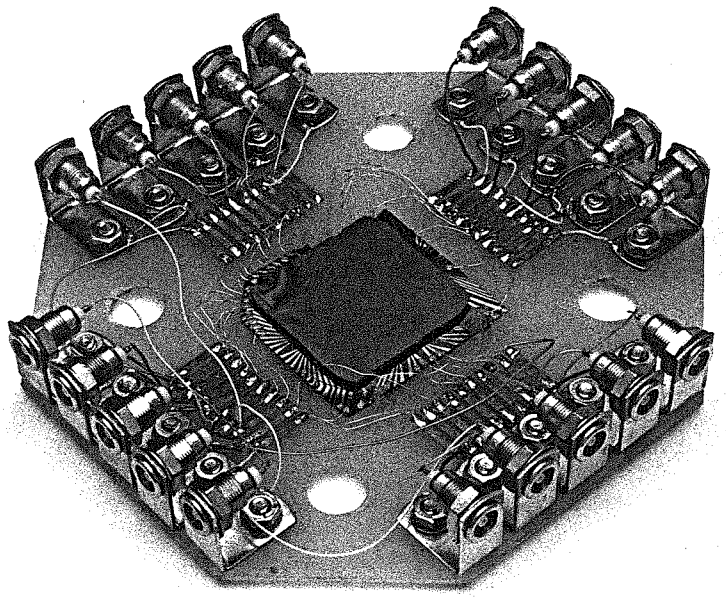

(b)

Figure 4.5 Photographs of the antenna array mounting and wire connections; front view (a) and back view (b).

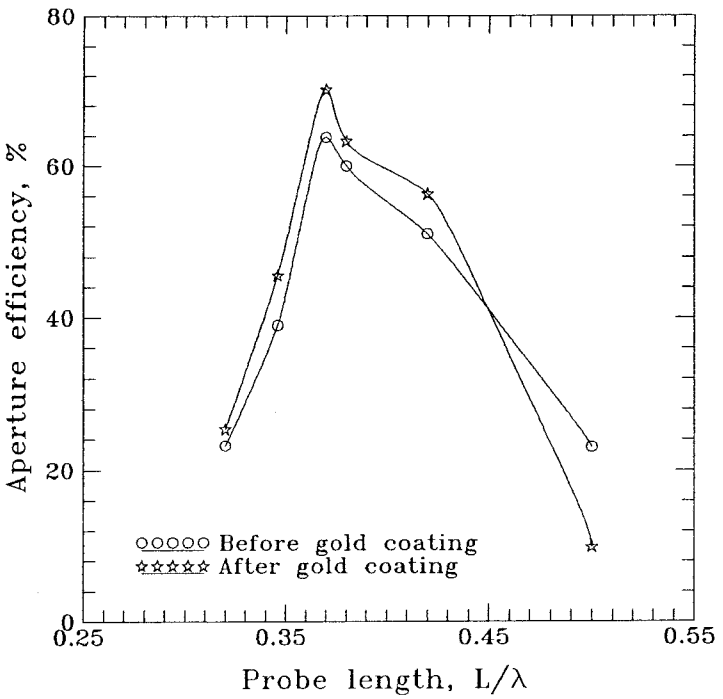

Figure 4.6 Measured aperture efficiencies at 93 GHz versus dipole probe length. The efficiencies were measured before (labeled with squares) and after (labeled with stars) coating the membrane-wafer sidewalls with evaporated gold.

The efficiency reaches its maximum value, 72 %, for a length of 0.37 λ, compared with 44 % obtained before [5]. For all but the longest probe, gold-coating the sidewalls of the membrane wafer improves the efficiency, with a typical improvement of 6 %. Figure 4.7 shows the estimated loss breakdown. The total calculated loss is 1.2 dB, compared with the measured value, 1.4 dB. There is still some mismatch loss (0.4 dB) because the bolometer resistance in the meas-urements is about 90 Ω, compared with the resonant antenna resistance of 50 Ω that was measured on the microwave model. A plot of the efficiency versus the frequencies ranged from 77 GHz to 109 GHz was also made for various dipole-probe lengths, and this is shown in Figure 4.8. Probes with lengths in the range from 0.37 to 0.40 λ gave efficiencies better than 60%. The 3-dB bandwidths are of the order

Loss component	loss, dB
Taper loss	0.5
Cross-polarization loss	0.2
Mismatch loss	0.4
Horn-to-horn coupling loss	0.1
Total calculated loss	1.2
Measured loss	1.4

Figure 4.7 The summary of calculated and measured losses.

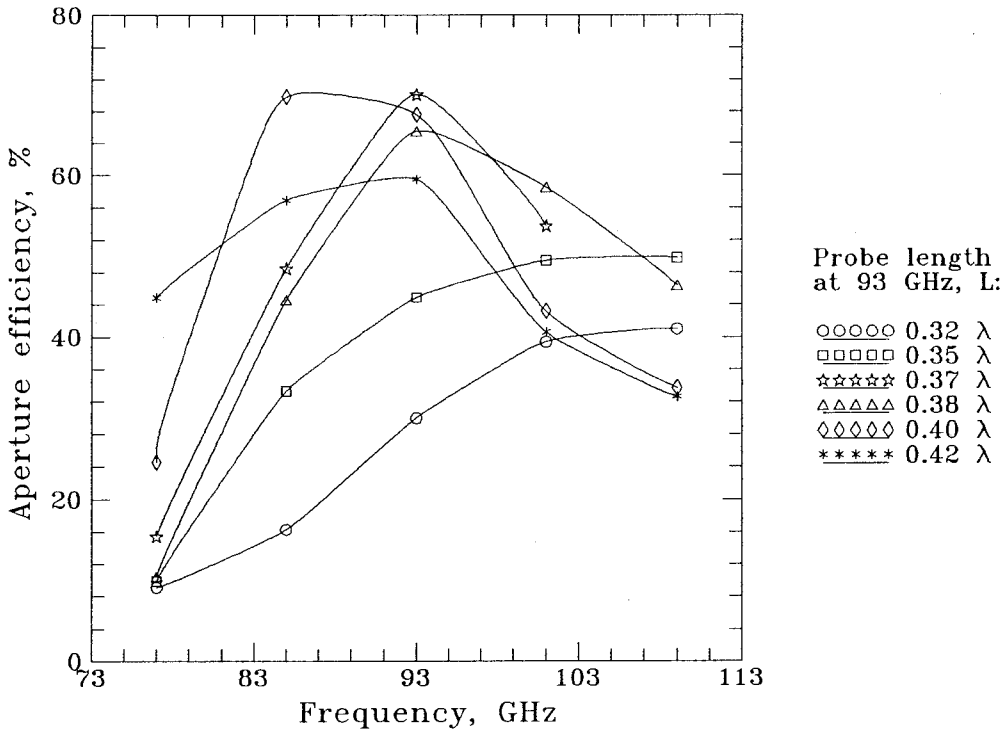

Figure 4.8 Measured aperture efficiencies at 93 GHz versus frequency for different dipole-probe lengths.

of 10 GHz.

4.3 System Efficiency Measurements

The Measurements of the system coupling efficiency were made with a lens in front of the array (Figure 4.9). The system coupling efficiency is the ratio of the detected power to the power incident on the lens. In the measurement, various stops were used to change the half angle subtended by a 100-mm diameter lens with an f-number of 0.75. The highest system coupling efficiency with a lens is 36% for an f-number of 0.75 (Figure 4.10). The losses from reflection and absorption in the lens were estimated to be 28 %, so that it should be possible to achieve a coupling efficiency of 50% in an f-0.75 system with reflecting optics.

In conclusion, aperture efficiency of the integrated-circuit horn antennas has been improved up to 72 % by optimizing the length of the dipole probes and by coating the entire horn sidewalls with gold. The system coupling efficiency is 36% for an f-number of 0.75. The resonant resistance of the dipole probe was found to be 50 Ω at the dipole probe length of about 0.20 λ. Meanwhile, a new thin-

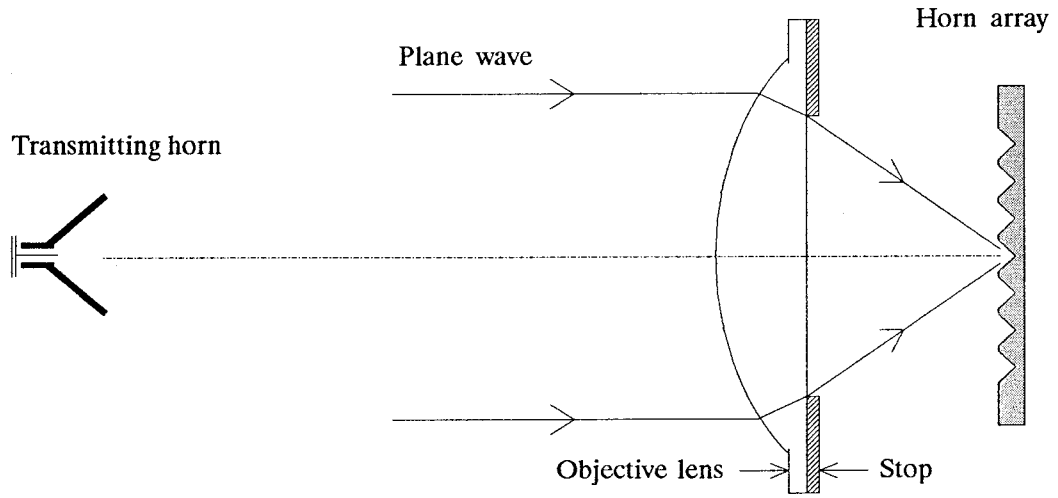

Figure 4.9 A system of coupling efficiency measurements. Different f-numbers were obtained by changing stops behind the lens.

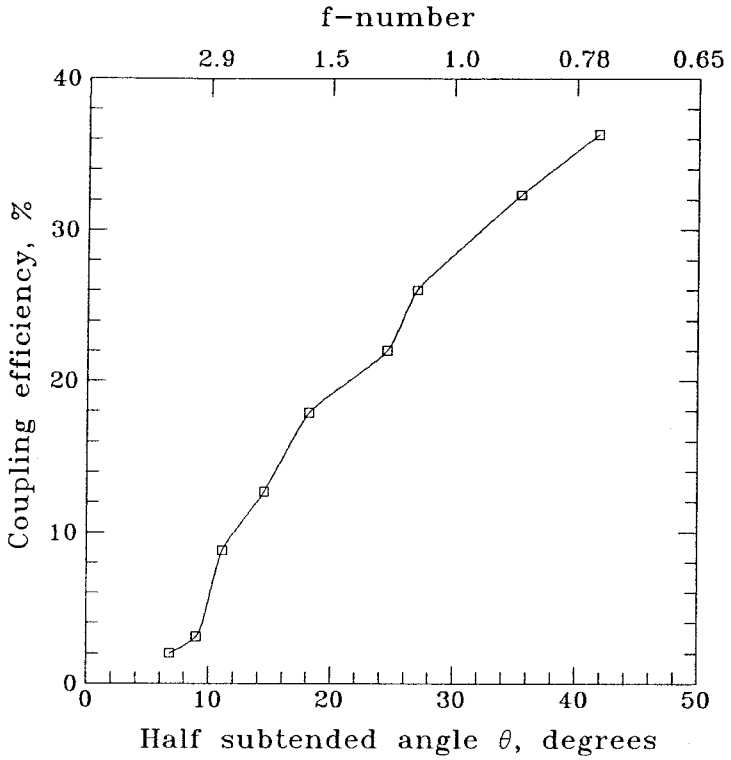

Figure 4.10 The measured system coupling efficiencies. The horizontal axis is the half angle subtended by the lens, which is varied by changing stops behind the lens. This measurement includes the loss from reflection and absorption in the lens.

film, large-area- bolometer power-density meter was developed for measuring millimeter-wave power density with accuracies better than 5 %. These horn antennas are now efficient enough to be considered for practical applications, such as remote sensing, plasma diagnostics, and radio astronomy.

4.4 Test of Beam-Lead Diodes in the Horn Array

In the aperture efficiency measurements described above and other previous measurements including pattern measurements [5], the detector used in the antenna array on the dipole probes is always a bismuth, thermal microbolometer, which is a very useful detector considering its simple fabrication techniques plus its easy and accurate calibration. However, in the application of imaging

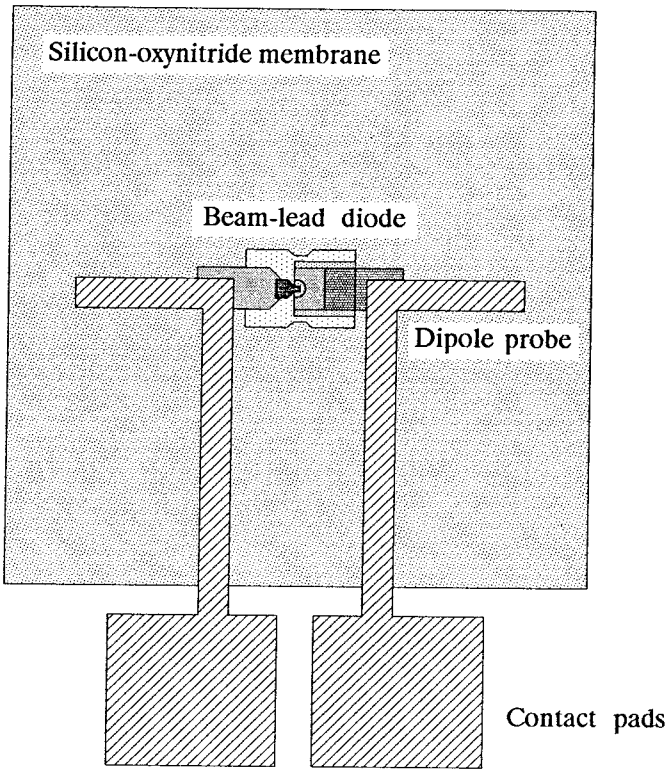

Figure 4.11 A beam-lead, Schottky diode silver-paint glued on the membrane in the center of the dipole probe. The dimension of the diode is about $900 \times 300\,\mu m^2$.

a fast-moving object, the microbolometer with a millisecond response time becomes inadequate; thus faster detectors are in demand, for example, Schottky diodes or SIS detectors. Additionally, in a quasi-optical, antenna-mixer array, a non-linear mixing element other than a thermal bolometer is also an essential requirement. Hence, diodes or other semiconductor detectors need to be introduced into the horn antenna array, either monolithically or in a hybrid manner. As a preliminary test, a few beam-lead diodes were mounted on the membrane in the center of the dipole probe (Figure 4.11), using a gold-filled epoxy, which was cured at 125°C for 2.0 hours. This antenna array with diodes in it has successfully passed the standard environmental test [6], which includes 8 temperature cycles between −30.0 to +65.0°C, 48 hours of continuous burn-in at 62°C and

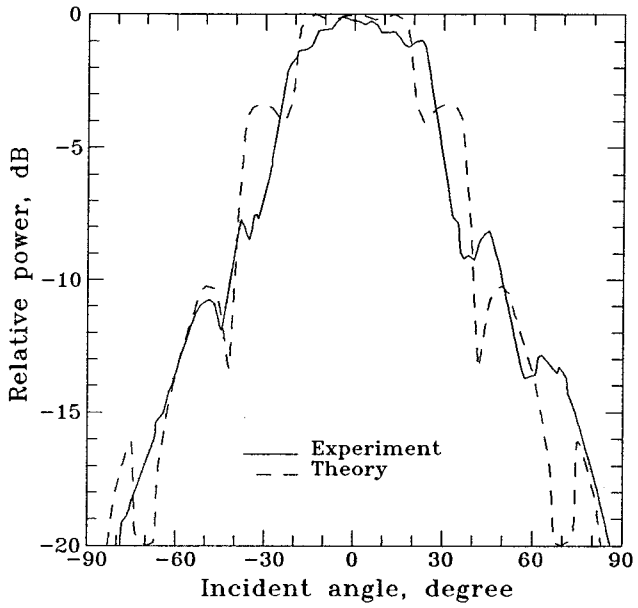

(a)

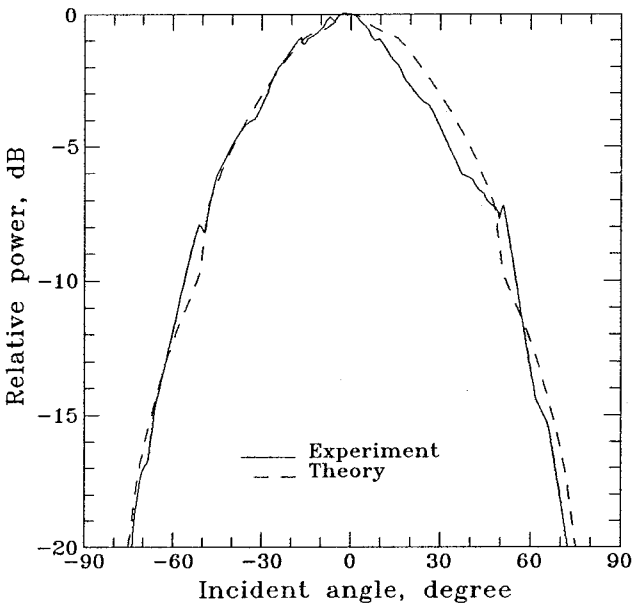

(b)

Figure 4.12 E-plane(a) and H-plane(b) patterns of the horn antenna array using beam-lead diodes as detectors; measured results in solid line and theory in dashed line.

Plane of scanning	Frequency (GHz)	Beamwidth (degree) 3 dB	10 dB	20 dB	Cross-Pol. Level (dB)
E-plane	75	38.0	132.7	—	–15
E-plane	85	37.3	106.6	165.2	–20
E-plane	95	47.8	89.4	165.7	–24
E-plane	105	46.8	80.2	144.4	–18
H-plane	75	74.3	125.3	155.3	–15
H-plane	85	50.6	109.2	153.3	–18
H-plane	95	49.4	109.3	146.5	–17
H-plane	105	45.8	101.0	142.5	–22
Diagonal	75	44.8	113.7	169.9	–13
Diagonal	85	41.0	91.6	169.9	–13
Diagonal	95	42.7	94.5	162.2	–17
Diagonal	105	54.7	85.1	145.1	–15

Figure 4.13 Summary of the pattern beamwidths and cross-polarization levels of the beam-lead diode, horn-antenna array; cross-polarization levels shown in the last column in the table.

3-axis vibration of $0.20g^2/\text{Hz}$, each axis at 2.0 minutes duration. The I-V curve of the diode was verified before and throughout the entire environmental test. These encouraging test results indicate that the horn antenna array with diodes as detectors can be constructed in an airborne imaging system or on a satellite.

Antenna patterns were also measured for the antenna array using the beam-lead diodes as detector elements [7]. Patterns were measured at frequencies of 75, 85, 95 and 105 GHz in the E-, H- and diagonal planes. Particularly, the E-plane and H-plane patterns measured at 95 GHz are presented in Figure 4.12, which shows good agreement with the theoretical patterns. In the figure, the H-plane pattern is smooth and does not show sidelobes, while the E-plane pattern shows

sidelobes as predicted by the theory. As a summary, Figure 4.13 lists the pattern beamwidths and cross-polarization levels of the beam-lead-diode horn-antenna array.

References

[1] D.P. Neikirk, Wayne W. Lam, D.B. Rutledge, "Far-Infrared Microbolometer Detectors," *International Journal of Infrared and Millimeter Waves*, Vol. 5, No. 3, 1984.

[2] D. B. Rutledge and S. E. Schwarz, "Planar Multimode Detector Arrays for Infrared and Millimeter-Wave Applications," *IEEE J. of Quantum Elec.*, Vol. QE-17, No. 3, March 1981.

[3] *American Institute of Physics Handbook*, 3rd Edition, McGraw-Hill Book Company, New York, 1972.

[4] C. C. Ling, G. M. Rebeiz, "A Wideband Monolithic Submillimeter-Wave Quasi-Optical Power Meter," *IEEE MTT-S International Microwave Symposium*, May, 1990, Dallas, Texas.

[5] G. Rebeiz, D. Kasilingam, Y. Guo, P. Stimson, D. Rutledge, "Monolithic Millimeter-Wave Two-Dimensional Horn Imaging Arrays," *IEEE Transactions on Antennas and Propagation*, Vol. 38, pp. 1473–1482, September, 1990.

[6] The environmental tests were done at Aerojet ElectroSystems, courtesy of Robert W. Haas.

[7] The pattern measurements were done at Aerojet ElectroSystems, courtesy of Dennis H. Brest.

Chapter 5

Back-to-Back Horn-Antenna-Mixer Array Designs

In millimeter-wave systems, because of their higher frequencies and complexities compared with microwave systems, it is inevitable to simplify components and to combine functions whenever possible. Traditionally, mixers are made of mixing elements and wave-guide circuits, which are normally machined. At shorter wavelengths, the wave-guide circuits become much smaller, making them very expensive to build. However, quasi-optical components provide a solution to this problem. The back-to-back quasi-optical horn-antenna-mixer arrays, presented in this thesis, combine monolithically the function of antennas and mixer circuits into a single array. These types of circuits potentially can be mass produced by standard, integrated-circuit technology. Moreover, the integration of the antenna and the mixer eliminates the need for RF and LO circuit-fashion connections. Such construction offers the potential of smaller size, light weight, ruggedness and reduced cost, as compared to conventional methods. The applications of this monolithic technique include imaging systems, radars, plasma diagnostics and satellite communications.

5.1 Horn Structure and Circuit Designs

A mixer, in principle, can be thought of as an ideal multiplier [1], illustrated in Figure 5.1, which shows an ideal analog multiplier with two sinusoids applied to it. The signal, with a carrier frequency ω_S and modulated by the information-bearing function $A(t)$, is applied to the RF port. The other one applied to the LO port is an unmodulated sinusoid with a frequency of ω_P. Through some simple trigonometry, the output is found to consist of modulated components at the sum and difference frequencies. The sum frequency can be rejected by the IF filter, leaving only the difference frequency. In a real mixer, the ideal multiplier is replaced by non-linear devices, such as mixer-diodes or transistors. However, these non-linear devices will not perform simple multiplication; they generate many LO harmonics and mixing products other than the desired one. Consequently, the desired output frequency component must be filtered out from the resulting frequencies.

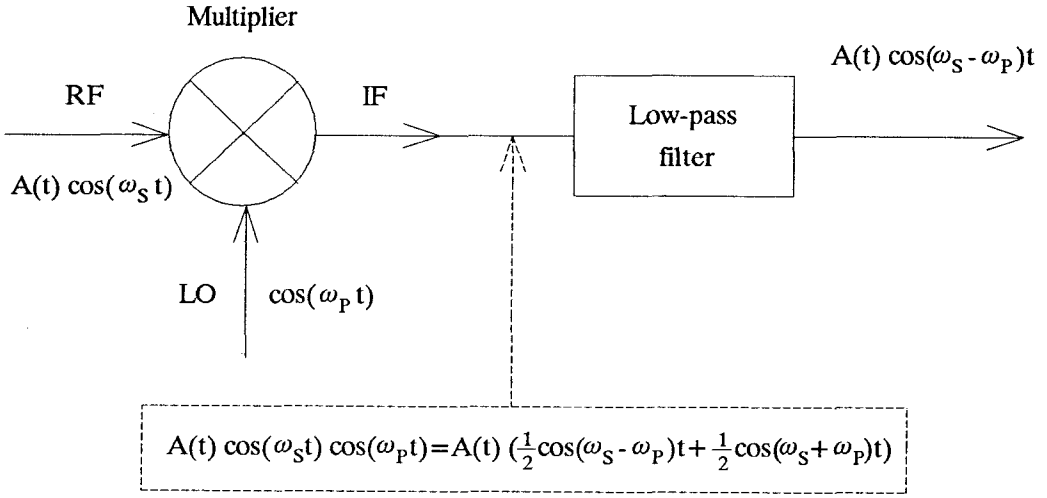

Figure 5.1 A mixer fundamentally acts as a multiplier; the difference frequency IF comes from the multiplication of the sinusoids.

In designing the quasi-optical antenna-mixer array, the first thing to be considered is how to construct the RF and LO ports to couple RF and LO signals into such an array, i.e., the construction of horn structures. One of the simplest designs one can think of is to put a beam diplexer in front of the single-side horn array so that the signal RF and LO can be combined before being fed into the horn array (as shown in Figure 1.2, Chapter 1). Although this is a simple and quick way based on existing fabrication techniques, it suffers from the disadvantage of a 3 dB loss in both the signal RF and LO power even before mixing, because both beams pass through the beam diplexer. This 3 dB loss can be eliminated if RF and LO are fed in from each side of the horn array. As Figure 2.1 in Chapter 2 shows, that there is plenty of space between the single-side horns, which can be used to make another set of horns for LO reception. These horn arrays with two sets of horns facing back to each other are called back-to-back horn antenna arrays.

One of the horn structure designs is a so-called coaxial back-to-back array [2], which consists of a set of coaxial forward- and backward-looking horns sharing the same membrane (Figure 5.2). The membrane and dipole probes are placed where the horn width is approximately $\lambda/2$, the same as the single-side horn array, but there is no closed pyramid forming the horn apex. This would permit a very simple mixer design, as transmission lines would not be needed for the RF and LO. One antenna probe on the same membrane could be designed for both signal reception from the front and LO reception from the back. However, calculations indicate that it is difficult to avoid significant coupling of the two waves traveling in the opposite direction inside the horn, which would result in a low aperture efficiency. To solve this problem, an inductive grid reflector could be used, which consists of lines of metal strips on another membrane placed behind the horn antenna to prevent the tunnelling. In such a design, two additional membranes are required, one for the signal RF and one for the LO. The signals

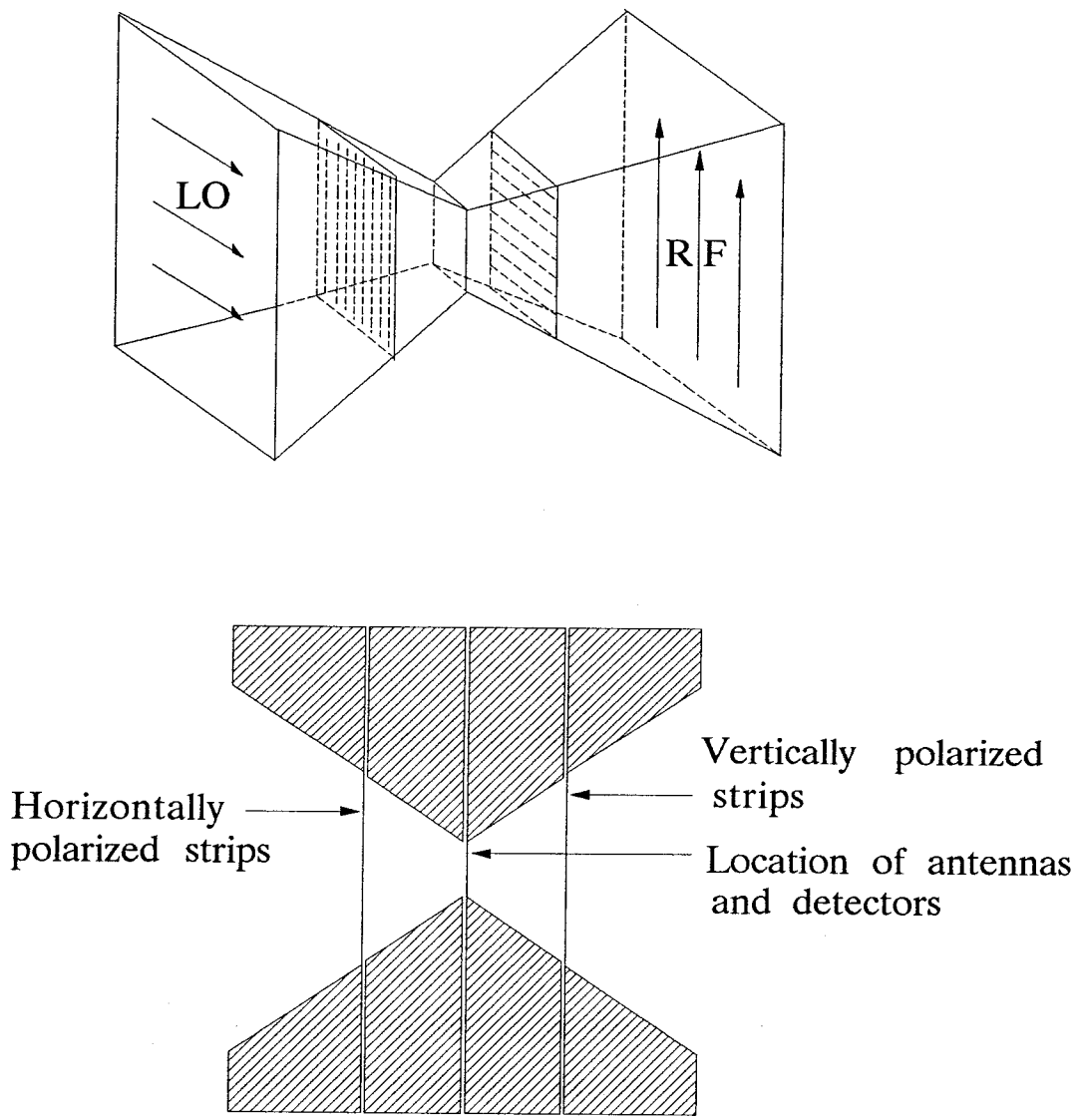

Figure 5.2 Coaxial back-to-back horn antenna array; the central membrane contains antenna probes and the other two membranes with metal strips act as reflectors; one of them will let the RF in but reflect the LO, and the other one will do the opposite.

RF and LO would use opposite polarizations to allow passage through the first grid and to ensure reflection from the next. For the antenna probes, polarization-duplexed probe elements can been used [3]. The signal would be received in the horizontal polarization by a horizontal dipole and the LO applied with vertical

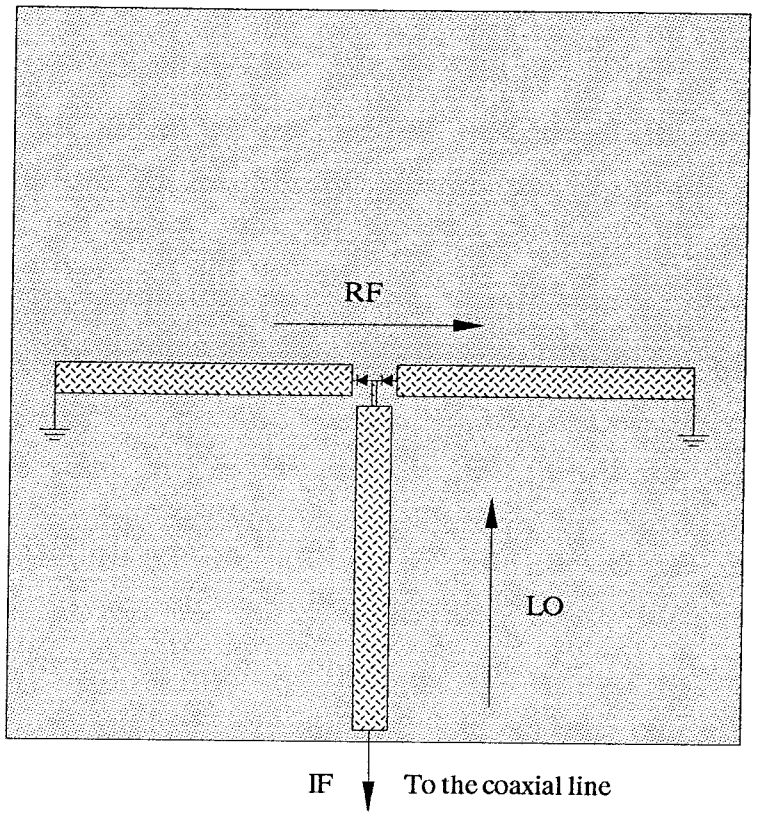

Figure 5.3 Mixer circuit design for coaxial back-to-back horn array; signal RF and LO are cross-polarized; IF is led out from the central tap.

polarization and received by a vertical monopole. This three-membrane-wafer design has the advantage that signal RF and LO transmission lines would not be required. Fabrication would be a straightforward extension of single-side horn array-making procedures; the structure is modular and the reflector membranes and grids would not have to be re-fabricated for each new device. The disadvantage is that this configuration is a departure from the standard horn geometry whose efficiency has been optimized. Nevertheless, one of the mixer designs for this array configuration is given in Figure 5.3; it is a balanced fundamentally pumped mixer consisting of two diodes in series with a center tap for the IF lead.

The horn configuration that has been designed for the antenna-mixer array is one called displaced, back-to-back horn array. This design, shown in Figure 5.4, consists of a set of forward- and backward-looking horns sharing the same membrane wafer. The front side is used to receive the signal RF, and the back side is used for the LO. Both RF and LO are picked up by antenna probes on the silicon-oxynitride membrane inside the horns and then fed down to monolithic transmission lines on the membrane surface, to be combined in a mixer located on the membrane in the horns. The advantages of this configuration are in avoiding the 3 dB loss of a beam diplexer, and keeping the original horn geometry with optimal aperture efficiency.

For a fundamentally pumped mixer, the frequencies of RF and LO have only a small difference, which means the sizes of the RF and LO horn openings can be made about the same, about one wavelength. The horns will look the same from either the RF side or the LO side as shown in Figure 5.5, except that LO horns have a small section of protrusion on the sidewalls as shown in Figure 5.4, and that the antenna probes used for the signal RF could be different from those for the LO. The protrusion caused by the membrane wafer W3 results in the unsmoothed sidewalls in the LO horns. The reason for this is that the etchant, EDP, etches the (100) silicon wafer, resulting in convergent, pyramidal-shaped sidewalls; if the LO horn sidewall is to be made smooth, a portion of the silicon underneath the membrane would need to be etched off, which is difficult to do, but possible. To avoid such a difficulty, the membrane wafer is etched from only one side, and the unsmoothed LO sidewall is considered to be tolerable, because the LO power, in most cases, can be increased to overcome the effect of such imperfect horns. Figure 5.6 shows the antenna probe design for the RF and LO horns of a fundamentally pumped antenna-mixer array, selected from several possible designs. It is a single balanced mixer, which is quite desirable, because the AM noise contained in the LO signal does not in principle appear in the IF

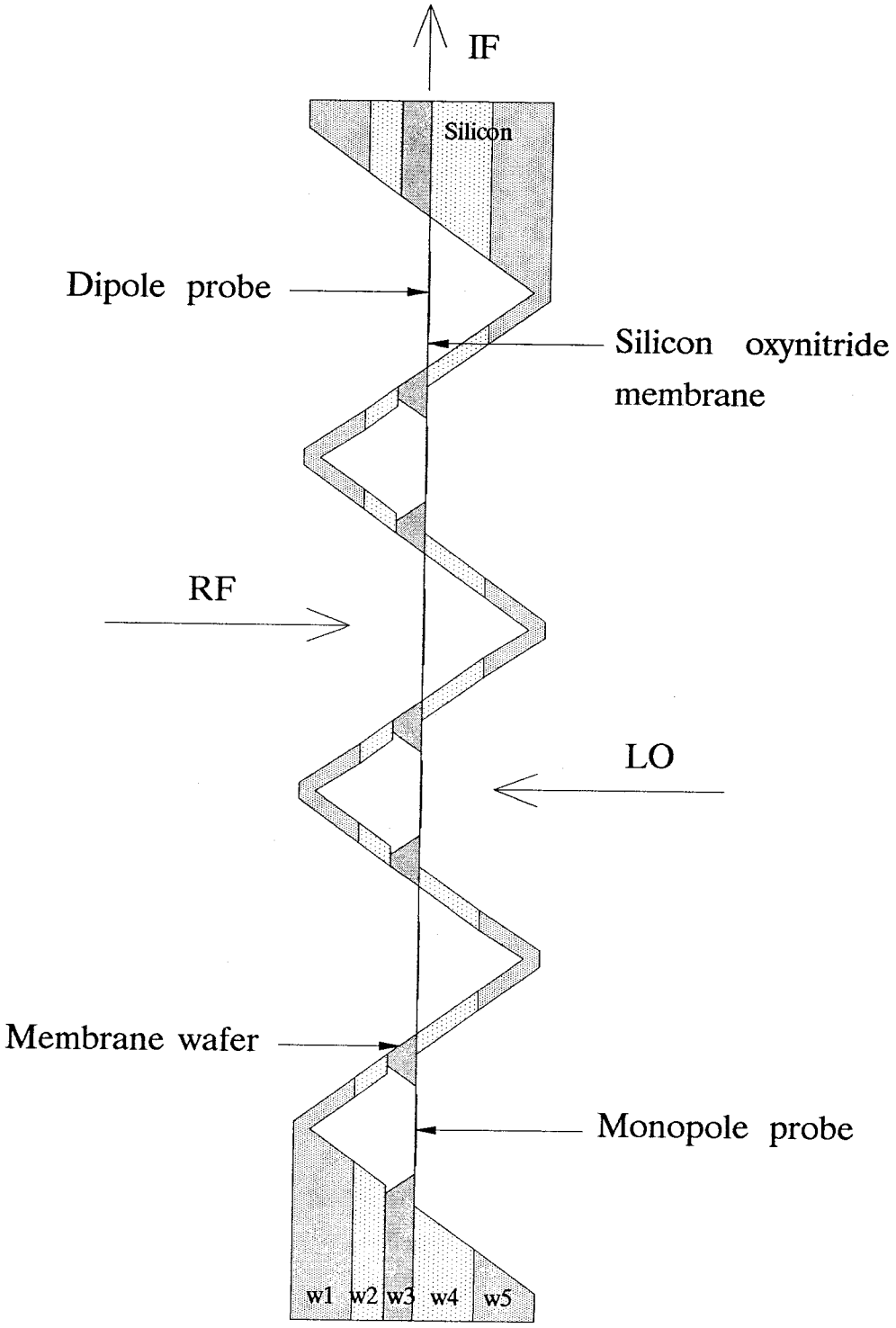

Figure 5.4 The displaced back-to-back horn-antenna array design consists of a set of forward- and backward-looking horns sharing the same membrane wafer.

output if the diode pair being used ideally matched to each other [4]. The mixer circuit consists of a folded-dipole RF probe driving the mixer diodes in series. If each diode has a resistance of 100 Ω, then it would require the folded dipole to have a resonant resistance of 200 Ω, which is fairly easy to achieve for these kinds of probes. A split-folded monopole is used as the LO probe driving the diodes in

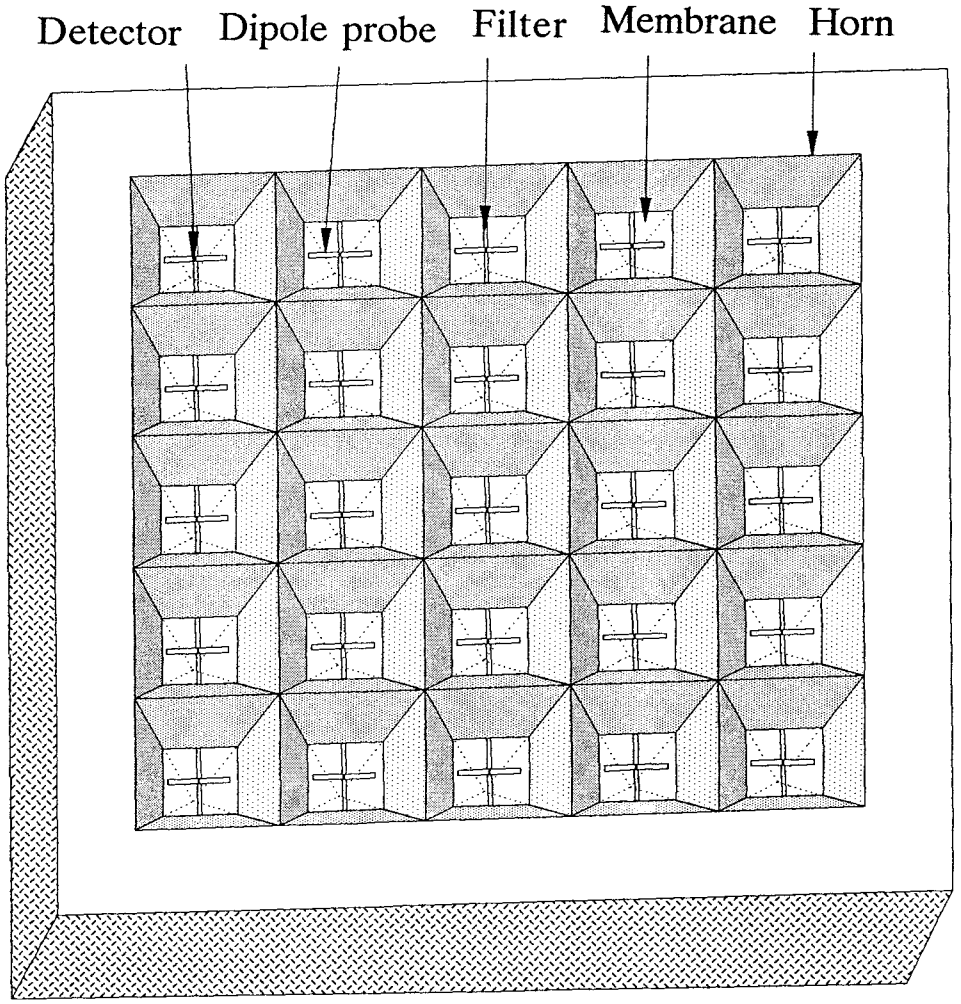

Figure 5.5 The displaced, back-to-back, horn-antenna-mixer array looking from the RF side is the same as looking from the LO side, except that LO horns have a small section of protrusion on the sidewalls as shown in Figure 5.4.

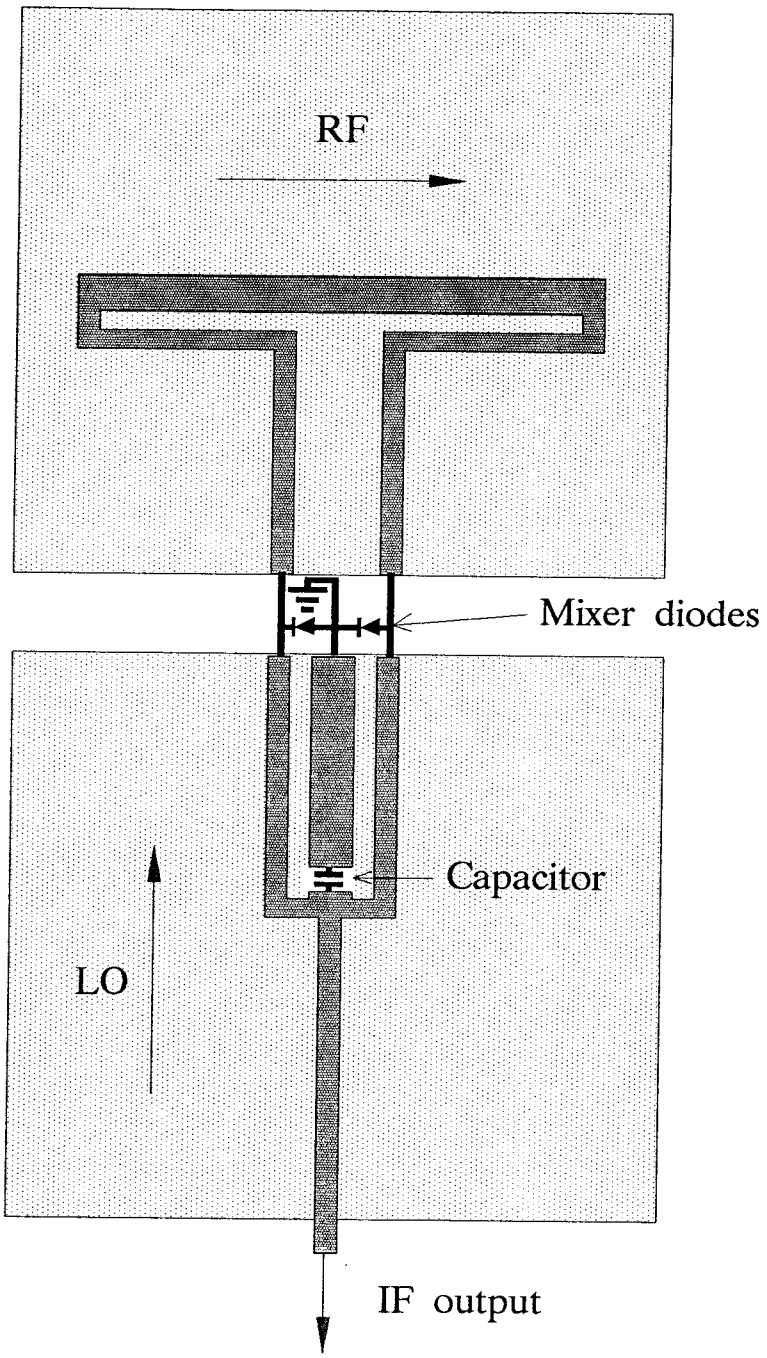

Figure 5.6 The mixer circuit design for the displaced, back-to-back, horn antenna array; a folded dipole is used for the RF signal and a split-folded monopole for the LO; the IF signal is led out through a long strip in the center of the LO membrane.

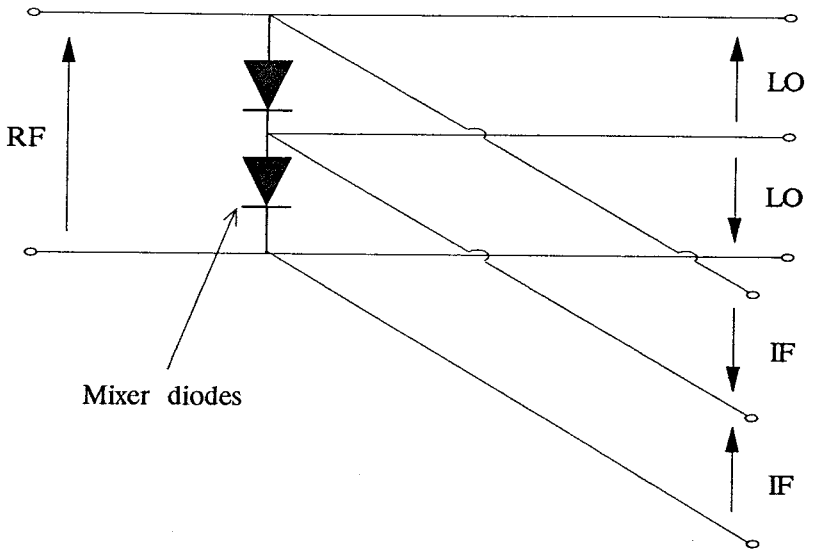

Figure 5.7 An equivalent circuit of the mixer design for the displaced back-to-back horn antenna array.

parallel and leading the IF out through the long split probe across the LO horn membrane. Since RF and LO are fed in from the opposite side of the array and are cross-polarized, this will significantly reduce their interference before mixing. The main advantage of the mixer circuit design is the ability to remove the IF signal without disturbing the balance of the RF and LO probes; furthermore, it removes the need for low-pass filters in the IF signal path. Figure 5.7 shows an equivalent circuit of such a mixer circuit design.

5.2 Subharmonically Pumped Mixer Designs

In millimeter-wave systems, as the operation frequency is increased, a direct supply of fundamental LO becomes increasingly more inconvenient, more difficult and more costly. A subharmonically pumped mixer provides a suitable solution. Such a mixer usually shows a poorer conversion loss than its fundamental counterpart. However, certain circuit designs can enhance its efficiency; for example, a back-to-back pair of diodes can be made to conduct twice per LO

cycle, and thus can function nearly as well as a conventional mixer with twice the LO frequency [5]. Since the RF and LO frequencies differ by approximately a factor of two, the filters to separate RF and LO are much easier to realize. Moreover, the subharmonically-pumped balanced mixer also rejects spurious responses associated with the odd harmonics of the LO.

For the reasons stated above plus the availability of the mixer-diode pairs working at 100 GHz, a new subharmonically pumped mixer has been developed, in which a pair of millimeter-wave, beam-lead mixer diodes is to be introduced in the horn antenna array. The mixer-diode pairs are available commercially, consisting of two diodes fabricated simultaneously and connected in antiparallel.

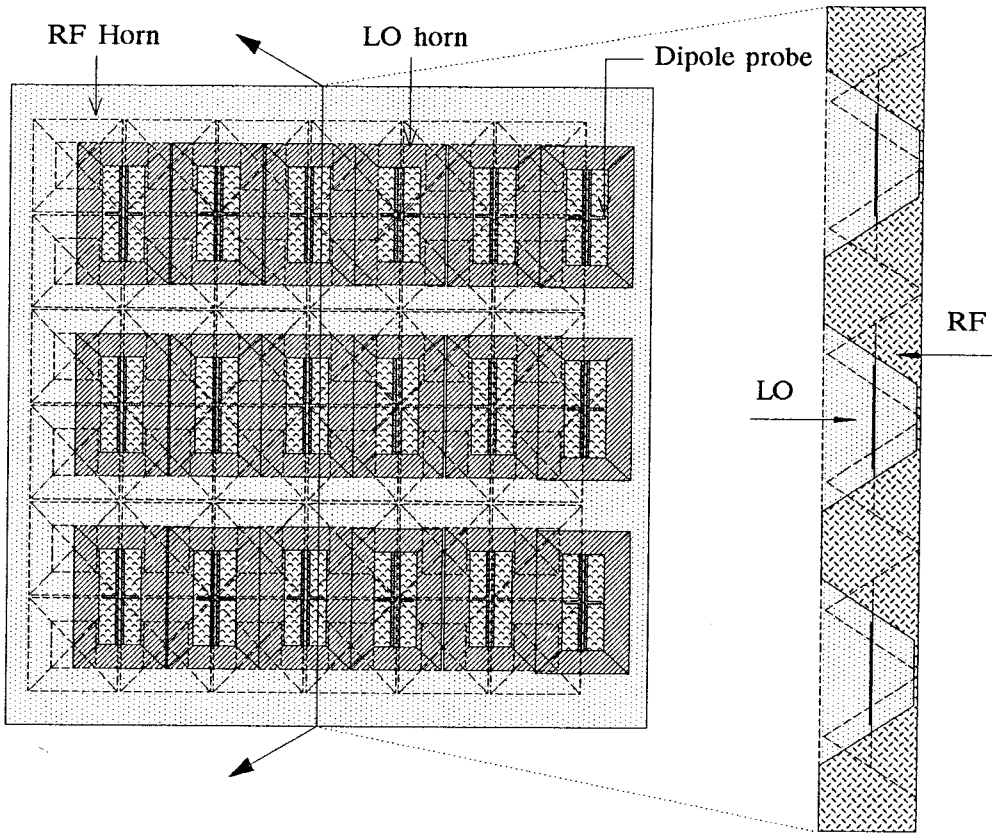

Figure 5.8 View of the horn structure of a subharmonically pumped mixer design, one LO horn corresponding to two RF horns.

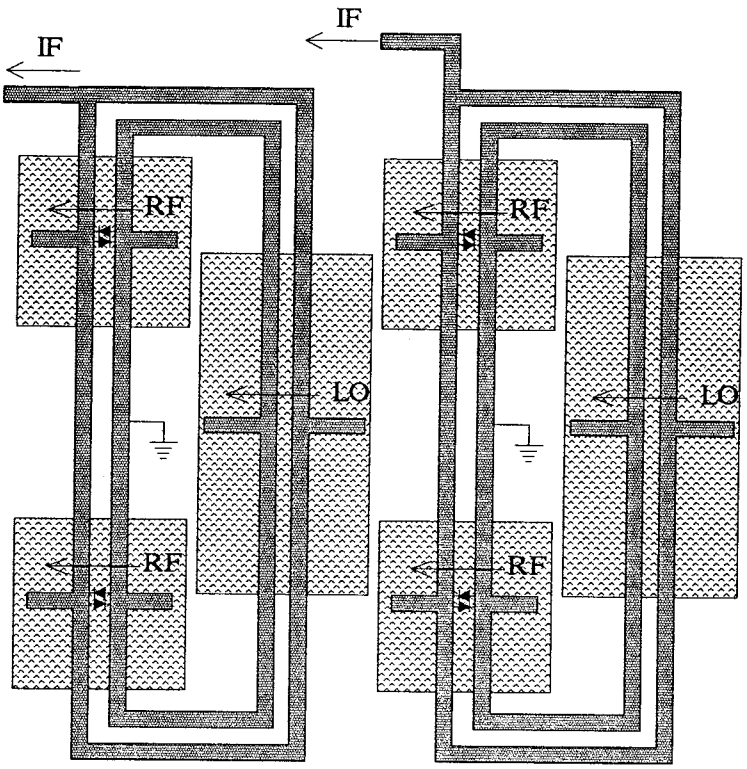

Figure 5.9 The mixer circuit design of the a subharmonically-pumped mixer design with one LO horn corresponding to two RF horns.

For the horn configuration, the so-called "displaced, back-to-back horn antenna array" is used. Now, since the size of the LO horns should be twice that of the RF horns, there is not enough room to put so many LO horns such that each RF horn can have a corresponding LO horn. In order to solve this problem, every two or every four RF horns will be provided with one LO horn, which is made of a rectangular horn instead of a square-opening horn. Since the cutoff frequency is determined by the dimension of the longer side of the rectangle, the dipole probes need to be put perpendicular to the longer side, making the dipole probes much shorter than a half wavelength, resulting in a capacitive characteristic impedance. This effect needs to be compensated for. Figure 5.8

shows a horn structure with every two RF horns corresponding to one LO horn, and a possible mixer circuit design is present in Figure 5.9. This configuration is simple and easy to build. But the shortcoming of the design is that it does not keep the symmetry between RF and LO horns, and the IF signal is difficult to take out.

In modifying the horn-structure design described above, every four RF horns are provided with one LO horn, which is still kept as a rectangular-shaped horn. By using the sub-array concept, every four RF horns can be taken as a sub-array; the four RF horns, together with one LO horn, form a unit cell. This design will keep the best symmetry, and the beam patterns of the sub-array will be improved by a factor of 4 compared with that of the single RF horn. Since the size of the LO horns should be twice that of the RF horns, half of the area on the LO side in each unit cell would be left unused. This would cause strong reflection from the flat surface, namely, a 3 dB reflection loss. In order to eliminate this 3 dB reflection loss, a structure is designed to be placed on the top of the LO horns. The structure has a long trough on each row of the LO horns and will fill up the space between the LO horns to converge the incoming power into the LO horns. Figure 5.10 and Figure 5.11 show the horn-antenna-mixer array with 4×4 LO horns looking from the LO side and 8×8 RF horns looking from the RF side. The mixer circuit design is shown in Figure 12. Every monopole from each of the four RF horns will couple the RF signal down to the LO horn through a coplanar-strip transmission line. A dipole probe is employed to receive the LO. The beam-lead diodes are located in the center of the LO membrane, and the IF is led out from the ends of the LO horn. The dipole probe is loaded on the ends near the sidewalls with a short stub, which, as a result, could compensate for the capacitive characteristic impedance of the short dipole probe.

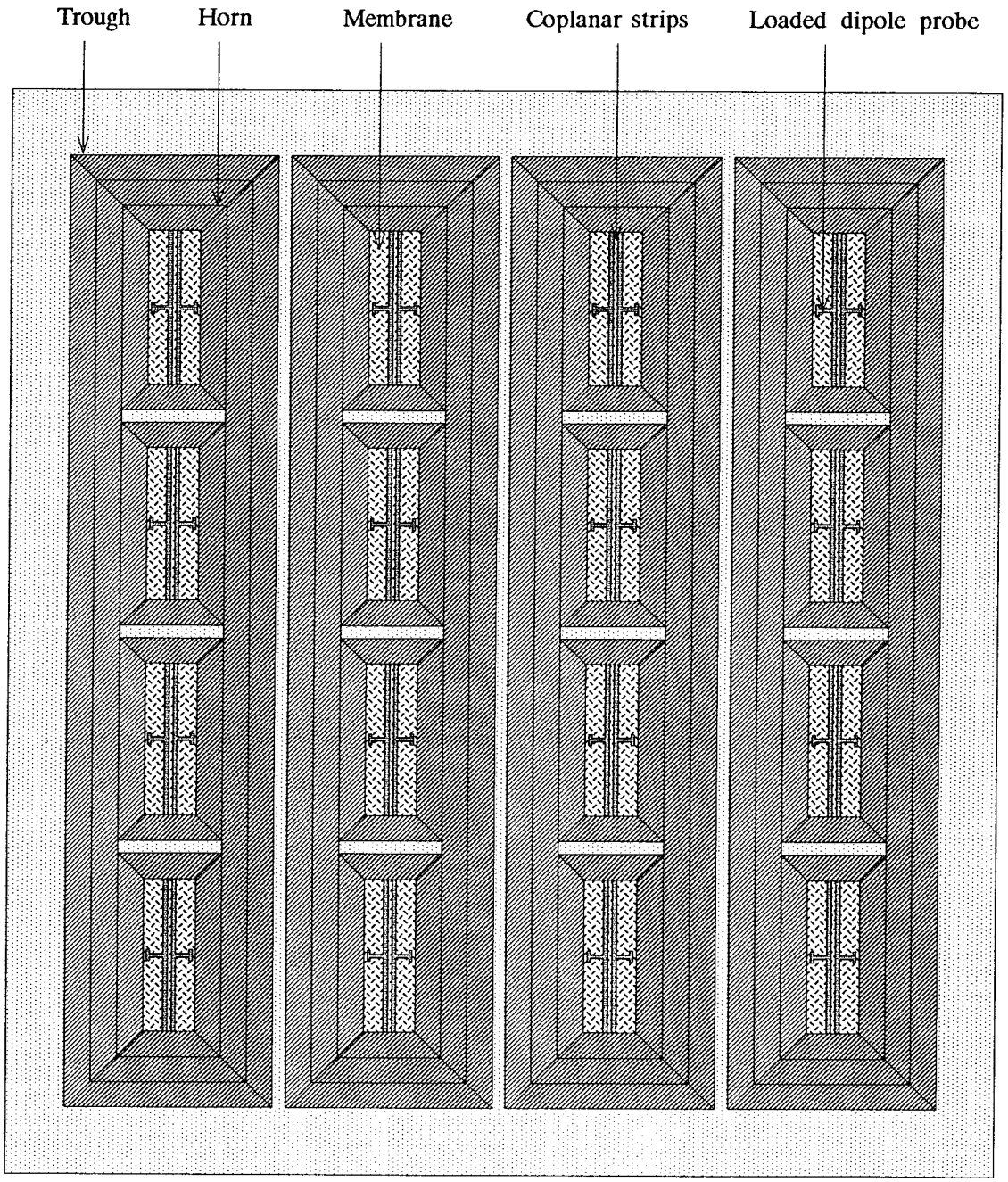

Figure 5.10 View of the LO horn structure of the subharmonically pumped mixer design with one LO horn corresponding to four RF horns; the trough made of two silicon wafers is put on the top of the horns to eliminate the strong reflection from the flat surface.

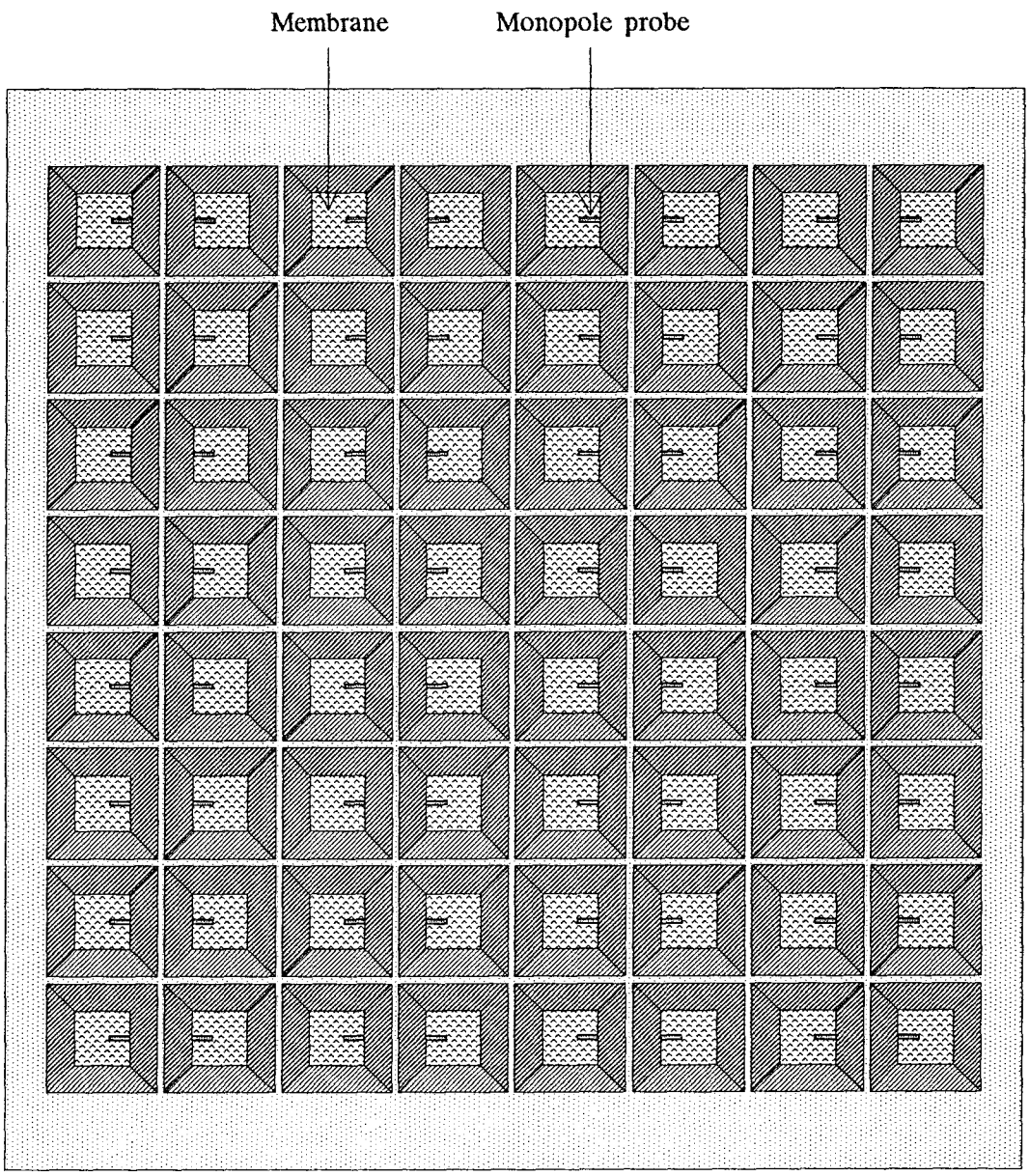

Figure 5.11 View of the RF horns of the subharmonically pumped mixer design; monopoles are used for the RF reception.

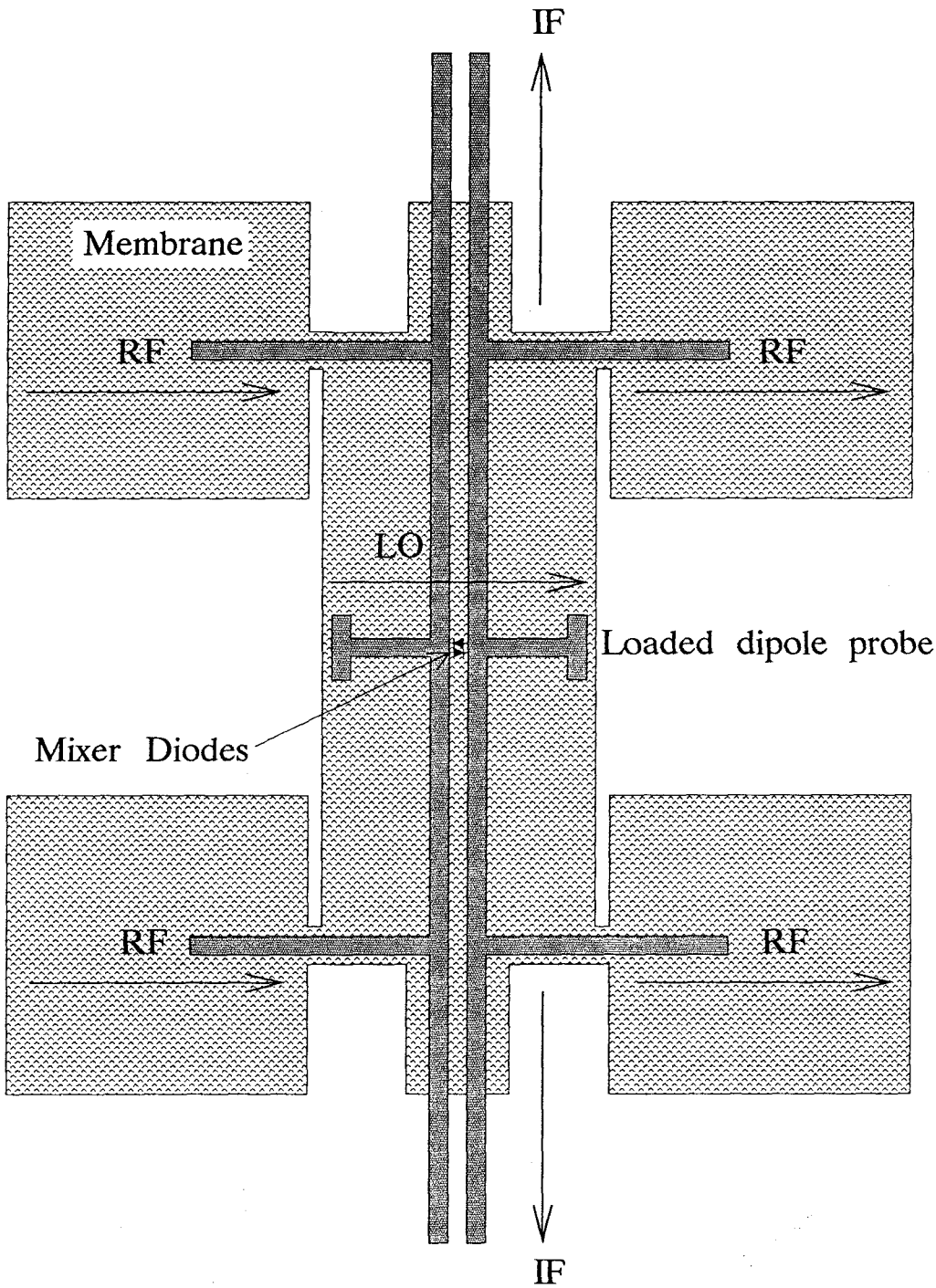

Figure 5.12 The mixer circuit design for a unit cell; four monopoles for the RF reception and one dipole for the LO reception; both RF and LO are detected by the mixer diodes located in the center of the unit cell; IF is led out from the ends of the LO horn through a coplanar-strip transmission line.

5.3 Modeling of the Antenna Probes inside the Horns

Since the quasi-optical antenna-mixer array combines antennas and mixer circuits into a single entity, the design requires consideration of the impedance matching, conversion loss and frequency response in addition to the horn antenna configurations. The antenna probes are required not only to couple the free space wave to the mixer diodes but also to provide a suitable impedance, the embedding impedance, to the mixer diodes. This impedance over a wide frequency range is important on the mixer performance because various frequency components exist in the mixer circuits [6]. In order to achieve an impedance-matched mixer array, the properties of the antenna probes inside the horns have to be studied.

The impedances of various probes were measured in low-frequency modelled-horns, which were made of two different types. One type was a 3×3 array (as shown in Figure 2.2) made of aluminum, and the other type was a half horn made of copper foil sitting on a big copper-clad circuit board that was used as an image plane (Figure 5.13). The half horn on a big ground plane was used in order to eliminate difficulties in modeling the transmission line normally used to feed the dipole in a full horn. These two types of modelled horns were used alternatively, depending on the feed location of the probe inside the horn. The horn opening is 1 λ, and the probe is placed inside the horn at about 0.37 λ away from the apex. The probe element was soldered to an SMA bulkhead feed-through, which was in turn soldered to the copper surface of the image plane. The thickness of the copper foil being used to make probes is about 0.13 mm and the width of the probe is about 1.0 mm. Measurements were done on an HP 8720 or an HP 8510 Network Analyzer, which was calibrated to the end of the test-set cable, using coax standards. The electrical-delay feature was used to remove effectively the line between the test-set cable and the probes. This was done by shorting the probes at the wall of the horn and increasing the electrical delay until the display appeared to be a short on the Smith chart. The impedance of the short varied

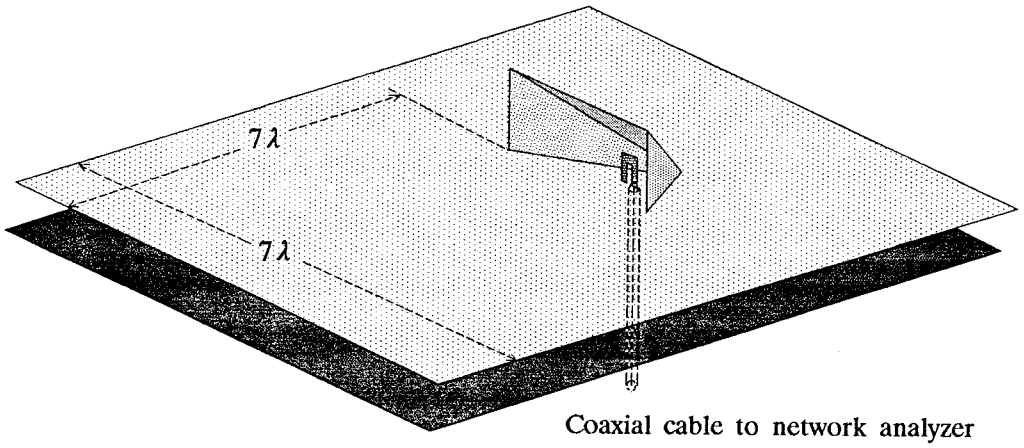

Figure 5.13 The half horn was built on a big ground plane in order to eliminate the difficulties in modeling the transmission line normally used to feed the dipole in a full horn. In this example, a half folded-dipole was built in a half horn.

by less than $2\,\Omega$ over a wide frequency-sweep range of 6 GHz.

The measured probe impedances being plotted on the Smith chart are illustrated in figures from Figure 5.14 to Figure 5.17, with the probe configurations on the top of each Smith chart. All these measurements illustrated in the Smith charts are measured over a range of frequencies for each particular probe, and only those impedances of the probes at the design frequency are marked on the Smith charts. Figure 5.14 shows a monopole being put into a full horn. In the Smith chart, the impedances are plotted as a function of the monopole-probe length. The resonant resistance of $16\,\Omega$ is achieved at the monopole length of $0.22\,\lambda$. In comparison, the resonant resistance of a short, lossless monopole over a big ground plane in the free space is $25\,\Omega$ at the monopole length of $0.25\,\lambda$. Figure 5.15 shows that a folded monopole is put into a full horn, with one leg attached to the coax-center-conductor and the other leg grounded to the horn sidewall. The impedances in the Smith chart are plotted as a function of

the monopole-probe length. The resonant resistance of 50 Ω is obtained at the monopole-probe length of 0.19 λ. This resistance matches the impedance of two mixer diodes connected in antiparallel; hence, this folded monopole is suitable for the LO reception in the fundamentally pumped, antenna-mixer array illustrated in Figure 5.6, in which the folded monopole is a split version. In the free space, however, the resonant resistance of a short, lossless, folded monopole over a big ground plane is about 100 Ω at the folded-monopole-probe length of 0.25 λ. Figure 5.16 shows that a half dipole is built in a half horn. The impedances in the Smith chart are plotted as a function of the half-dipole length. The resonant resistance is 25 Ω at the half-dipole length of 0.20 λ. Since the voltage across the half dipole in the half horn is half that in a full horn, the measured impedances are only *half* of the actual impedances; therefore, for a dipole in a full horn, the resonant resistance is 50 Ω at the full-dipole length of 0.40 λ. This is the same result as was obtained in the full-horn modelling work described in Chapter 2. This dipole probe also provides a very good matching impedance for the mixer diodes pairs. In comparison, the resonant resistance of a short, lossless dipole in the free space is about 50 Ω at the dipole-probe length of 0.50 λ. Figure 5.17 shows a half folded-dipole in a half horn. The impedances in the Smith chart are plotted as a function of the half-dipole-probe length. The resonant resistance of 68 Ω is obtained at the half-dipole-probe length of 0.18 λ. For the same reason stated above, the resonant resistance of a full folded-dipole in a full horn would be 136 Ω at the full-folded-dipole length of 0.36 λ, compared with 200 Ω of a short, lossless folded dipole in the free space. This folded-dipole impedance in the horn needs to be transformed to be about 200 Ω in order to be used as an RF reception element in the fundamentally pumped antenna-mixer-array design (Figure 5.6).

Dipole probes in a rectangular horn, to be used for LO reception in the subharmonically pumped antenna-mixer-array, were also modelled and tested.

These dipole probes were loaded with a short stub on the end near the horn sidewall, which could compensate for the capacitive characteristic impedance of the shorter dipole probe. The half-dipole-probe length is about $0.11\,\lambda$, determined by the height of the rectangular horn. Figure 5.18 shows a half loaded-dipole in a half rectangular-horn. The impedances in the Smith chart are plotted as a function of the loading-stub length d. The measurement is done at 5.0 GHz. The resonant resistance of $18\,\Omega$ is achieved at the loading-stub length of $0.08\,\lambda$, which corresponds to $36\,\Omega$ for a full loaded-dipole in a full horn. In Figure 5.19, it is a half loaded-folded-dipole in a half rectangular-horn. The impedances in the Smith chart are plotted as a function of the loading-stub length d, also measured at 5.0 GHz. The resonant resistance of $54\,\Omega$, or $108\,\Omega$ for a full loaded-folded-dipole, is obtained at the loading-stub length of $0.12\,\lambda$. This probe could provide a suitable matching impedance for single-diode mixers. Figure 5.20 shows the impedances in the Smith chart plotted as a function of the frequency for the same probe design as shown in Figure 5.18, but this time, the loading-stub length is fixed at the resonant length of $0.08\,\lambda$ at the design frequency of 5.0 GHz. This plot shows how the probe impedance changes over a wide-frequency range beyond the design frequency.

All these impedance measurements indicate that the presence of the horn increases the effective length of the probe element, which basically agreed well with the millimeter-wave aperture efficiency measurements presented in Chapter 4, in which a dipole probe was used as an antenna element. They also indicate that the resonant frequencies can be controlled by loading the probes and that resonant resistances can be increased to a reasonable matching range by folding the probes. These modelling measurements provide very useful options in choosing reception-probe elements in the design of the quasi-optical horn-antenna-mixer arrays.

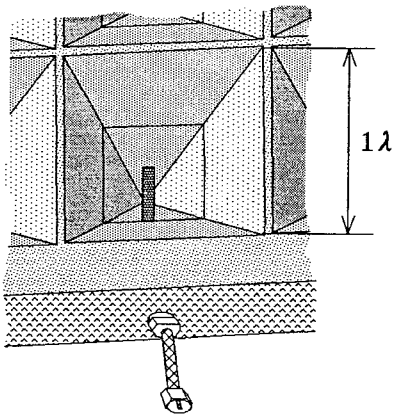

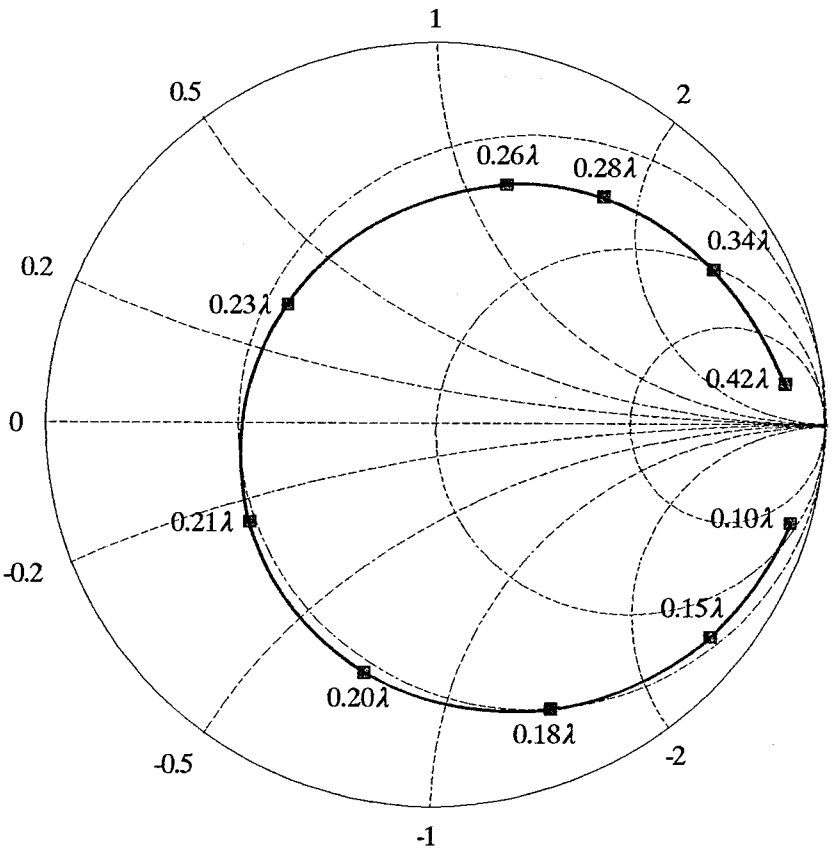

Figure 5.14 A monopole in a full horn; the impedances in the Smith chart are plotted as a function of the monopole length, measured at 4.9 GHz; the resonant resistance is 16 Ω at the monopole length of 0.22 λ.

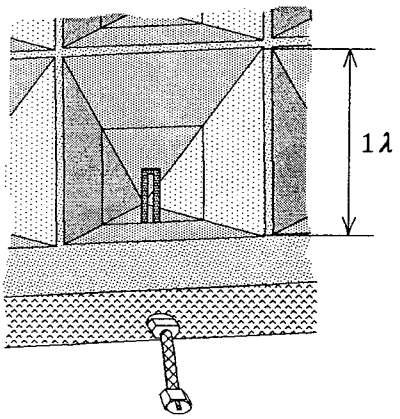

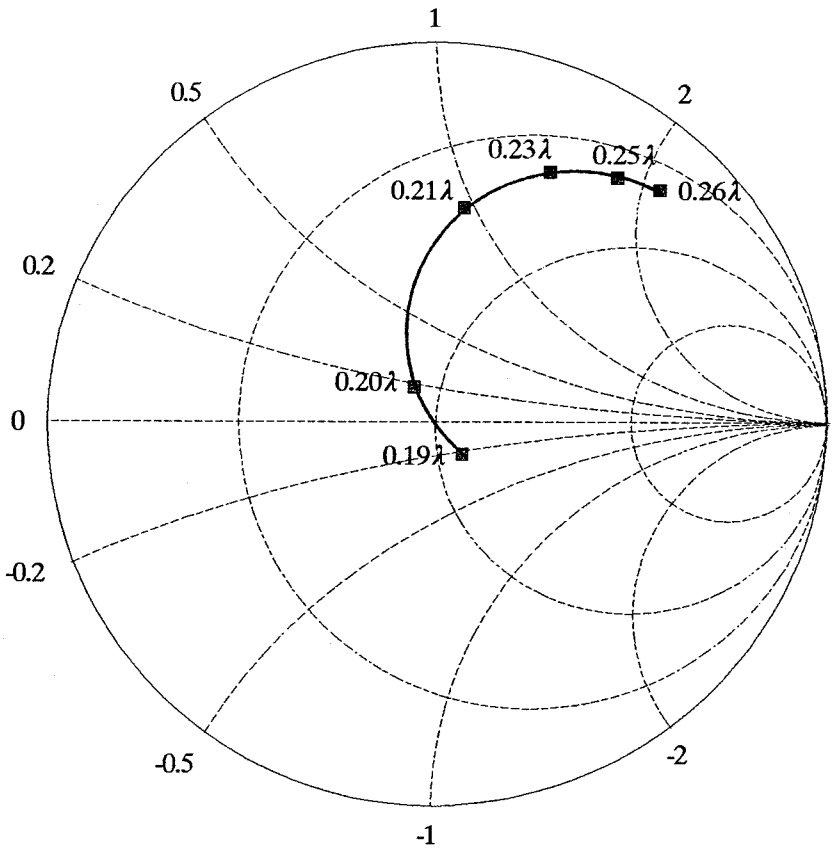

Figure 5.15 A folded monopole in a full horn; the impedances in the Smith chart are plotted as a function of the monopole-probe length, measured at 4.9 GHz; the resonant resistance is 50 Ω at the probe length of 0.19 λ.

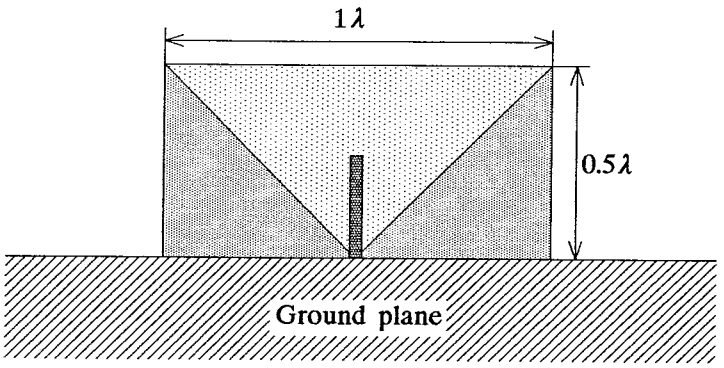

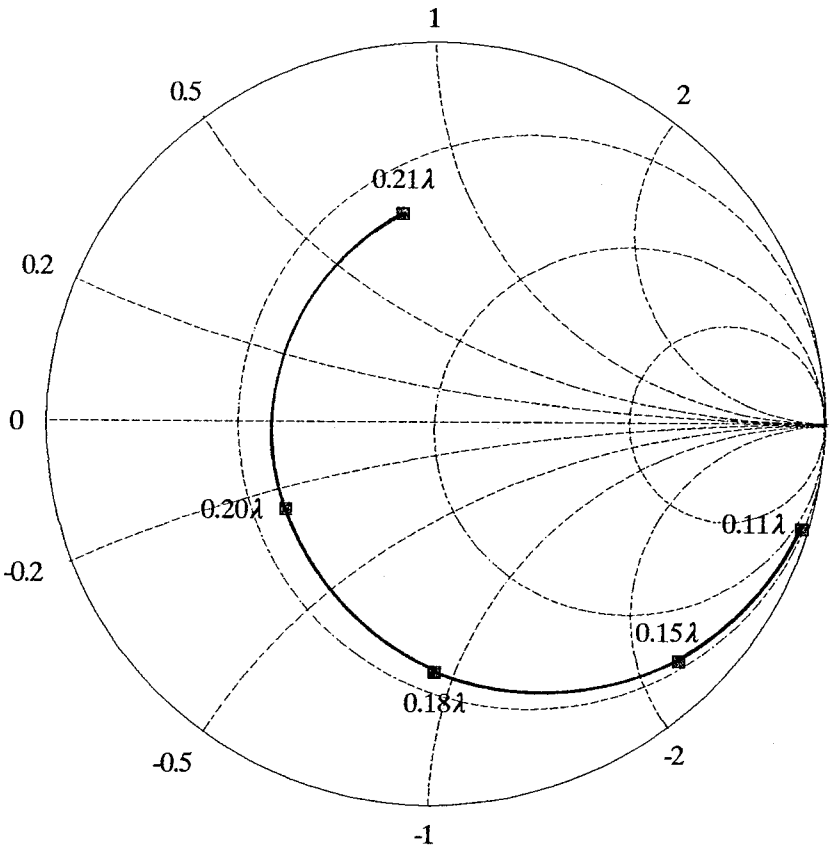

Figure 5.16 A half dipole in a half horn; the impedances in the Smith chart are plotted as a function of the half-dipole length, measured at 4.9 GHz; the resonant resistance is 25 Ω at the half-dipole length of 0.20 λ.

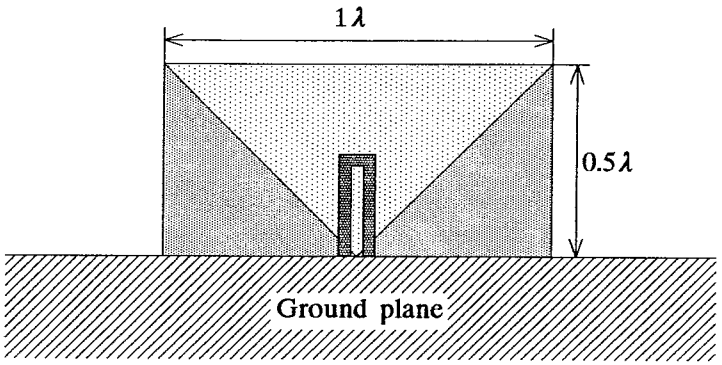

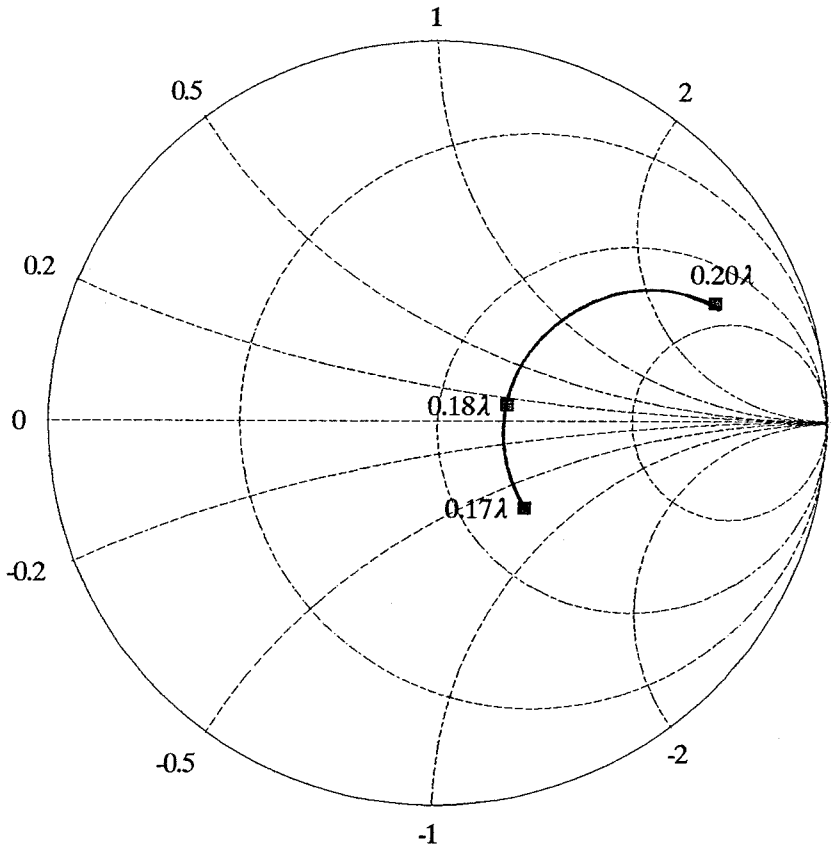

Figure 5.17 A half folded-dipole in a half horn; the impedances in the Smith chart are plotted as a function of the half-dipole length, measured at 4.9 GHz; the resonant resistance is 68 Ω at the half-dipole length of 0.18 λ.

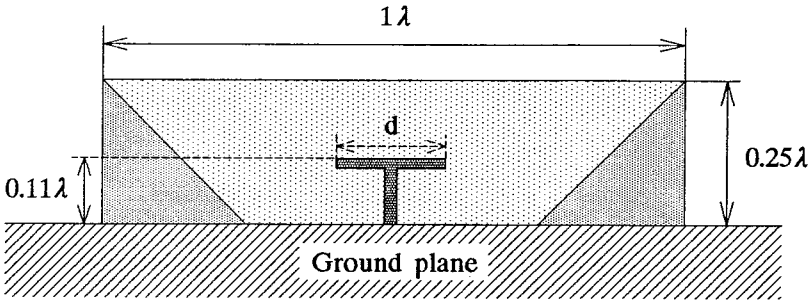

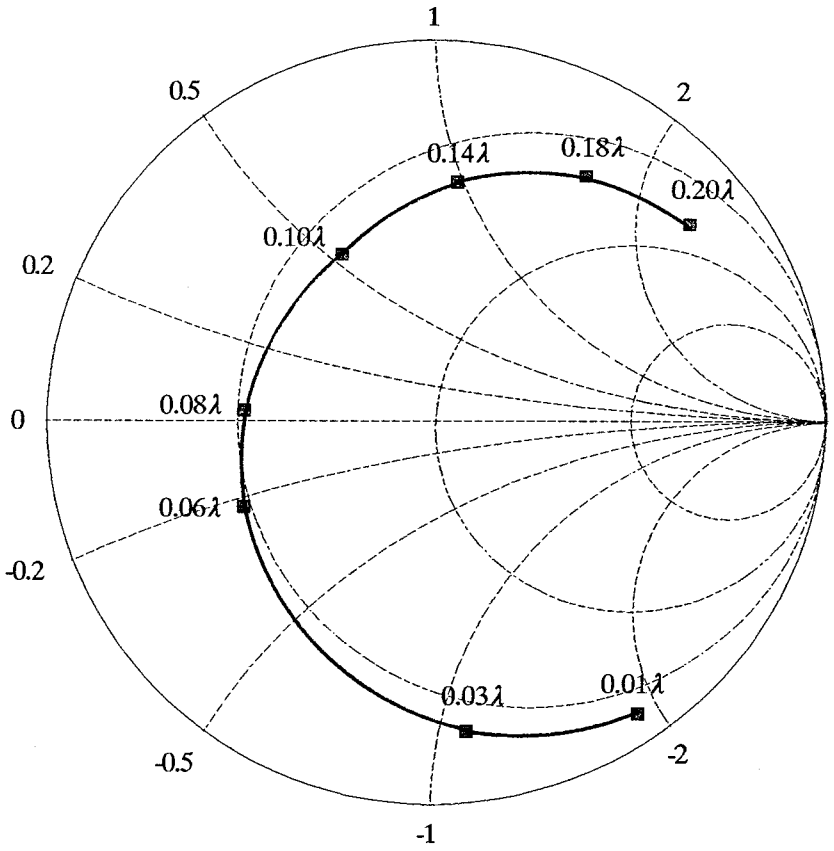

Figure 5.18 A half loaded-dipole in a half rectangular-horn; the impedances in the Smith chart are plotted as a function of the loading-stub length d, measured at 5.0 GHz; the resonant resistance is 18 Ω at the loading-stub length of 0.08 λ.

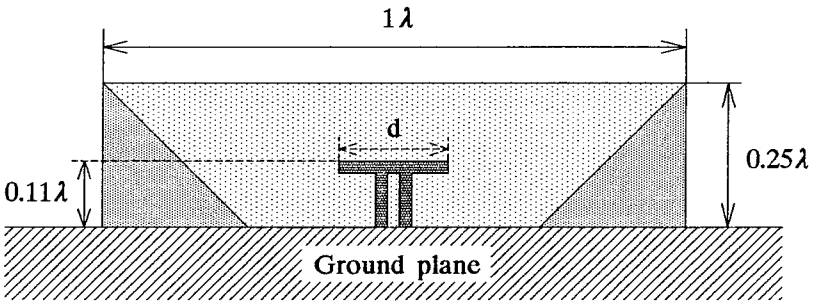

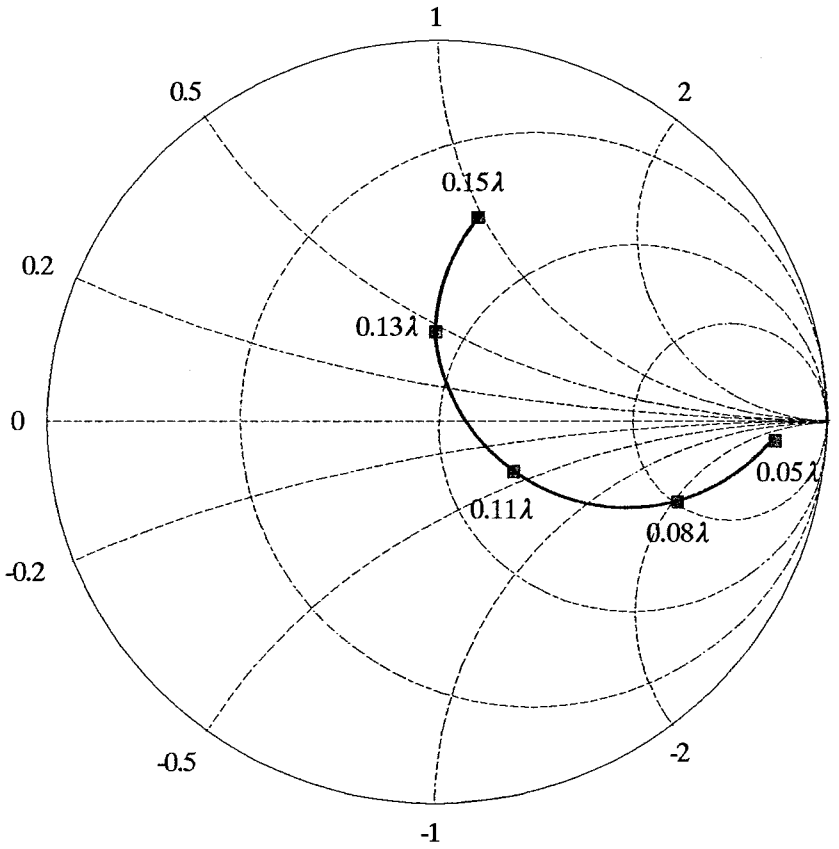

Figure 5.19 A half loaded-folded-dipole in a half rectangular-horn; the impedances in the Smith chart are plotted as a function of the loading-stub length d, measured at 5.0 GHz; the resonant resistance is 54 Ω at the loading-stub length of 0.12 λ.

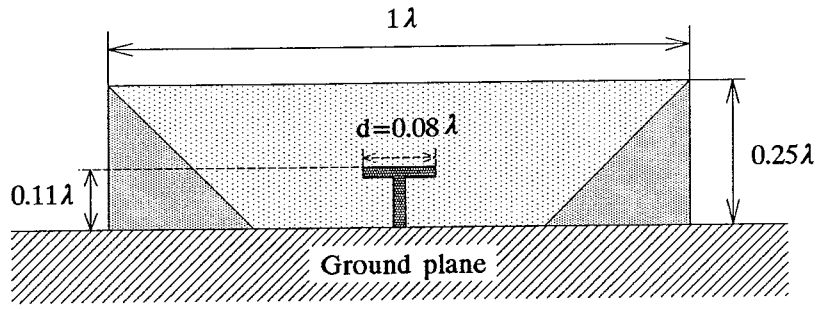

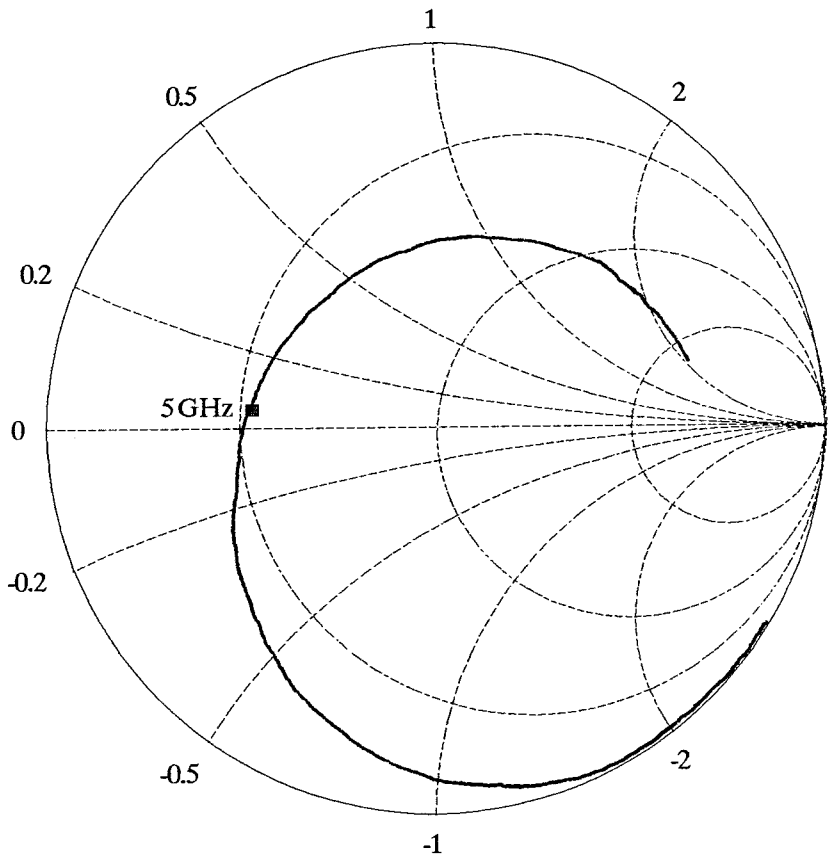

Start 2.0 GHz

Stop 8.0 GHz

Figure 5.20 A half loaded-dipole in a half rectangular-horn; the loading-stub length d is fixed to $0.08\,\lambda$; the impedances in the Smith chart are plotted as a function of the frequency, swept from 2.0 to 8.0 GHz; the resonant resistance is $18\,\Omega$ at the design frequency of 5.0 GHz.

References

[1] Stephen A. Maas, *Microwave Mixers*, Artech House, Inc., Dedham, Massachusetts, 1986.

[2] Courtesy of Professor Gabriel Rebeiz (The University of Michigan) and Kent Potter (Engineer, Caltech).

[3] K.D. Stephan and G. Perks, "Quasi-Optical Slot Ring Mixer Noise Figure Measurements," *1985 IEEE MTT–S Digest*, pp 643-644, 1985.

[4] Erik L. Kollberg, "Microwave and Millimeter-Wave Mixers," A volume in the IEEE Press selected reprint series, IEEE Inc., New York, 1984.

[5] M.V. Schneider, W.N. Snell, Jr, "Stripline Down-Converter with Subharmonic Pump," *Bell System Tech. Journal*, vol. 53, n. 7, pp. 1179-1183, July-August, 1974.

[6] D.N. Held, A.R. Kerr, "Conversion Loss and Noise of Microwave and Millimeter-Wave Mixers: Part I - Theory," *IEEE Trans. Microwave Theory and Techniques*, vol. MTT-26, n. 2, pp. 49-54, February 1978.

Chapter 6

Back-to-Back Horn-Antenna-Mixer Array Measurements

For millimeter-wave mixers, it is usually expensive and inconvenient to generate an LO power at a frequency close to RF. A subharmonically pumped mixer, however, is pumped at about only half the RF frequency, which mixes the RF signal with the second harmonic of the LO frequency. The performance of the mixer is comparable to fundamentally pumped mixers. Since the RF and the LO frequencies differ by approximately a factor of two, in principle, it is easier to realize the isolation between the RF and the LO. Furthermore, spurious responses associated with the odd harmonics of the LO can be rejected by using an antiparallel diode pair. Among the designs of the antenna-mixer arrays presented in Chapter 5, the subharmonically pumped horn-antenna-mixer array shown in Figures 5.10, 5.11, 5.12 has been constructed and tested on a scaled model sub-array, which consists of four RF horns and one LO horn. The gain of such a sub-array will be increased by a factor of 4 compared with a single horn. Based on this scaled model sub-array, antenna impedances and receiving patterns were measured. Additionally, various mixer circuits have been tested in order to achieve better isolation between the RF and the LO, as well as to match the impedances of the RF and the LO to the diode impedance. Trade-off has been made among the impedance match and the isolation between the RF and the LO so as to minimize losses.

6.1 Antenna-Mixer Sub-Array

In the subharmonically pumped horn-antenna-mixer array shown in Figures 5.10, 5.11, 5.12, every four RF horns can be taken as a sub-array. The four RF horns, together with one LO horn, form a unit-cell, which has been constructed using scaled-model horns made of copper foil. The unit-cell consists of two square RF horns and a half rectangular LO horn sitting on a big copper-clad circuit board, which was used as an image plane (Figure 6.1). The circuit board is as big as $10\,\lambda$ long on each side of the horns and the total width of the board is $10\,\lambda_{LO}$. Looking from RF side, it seems that there are four RF horns, but as a matter of fact, the lower two horns are the image of the top two real RF horns. Similarly, the half LO horn looks like a full horn from LO side. The monopole built in each of the four RF horns will couple the incoming signals to the loaded dipole in the LO horn through the coplanar-strip transmission line. A small channel in the middle of the horns will let the monopole probes go through between the LO and RF horns. The design frequency for the RF is 10 GHz and the LO is 5 GHz, corresponding to the wavelength of 3 cm and 6 cm, respectively. The opening of RF horns is $1\,\lambda_{RF}$ square, while the height of the LO horn is $\lambda_{LO}/2$, and the LO horn width is $1\,\lambda_{LO}$. Mixer diodes are to be placed in the center of the dipole probe in the LO horn (as shown in Figure 5.12). An SMA bulkhead feed-through connector is soldered from the back of the circuit board to the place where the diodes are supposed to be. The inner conductor of the connector is soldered to the dipole probe, and the outside conductor is soldered to the circuit board used as a ground plane.

Measurements were done on an HP 8510 Network Analyzer and data were collected by a PC computer. Full two-port calibration was made in order to measure not only the reflection coefficients but also the receiving properties and the isolation between the RF port and LO port. Similarly to the calibration in the probe modelling measurements, the network analyzer was calibrated to

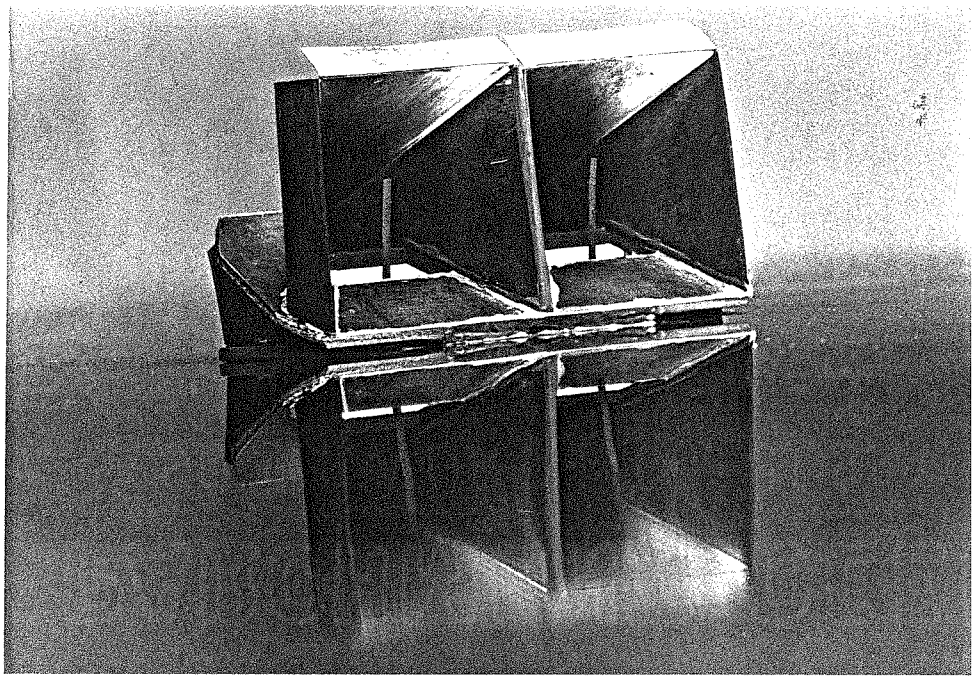

(a)

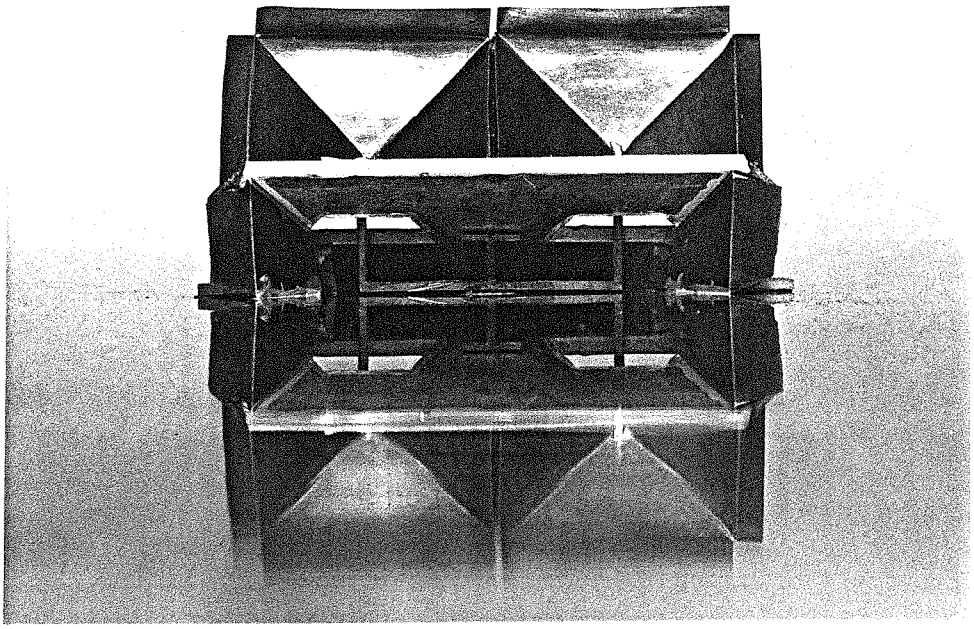

(b)

Figure 6.1 The modelled antenna-mixer-array unit-cell, looking from RF side (a) and looking from LO side (b).

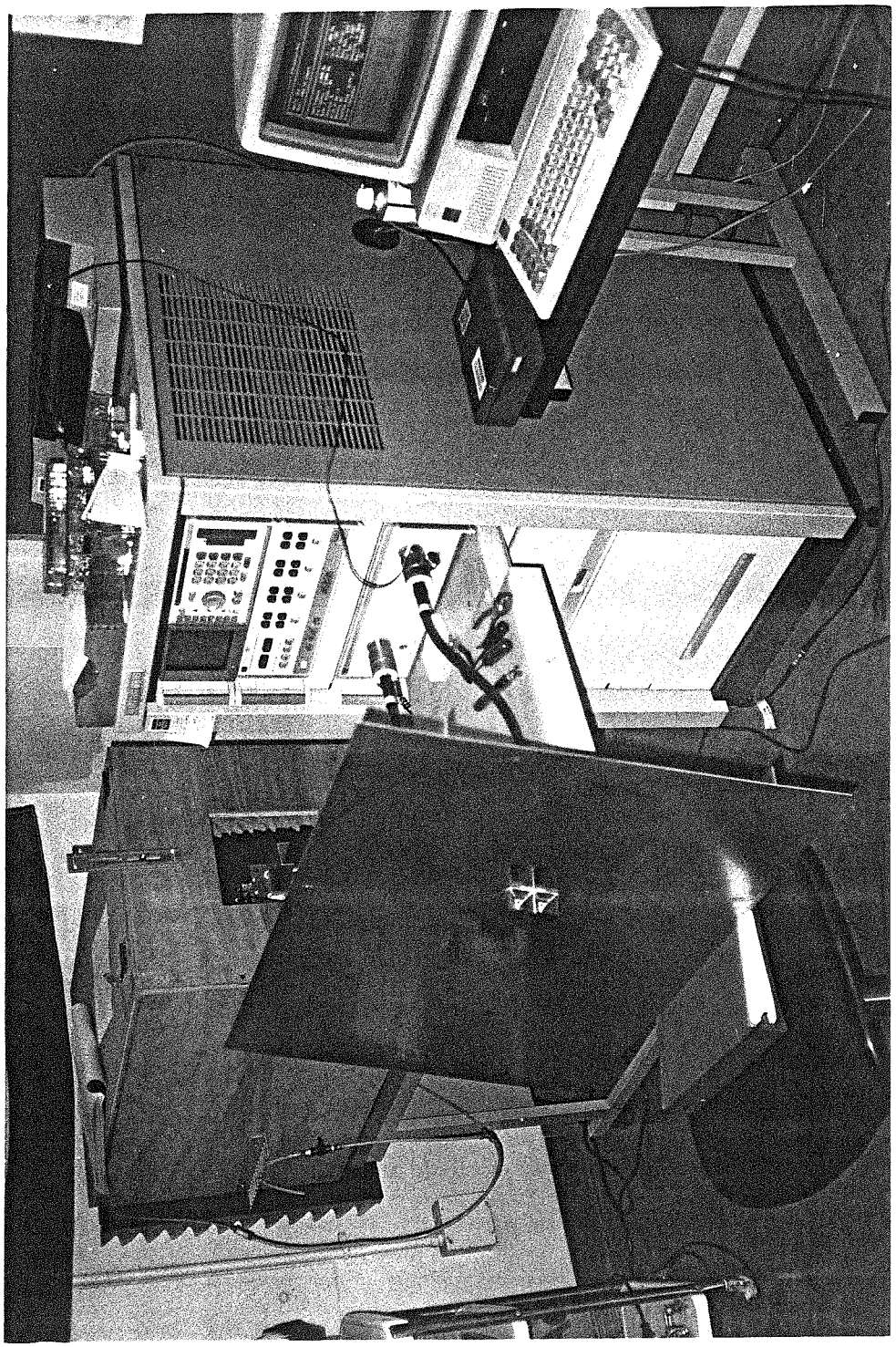

Figure 6.2 The test setup for the modelled antenna-mixer sub-array. The measurements were done on an HP 8510 Network Analyzer; the data were collected by a PC computer; a broad-band horn antenna was used to test the power receptions.

the ends of the test-set cable using coax standards. The electrical-delay feature was used to remove effectively the extra line of the connector between the test-set cable and the mixer circuit. The impedance of the calibration short varied by less than 2 Ω over a frequency-sweep range from 2 GHz to 12 GHz. The measurement setup is shown in Figure 6.2. Beside the measurements of the impedances (from S_{11} parameter), the power receptions were also measured by measuring the transmission coefficient S_{12}, using a broad-band horn antenna as a transmitting horn that has a working frequency range from 2 GHz to 18 GHz.

6.2 Antenna-Mixer Sub-Array Measurements

To start with, a simple mixer-circuit design is used, shown in Figure 6.3. The reason for the membrane pattern in Figure 6.3 to be a little different from the one shown in Figure 5.12 is that a membrane, patterned by a mask with too many corners, breaks more easily when it is etched. Therefore, in this design, the pattern on the membrane wafer is made in such a way that the walls between the RF and LO horns are completely removed, resulting in smoother transitions between the horns. The shape of each unit-cell on the membrane wafer looks like a big "I," so it is called the "big 'I' design." The measured impedances are marked on the Smith chart in Figure 6.4. Although the impedances were measured on only a half unit-cell, consisting of two RF horns and a half LO horn, the impedances in a full unit-cell can be easily obtained by doubling those measured impedances in the half unit-cell. The impedances in Figure 6.4, as well as in the other following Smith charts, have been doubled and plotted by using Puff, a software CAD program [1]. Both the RF and the LO impedance should be matched to 50 Ω because each beam-lead diode in the antiparallel diode pair has a resistance of about 100 Ω.

In Figure 6.4, when the loading stub on the dipole decreases in length, the LO impedance at 5 GHz changes from the inductive to the capacitive impedance,

passing the resonant resistance at about 50 Ω, which is a very good matching impedance for the diode pair. This LO impedance of the circuit can be regarded as the LO dipole-probe impedance parallel with the impedance of the coplanar transmission line plus the RF probes. At 5 GHz, the impedance of the coplanar transmission line plus the RF probes is very high as is illustrated by the LO frequency mark "5" when the entire LO dipole probe is taken away. Hence, the resonant LO impedance is mainly determined by the loaded dipole probe and is relative independent of rest of the circuits. On the other hand, the RF impedances at 10 GHz are pretty high and independent of the loading-stub length changes. The average value of those RF impedances at 10 GHz is about $84 + j82\,\Omega$. Figure 6.5 shows that the mixer circuit impedances are plotted on the Smith chart as a function of the sweeping frequency, from 2.0 to 12.0 GHz, with the loading-stub length d being fixed at $0.08\,\lambda_{LO}$. The plot indicates that the impedances are quite high at high frequencies, which is to be investigated and discussed further in Section 6.3.

The normal-incident power receptions by the RF and the LO horns were tested over a wide frequency range, from 2.0 GHz to 12.0 GHz. This was done by putting a wide-band transmitting horn (connected to port 2 of the network analyzer) in the front side of the RF horns or the LO horn at about 30 cm away and measuring the S_{12} parameter. Figure 6.6 shows the measured power received by the RF horns when the transmitting horn is in the front side of them (solid line) and by the LO horn when the transmitting is in the front side of it (dashed line). At the LO frequency of 5 GHz, the difference between the LO and the RF power is defined as the LO-RF isolation. From the point of view of eliminating the losses, the higher isolation, the lower the coupling loss will be, under the condition that other parameters stay the same. For example, the 13 dB LO-RF isolation shown in the graph indicates that 5 % of the received LO power will re-radiate through the RF horns; if the LO-RF isolation was 20 dB, then the

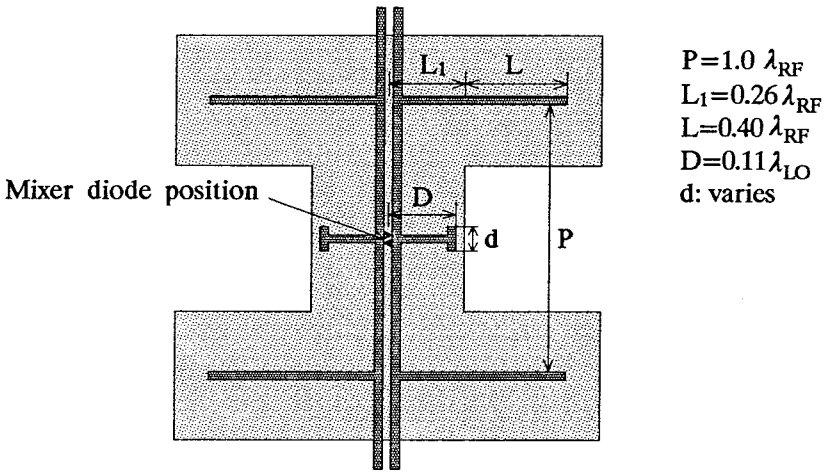

Figure 6.3 One of the mixer circuit designs for the sub-array; monopoles for the RF reception and a dipole for the LO; IF is led out from the two ends.

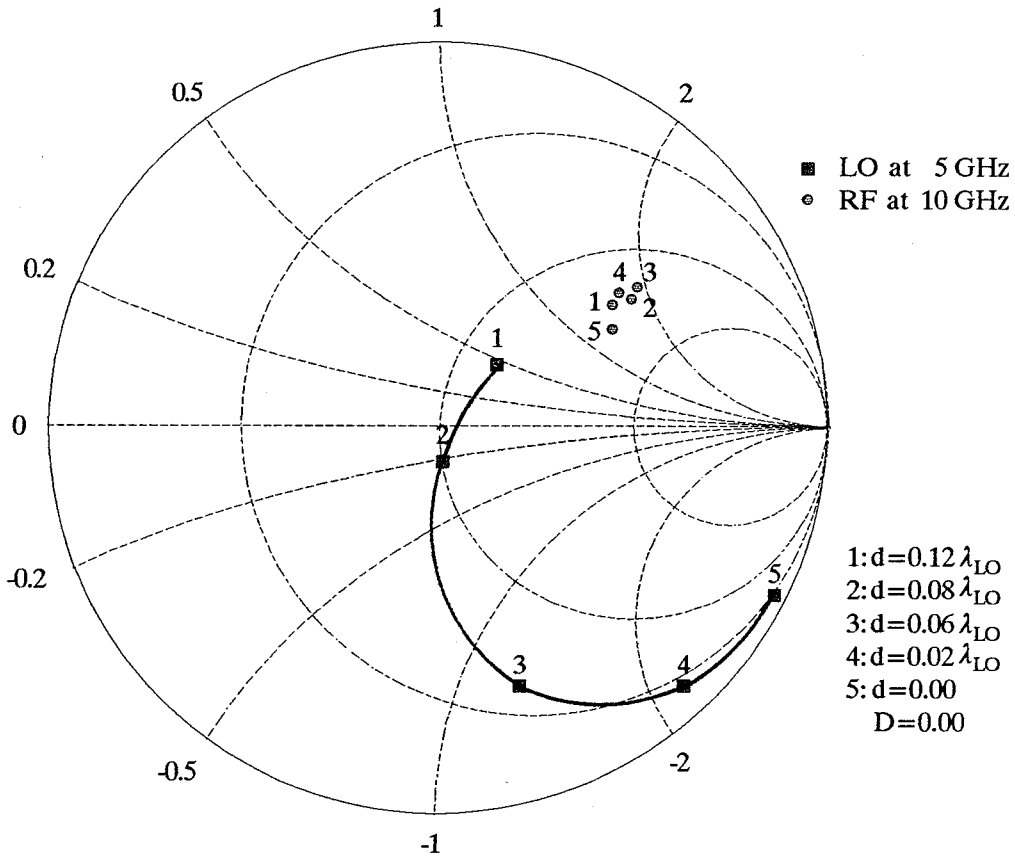

Figure 6.4 The circuit impedances indicated on the Smith chart with respect to the different loading-stub length d; measured at 10 GHz for the RF and 5 GHz for the LO.

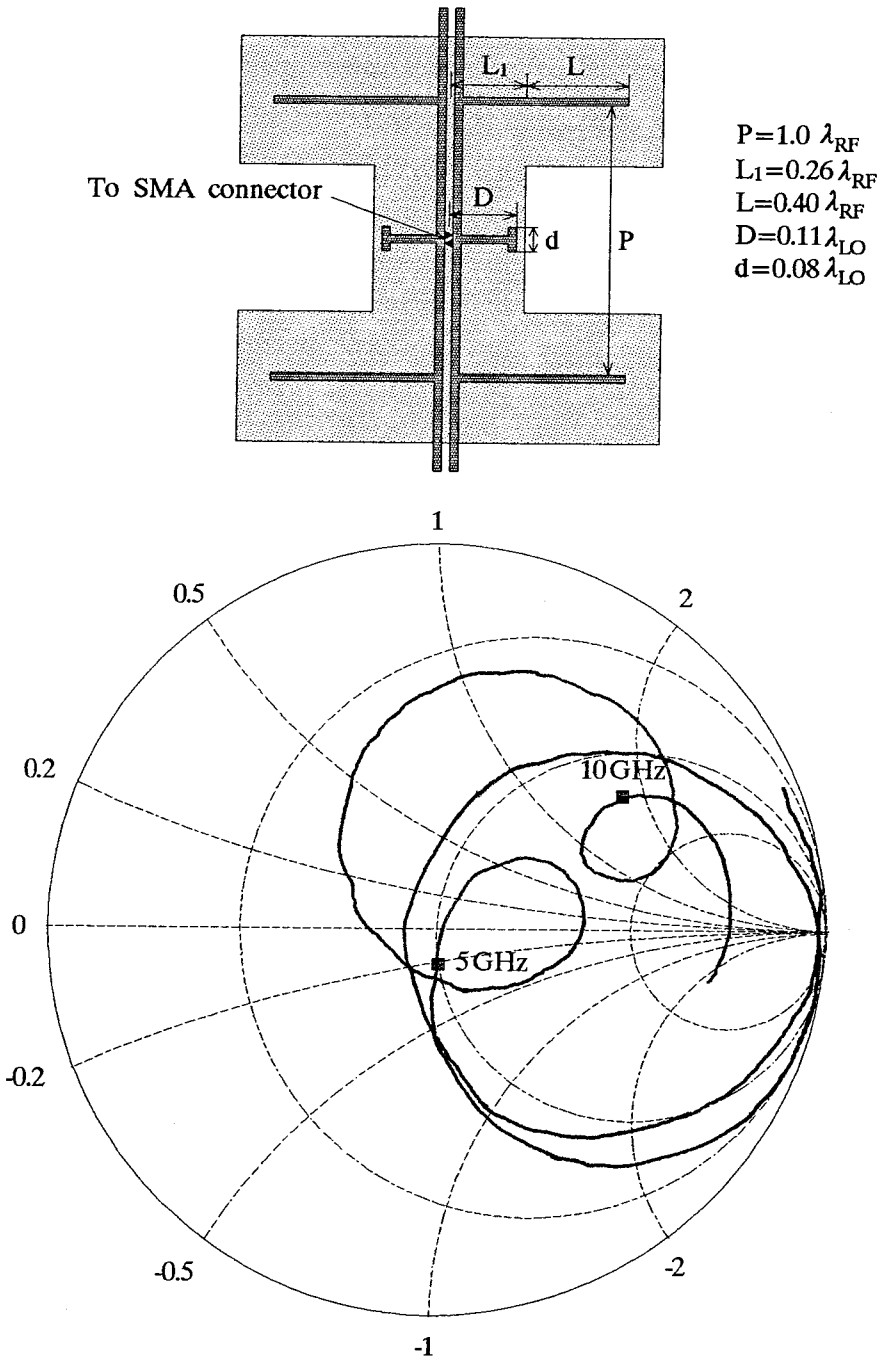

Figure 6.5 The same circuit design as the one in Figure 6.3, but the loading-stub length d is fixed at $0.08\,\lambda_{LO}$; circuit impedances are plotted on the Smith chart as a function of the sweeping frequency from 2.0 to 12.0 GHz.

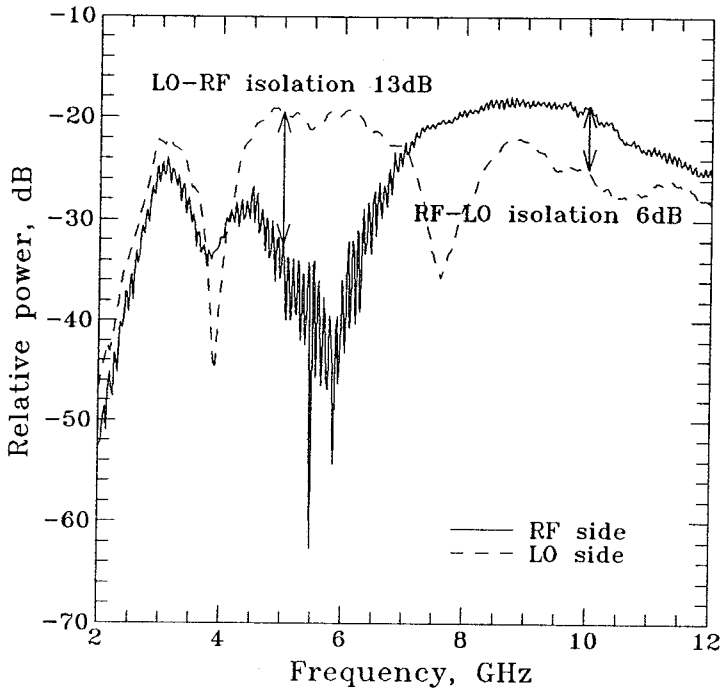

Figure 6.6 Measured normal-incident power, received by the RF horns (solid line) and by the LO horn (dashed line). The distances in the two measurements are equal.

loss would be only 1 %. Similarly, the RF-LO isolation is the power difference between RF and LO at the RF frequency of 10 GHz. The measured RF-LO isolation is 6 dB or a 25 % loss, which is pretty high. The reason for the loss caused by the LO-RF coupling to be relative low is that the frequency of the LO is below the cutoff frequency in the RF horns. On the other hand, RF power will propagate easily in the LO horns represented by higher modes. The RF-LO isolation should be increased to reduce the coupling loss, which will be discussed further in Section 6.4.

Patterns in the H-plane were measured on both the RF horns and the LO horn. The RF horn sub-array can be considered as a linear array, and the pattern is a multiplication of the single RF horn [2]. Theoretical patterns of the sub-array

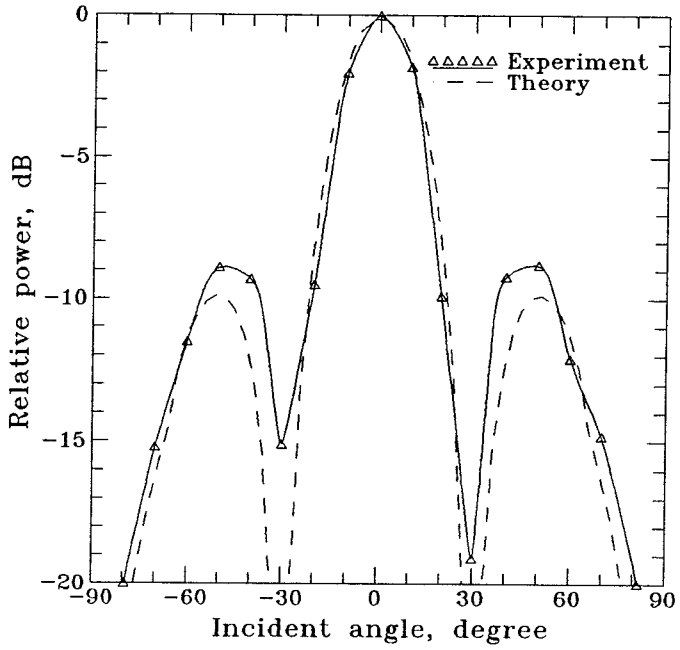

(a)

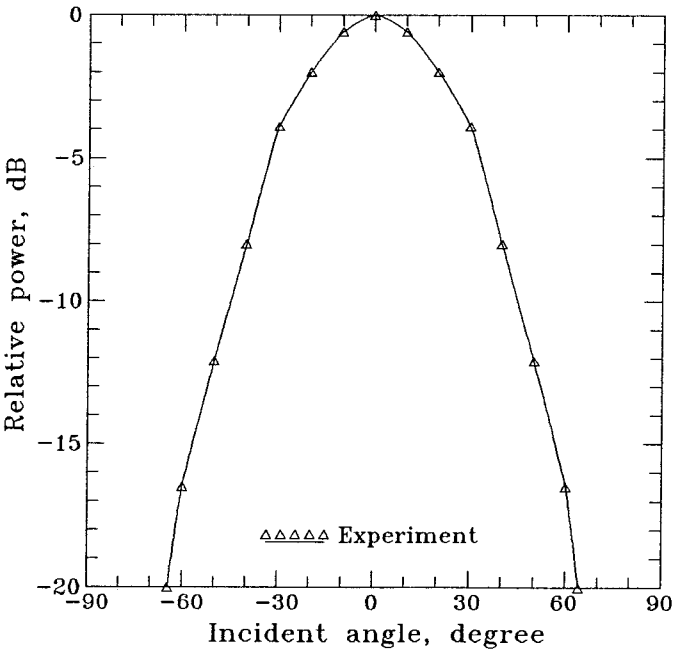

(b)

Figure 6.7 H-plane patterns of the sub-array; RF horns measured at 10 GHz (a) and the LO horn at 5 GHz (b).

can be obtained by multiplying the theoretical pattern of a single horn [3] with an array function. For a uniform, one-dimensional array, spaced by a distance d, excited with the same constant amplitude I_0, the array function can be written as the following

$$F = I_0 e^{j(N/2)(\alpha + k_0 \cos\psi)d} \frac{\sin\{[(N+1)/2](\alpha + k_0 \cos\psi)d\}}{\sin[(\alpha + k_0 \cos\psi)d/2]} \tag{6.1}$$

where N is the number of elements, α is the phase-change factor from element to element, $k_0 = 2\pi/\lambda$ and ψ is the incident angle. Measured H-plane patterns of RF at 5 GHz and of LO at 10 GHz were shown in Figure 6.7, together with the RF theoretical pattern. The LO pattern shows no sidelobes and the RF pattern agrees well with the theory. But the sidelobes of the RF horn are quite high, which comes from the wide flair angle of the RF horns bounded by the (111) crystal planes. If high-gain, step-profiled horns [4] are utilized, the sidelobes would be reduced tremendously.

6.3 Antenna Impedance Analysis

To summarize the measurements of the circuit configuration shown in Figure 6.3, the best matched LO impedance of about 50 Ω has been achieved and the LO-RF isolation is 13 dB. Of the four concerned parameters, namely, RF impedance, LO impedance, RF-LO isolation and LO-RF isolation, there are still two parameters that need to be improved or understood. This section will emphasize the RF impedance analysis, and Section 6.4 will address the issue of the RF-LO isolation.

In order to simplify the problem, the LO dipole probe is removed, shown in Figure 6.8 together with the measured impedances marked in the Smith chart. As long as the measured impedance of the circuit configuration at the LO frequency stays high; then, the actual LO impedance with the LO probe in position will not be affected because the LO dipole probe has a low resonant impedance

parallelled with the rest of the circuit. On the other hand, the dipole probe in a rectangular horn has a very high impedance (Figure 5.20) at high frequencies; therefore, removing the LO probe will have little effect on the RF impedance. The measured results show that the RF impedance does not go down when the spacing of the RF probes is changed, and the RF-LO isolation has not been improved either. In another attempt, the portion of coplanar strips used for IF leads has been removed (the top part in Figure 6.9), since the coplanar-strip transmission line used to be shorted at each end, which could be a big load at the RF frequency, causing the high RF impedances. To verify this assumption, the circuit design in Figure 6.9 has been measured and impedances are marked on the Smith chart. The RF impedance goes from inductive to capacitive as the RF probe decreases, but the resonant impedance is still not satisfactory low. In analyzing all these measurement results, which include the results in Figures 6.9, 6.8, 6.5, 6.4 and Figure 5.14, it is believed that the high RF impedance is caused by the effect of the long RF monopole probes ($L + L_1 \gg 0.22\lambda$; see Figure 5.14). For this particular sub-array design, the RF impedance will not decrease to the desirable value unless the total length of the monopole probe is greatly reduced, which is impossible to do. If the RF probe is too short, then there will not be any coupling elements for the RF power reception. To understand this, the RF power reception versus various monopole probe lengths has been measured and is shown in Figure 6.10. The RF horns have maximum power reception when the probe length is about $0.3\sim0.4\lambda_{\mathrm{RF}}$. This means that the total RF probe length $L + L_1$ is in the range of $0.5\sim0.6\lambda_{\mathrm{RF}}$. One of the trade-offs in this simple circuit design is between the better RF matching impedance and receiving the RF power at all.

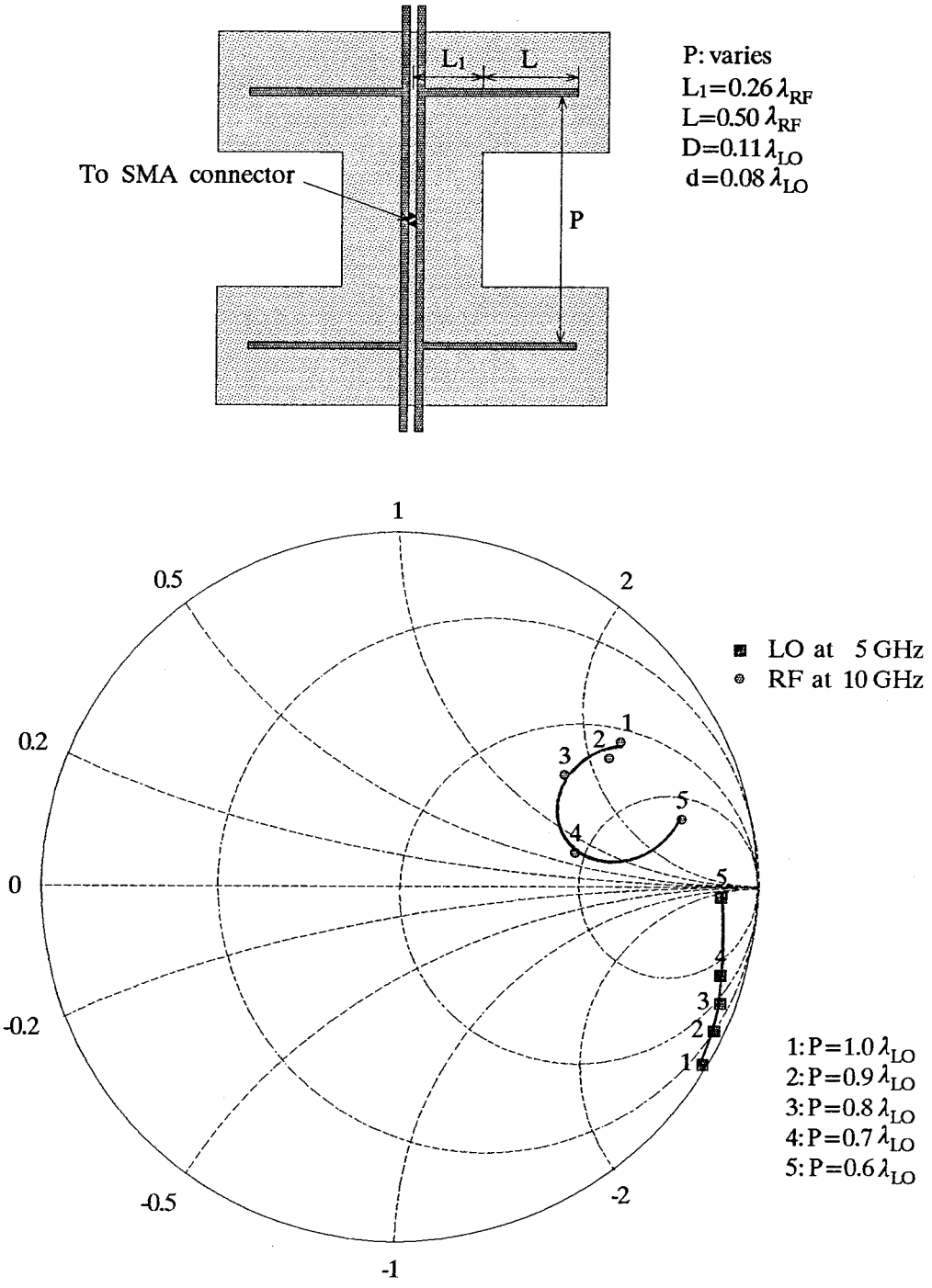

Figure 6.8 The LO dipole probe being removed; the circuit impedances are marked on the Smith chart as a function of the distance P between the two RF monopole probes.

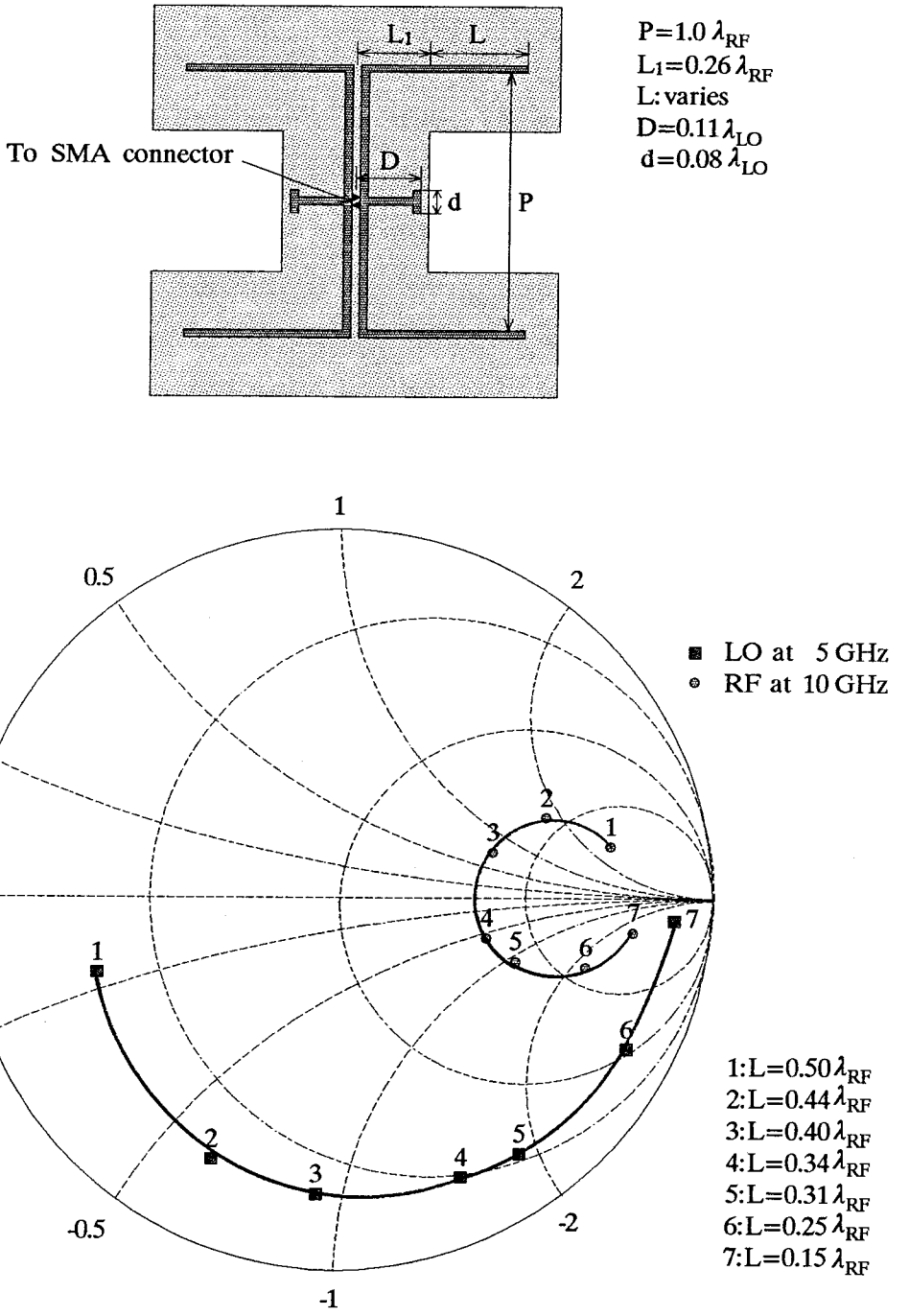

Figure 6.9 The segments for the IF leads being removed; the circuit impedances are marked on the Smith chart as a function of the length L of the RF monopole probes.

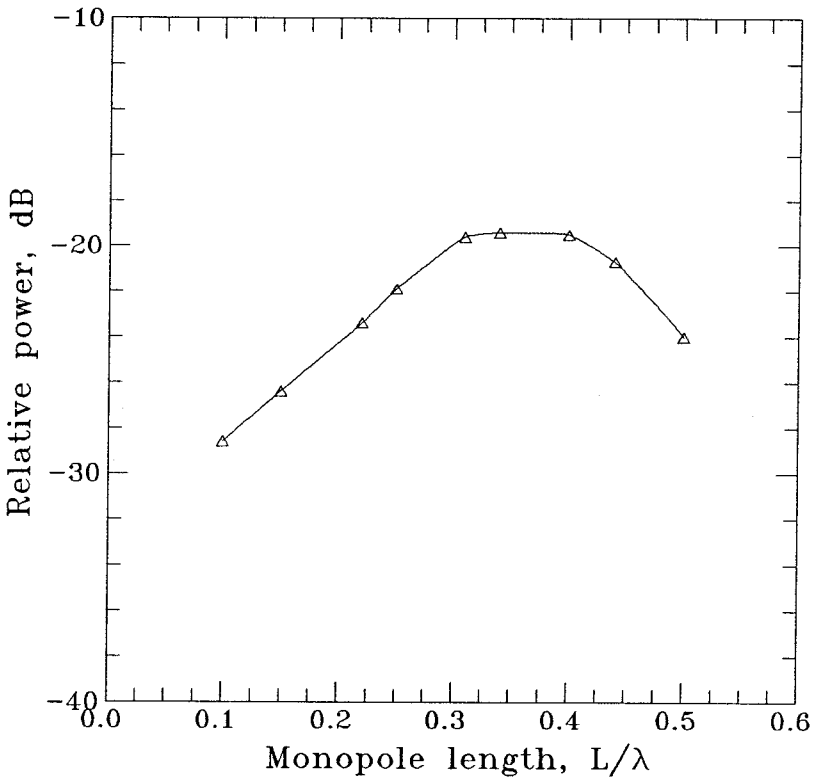

Figure 6.10 The measured normal-incident power received by the RF horns at various monopole probe lengths.

6.4 RF-LO Isolation

As was shown in Figure 6.6, the RF-LO isolation is only 6 dB, resulting in 25 % of the received RF power re-radiating from the LO horn. This is because the RF probes appear in the LO horn (see Figure 6.1), and these segments of the RF probes re-radiate the received RF power through the LO horn. To avoid such a re-radiation, the segments of the RF probes in the LO horn are moved close to the LO horn sidewalls where the tangential electric field is the minimum (Figure 6.11). On the other hand, in order to control the way higher modes are being excited, the LO probe is split into two identical ones. By changing the spacing P_1 between the two LO probes, fields at certain frequencies will cancel and produce no radiation. This circuit configuration is called the "split-LO-probe design" in distinguishing it from the "simple-probe design" (Figure 6.3). The measured impedances over a range of frequencies as well as the circuit design are shown in Figure 6.11. At the LO frequency of 4.5 GHz, the impedance is close to 50 Ω, but at the RF frequency of 9.5 GHz, the impedance is still too high, $78 + j178\,\Omega$. Nevertheless, the RF-LO isolation has been improved from 6 dB up to 20 dB, shown in Figure 6.12. While the LO-RF isolation is 14 dB, which is about the same as the simple-probe design (Figure 6.6). In the split-LO-probe design, IF frequency is chosen to be 0.5 GHz.

In comparison to the simple-probe design and the split-LO-probe design, the impedance-mismatch losses and the coupling losses of the two designs are listed in the table in Figure 6.13. The impedance-mismatch losses are calculated using

$$L_m = \frac{4R_dR_p}{(R_s^2 + X_p^2)} \tag{6.2}$$

where R_d is the diode-pair resistance; R_p is the probe resistance; R_s is the sum of the diode and the probe resistance; and X_p is the probe-reactive impedance. For both designs, the biggest loss comes from the RF-impedance mismatch, 1.7 dB

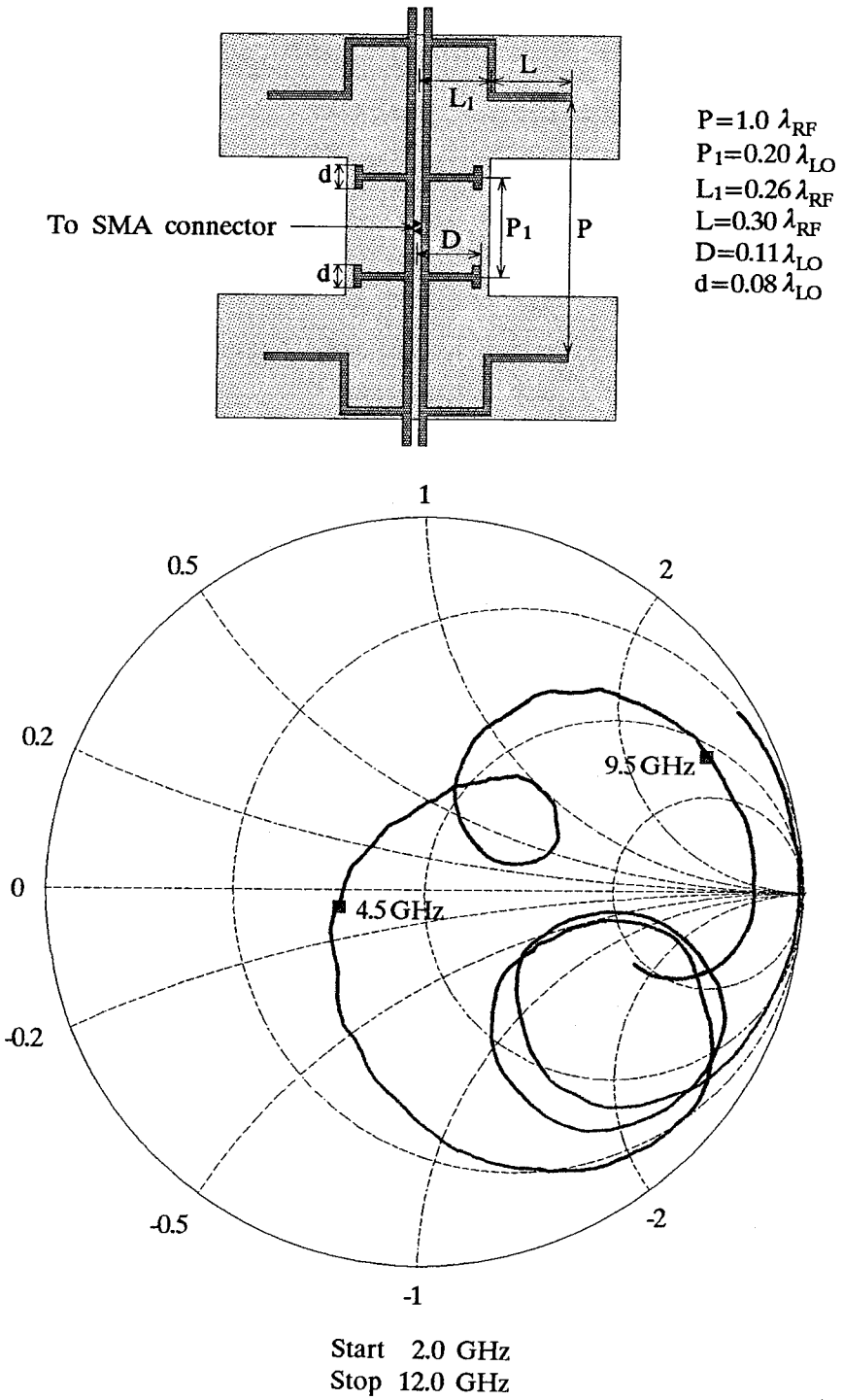

Figure 6.11 The split-LO-probe design; segments of the RF probes in the LO horn are moved close to the LO horn sidewalls; the circuit impedances are plotted on the Smith chart as a function of the sweeping frequencies.

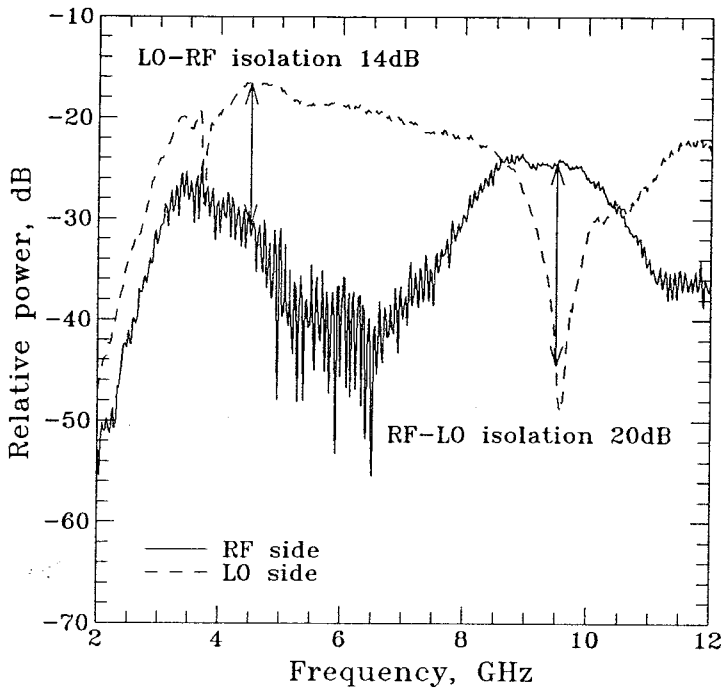

Figure 6.12 Measured normal-incident power on the split-LO-probe design, received by the RF horns (solid line) and by the LO horn (dashed line). The distances in the two measurements are equal.

for the simple probe and 4.9 dB for the split-LO-probe. One way to reduce the RF-mismatch loss is to use the lower side-band as the RF frequency. For example, in the split-LO-probe design, if the signal-image frequency 8.5 GHz

Loss component	Simple-probe design	Split-LO-probe design
RF mismatch, dB	1.7	4.9
LO mismatch, dB	0.0	0.2
RF-LO coupling, dB	1.3	0.0
LO-RF coupling, dB	0.2	0.2

Figure 6.13 Summary and comparison of the impedance-mismatch losses and the coupling losses between the two different mixer circuit designs.

is used for the RF rather than the 9.5 GHz, then the RF impedance would be $43 + j83\,\Omega$, and the impedance-mismatch loss would be reduced from 4.9 dB to 2.6 dB, which also means that the total RF loss is 2.6 dB.

The E-plane and H-plane patterns were measured on this split-LO-probe design. Notice that H-plane patterns are the full scan measurements from $-90°$ to 90°, while the E-plane patterns are measured only from 0° to 90°, and then they are symmetrically flipped over to the other half plane. Figure 6.14 shows the patterns measured on the RF horns at the 9.5 GHz. Both E-plane and H-plane patterns agree reasonably well with the theory. The relatively wider E-plane pattern is caused possibly by the reflections of the ground plane. Patterns of the LO horn are shown in Figure 15. The H-plane pattern whose 3-dB beam width is about 50°, is smooth. The E-plane pattern, on the other hand, is very wide. This is not surprising, because the smaller opening horn does have broader beam patterns, as the theory predicted, plus the effect of the ground-plane reflections.

In conclusion, to reduce the losses in the subharmonically pumped back-to-back, horn-antenna-mixer array, compromises have to be made between the RF-impedance mismatch, the LO-impedance mismatch and the RF-LO coupling losses. In certain applications, if some LO loss is tolerable, then lower RF loss can be achieved (which means lower conversion loss) by sacrificing certain LO impedance-mismatch losses and LO-RF coupling losses. The antenna-mixer array designs presented here and in Chapter 5 not only can be used in millimeter-wave frequencies, but also may be used in submillimeter-wave frequencies, and even up to terahertz [5]. In those cases, the mixer elements could be either Schottky diodes [6] or superconducting SIS mixers [7,8].

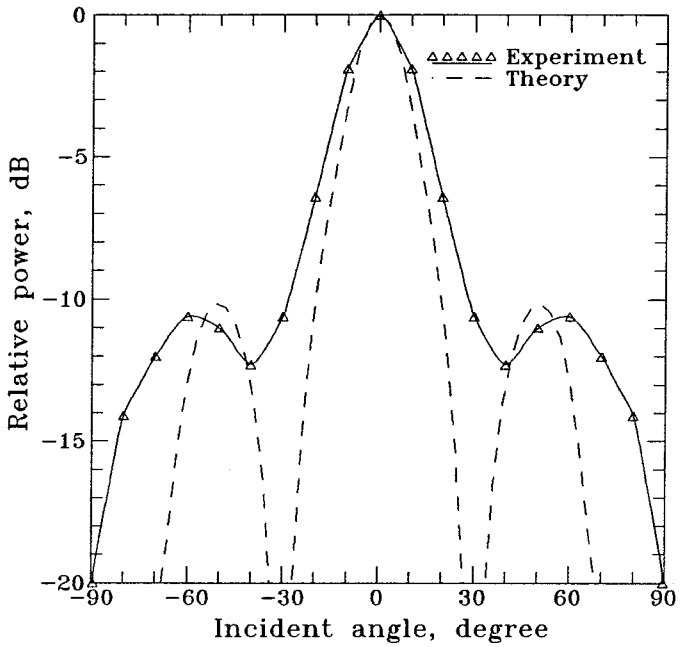

(a)

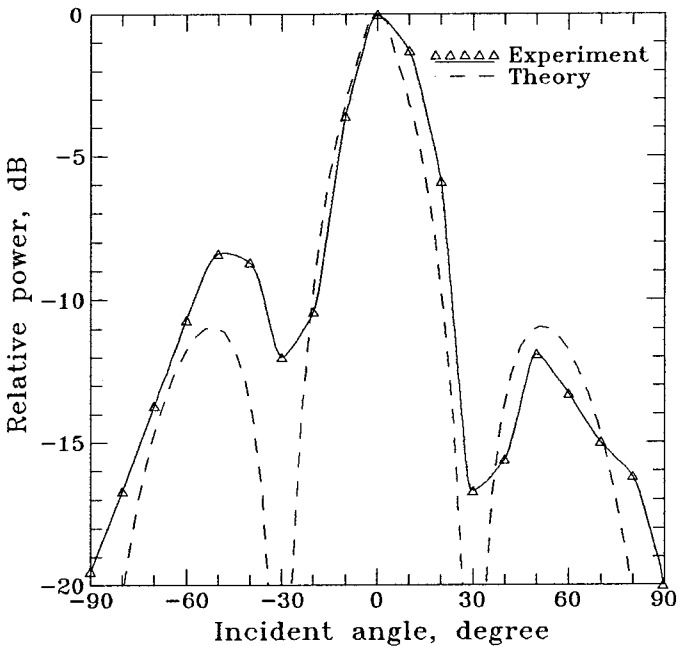

(b)

Figure 6.14 The RF horn patterns at 9.5 GHz of the split-LO-probe design; the E-plane pattern (a) and the H-plane pattern (b).

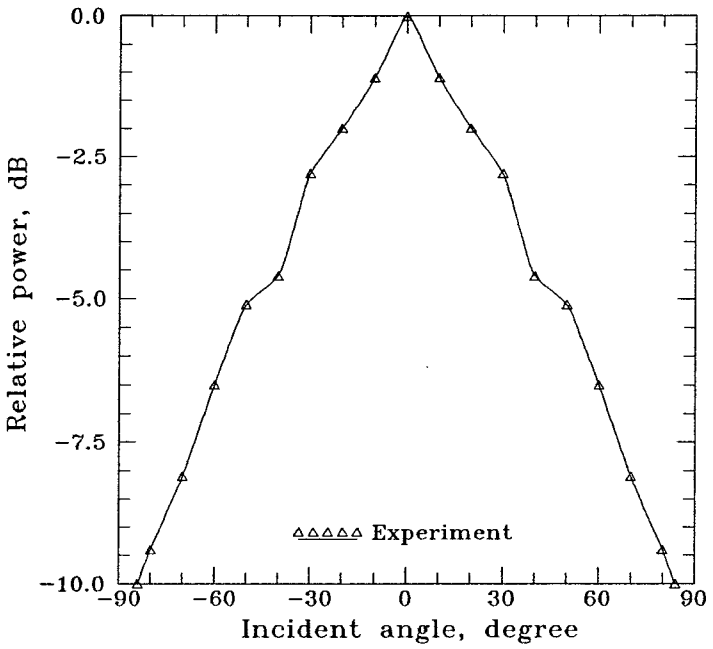

(a)

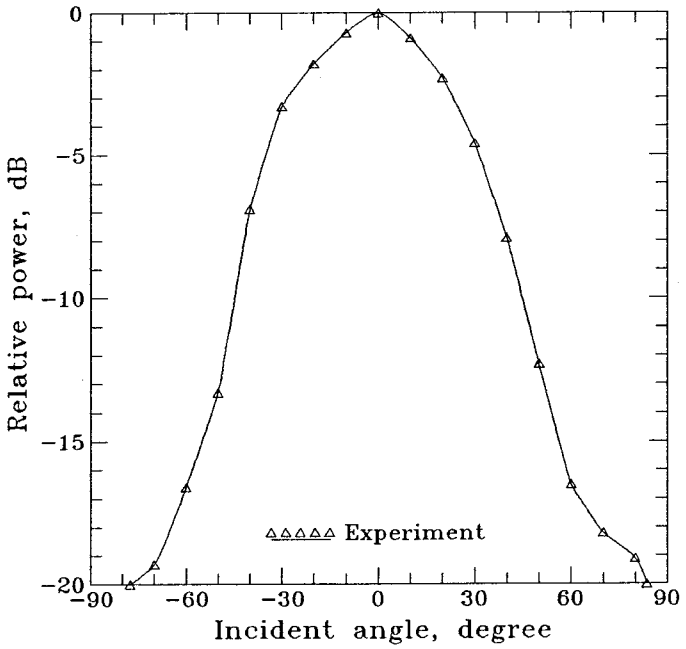

(b)

Figure 6.15 The LO horn patterns measured at 4.5 GHz; the E-plane pattern (a) and the H-plane pattern (b).

References

[1] R.C. Compton, S.W. Wedge, D.B. Rutledge, "*Puff*: Computer Aided Design for Microwave Integrated Circuits," Caltech Press, January, 1990.

[2] R. E. Collin, *Antennas and Radiowave Propagation,* McGraw-Hill Book Company, New York, 1985.

[3] G. Rebeiz, D. Kasilingam, Y. Guo, P. Stimson, D. Rutledge, "Monolithic Millimeter-Wave Two-Dimensional Horn Imaging Arrays," *IEEE Transactions on Antennas and Propagation*, Vol. 38, pp. 1473–1482, September, 1990.

[4] G.V. Eleftheriades, L.P. Katehi, G.M. Rebeiz, " High-Gain Step-Profiled Integrated Horn Antennas," submitted to *International IEEE/AP-S Symposium*, June 24–28, 1991.

[5] W.Y. Ali-Ahmad, G.M. Rebeiz, H. Dave, G. Chin, "802 GHz Integrated Horn Antennas Imaging Array," *International Journal of Infrared and Millimeter Waves*, Vol. 12, No. 5, 1991.

[6] T.W. Crowe, W.C.B. Peatman, "GaAs Schottky Diodes for Mixing applications Beyond 1 THz," *Second International Symposium on Space Terahertz Technology*, JPL, Pasadena, CA, February 26–28, 1991.

[7] M.J. Wengler, N. Dubash, G Pance, R.E. Miller, "High Gain and Noise in SIS Mixers at the Submillimeter Wavelengths," *Second International Symposium on Space Terahertz Technology*, JPL, Pasadena, CA, February 26–28, 1991.

[8] E.N. Grossman, D.G. McDonald, J.E. Sauvageau, "Terahertz Detectors Based on Superconducting Kinetic Inductance," *Second International Symposium on Space Terahertz Technology*, JPL, Pasadena, CA, February 26–28, 1991.

Chapter 7

Future Work in Integrated-Circuit Imaging Arrays

In this thesis, efficiencies of the millimeter-wave, integrated-circuit, horn antenna imaging array made on silicon have been studied and optimized, which makes the array very competitive with machined-horn antennas. Meanwhile, fabrication procedures of the horn array have been improved and are more mature. Designs and modelling of the novel, integrated-circuit, back-to-back, horn-antenna-mixer array have been presented. The antenna-mixer array combines the function of antennas and mixer circuits monolithically into a single array. Signals of RF and the local oscillator are coupled to the antenna-mixer array from both sides of the array by using quasi-optical techniques. These types of devices potentially can be mass-produced by standard, integrated-circuit technology. These designs can be used in millimeter-wave frequencies, as well as up to terahertz frequencies [1,2]. They will find useful applications in the area of imaging systems, remote sensing, and plasma diagnostics in addition to more traditional ones in radar and communications. The progress of the back-to-back horn-antenna-mixer array developments and the antenna efficiency improvements have opened opportunities for quite a few new and interesting research projects.

7.1 Coaxial Transmission Lines in Silicon

In the back-to-back antenna-mixer array (Chapter 6), the coplanar-strip transmission line in the LO horn has been shorted on both ends in simulating the transmission line being sandwiched by two conducting silicon wafers, which provide the RF and the LO isolation from the IF. Such a design is valid for IF in the range of megahertz or lower frequencies. In the millimeterwaves or submillimeterwaves, however, the IF frequency in a mixer is usually in the order of gigahertz or higher, which requires a suitable IF transmission line working at these frequencies. One way to do this as proposed here is to build a symmetrical, coaxial line in the high-conducting silicon (Figure 7.1). A very thin membrane

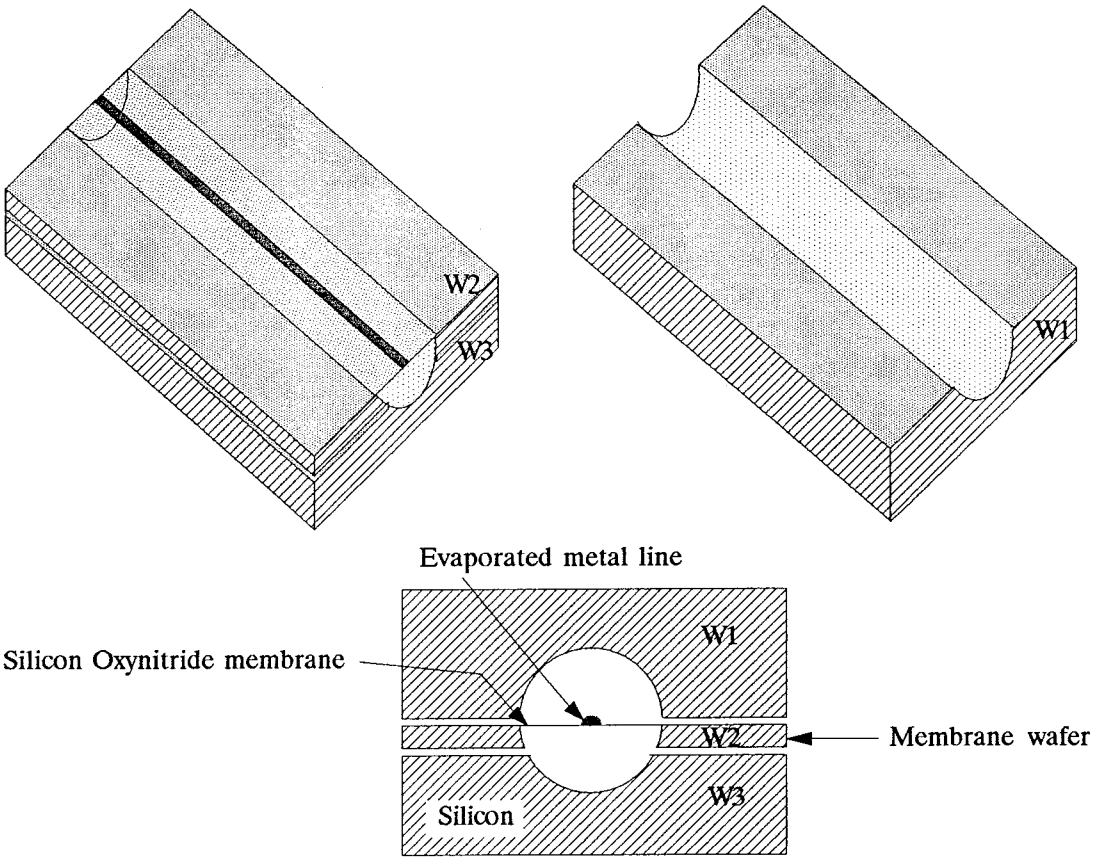

Figure 7.1 Coaxial transmission lines designed in silicon.

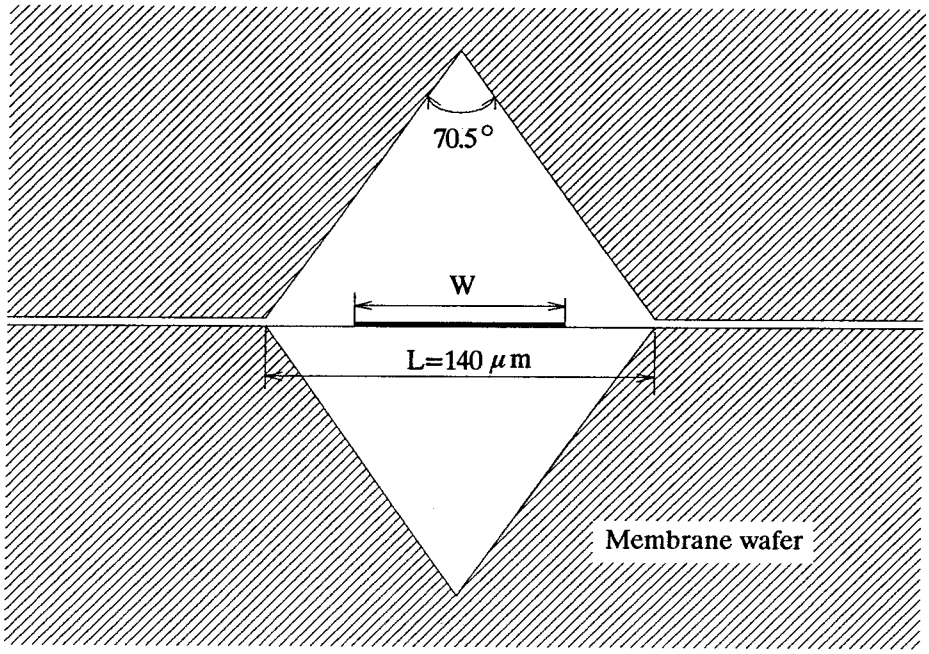

Figure 7.2 Diamond-shaped coaxial-transmission lines in silicon.

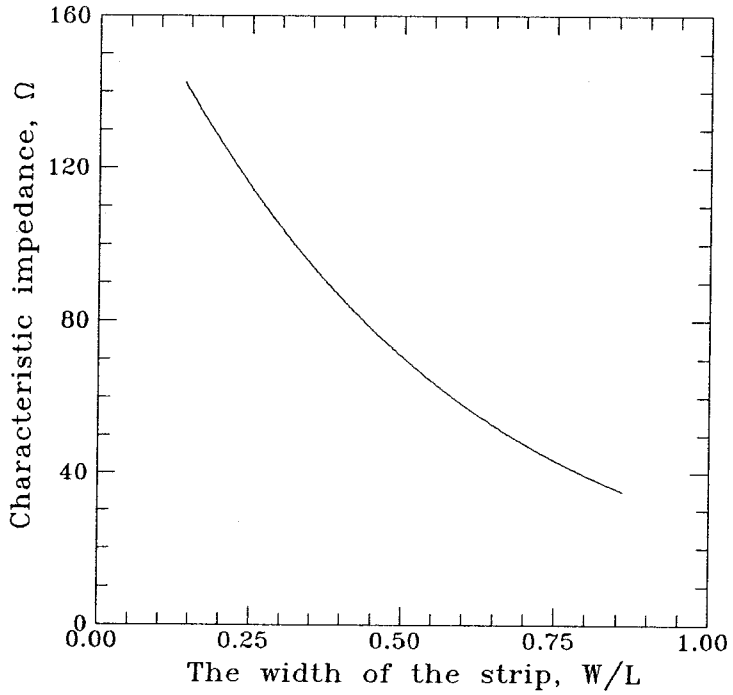

Figure 7.3 Calculated impedances of the diamond-shaped, coaxial-transmission lines versus the strip width.

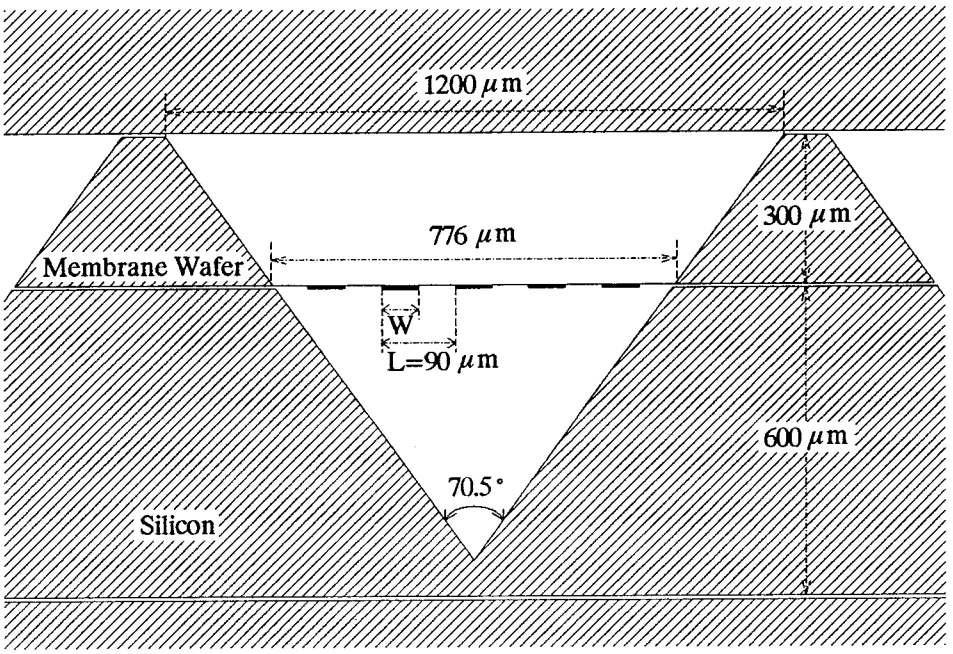

Figure 7.4 Multiple-strip transmission lines designed in silicon.

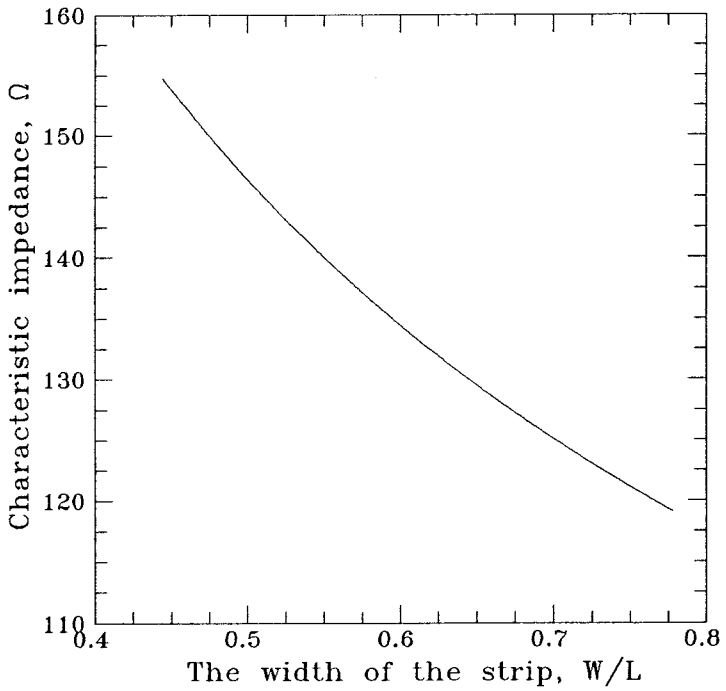

Figure 7.5 Calculated impedances of the multiple-strip transmission lines.

wafer sandwiched by two other wafers with etched grooves forms a coaxial line. The surrounding walls of the coaxial line will be coated with gold to make them a good conductor. Practically, the coaxial transmission line will look more like the one in Figure 7.2, in which the coaxial line is diamond-shaped and etched by the anisotropic etchant [3]. By changing the width of the evaporated metal line, a range of transmission-line impedances could be achieved. The impedances of the diamond-shaped transmission line have been calculated by using a finite element analysis program [4]. The results are shown in Figure 7.3, which cover the impedance range from 30 Ω to 150 Ω. This range is considered to be very suitable for the IF-impedance matching. Alternatively, a multiple-strip transmission line can be made by coating many strips on a much wider membrane in a single groove as shown in Figure 7.4, in which every other strip is grounded. The impedances, calculated by using the same program, are given in Figure 7.5. The achievable impedances are from 120 Ω to 160 Ω. These transmission-line designs could be very useful in millimeter-wave and submillimeter-wave applications when machined wave-guides are too difficult or too expensive to build.

7.2 Integrating Active Devices in the Array

In any mixers, the IF signal needs to be amplified and processed. Integrating an IF amplifier into the horn-antenna-mixer array could lead to a very attractive research project. It has demonstrated that beam-lead mixer diodes have been successfully mounted on the membrane and have passed standard industrial environmental tests (Chapter 4). Hence, as a start, an MMIC amplifier chip of the size smaller than $1 \times 1\,\mathrm{mm}^2$ can be mounted on the membrane wafer. However, as frequency goes higher into submillimeterwaves or even up to terahertz frequencies, integrating hybrid devices into the array become inadequate. In that case, the state-of-the-art mixer Schottky diodes [2] and millimeter-wave, low-noise amplifiers [5] must be monolithically integrated into the horn-antenna-

mixer array. This can be done by replacing the silicon membrane wafer by a gallium arsenide or an indium phosphide wafer, which could be etched using either reactive-ion etching [6] or a chemical-etching process [7] to produce horns with smooth walls. This can also be done by growing an epitaxial layer of gallium arsenide on the silicon membrane wafer [8]. On the membrane wafer, the Schottky mixer-diodes and the amplifiers could be made first and then protected before the horn-etching process. In addition to using advanced Schottky mixer diodes in the antenna-mixer array, a superconducting SIS junction device could also be integrated in the array as a mixing element to make a more sensitive, low-noise mixer-array. The SIS device could be deposited lithographically on the membrane suspended inside the horns. Membranes of size of $1.7 \times 1.7\,\mathrm{mm}^2$ have gone through thermal cycling from room temperature to a temperature as low as 77°K and no deterioration in the membranes has been found.

In some other applications, communications in space programs, for example, a horn antenna array integrated with amplifiers would be expected to work at frequencies of 60 GHz or lower where transmissions will not be absorbed by the oxygen in the atmosphere [9]. This requires the membrane size to be $2.5 \times 2.5\,\mathrm{mm}^2$ or larger. In our laboratory, membranes with low residual stress of a size as large as $13 \times 13\ \mathrm{mm}^2$ have been made, providing evidence that the horn antenna array can also be scaled down to lower frequencies. Practically, the horn antenna array can be designed and fabricated in frequencies down to 30 GHz with or without amplifiers or mixer circuits.

Considering the state of the art in low-noise, HEMT amplifiers working up to 100 GHz and the GaAs Schottky mixer diodes operating up to 1 THz, it should be possible to combine the ideas outlined above and to design a high-efficiency, back-to-back, horn-antenna-mixer array together with mixer diodes and IF amplifiers monolithically integrated in it, which can operate at a frequency of several hundred gigahertz.

References

[1] W.Y. Ali-Ahmad, G.M. Rebeiz, H. Dave, G. Chin, "802 GHz Integrated Horn Antennas Imaging Array," *International Journal of Infrared and Millimeter Waves*, Vol. 12, No. 5, 1991.

[2] T.W. Crowe, W.C.B. Peatman, "GaAs Schottky Diodes for Mixing applications Beyond 1 THz," *Second International Symposium on Space Terahertz Technology*, JPL, Pasadena, CA, February 26–28, 1991.

[3] A. Bohg, "Ethylene Diamine-Pyrocatechol-Water Mixture Shows Etching Anomaly in Boron-Doped Silicon," *J. Electrochem. Soc.*, vol. 118, pp. 401, 1971.

[4] The Finite Element Analysis program is called Maggie; courtesy of Professor Charles H. Wilts.

[5] Reza Majidi-Ahy C.K. Nishimoto et al., "5–100 GHz InP Coplanar Waveguide MMIC Distributed Amplifier," *IEEE Transactions on Microwave Theory and Techniques,* Vol. 38, pp. 1986–1993, December 1990.

[6] G. Smolinsky, R. P. Chang and T. M. Mayer, "Plasma Etching of III-V Compound Semiconductor Materials and Their Oxides," *J. Vac. Sci. technol.,* vol. 18, pp. 12–16, Jan.–Feb. 1981.

[7] D. W. Shaw, "Localized GaAs Etching with Acidic Hydrogen Peroxide Solutions," *J. Electrochem. Soc.: Solid-State Science and Technology,* vol. 128, pp. 874–880, April 1981.

[8] M.R. Wilson, Y.D. Shen, B.M. Welch, "GaAs-on-Si: A GaAs IC Manufacture's Perspective," *Proceedings of the GaAs IC Symposium* Nashille, Tennessee, pp. 243–246, November 6–9, 1988.

[9] E.S. Rosenblum, "Atmospheric Absorption of 10–400 KMCPS Radiation:

Summary and Bibliography to 1961," *Microwave J.*, vol. 4, pp. 91–96, March 1961.